University of West Bohemia in Pilsen
Faculty of Applied Sciences

THERMO-PHYSICAL PROCESSES AND ULTRASHORT PULSE LASER SCANNING METHODS IN SURFACE TEXTURING

Denys Moskal

Ph.D. Dissertation

to obtain the academic title Doctor

in "Physics of plasma and thin films"

Supervisor: Doc. Ing. Milan Honner, Ph.D.

Department of Physics

Pilsen 2019

Západočeská univerzita v Plzni
Fakulta aplikovaných věd

TERMOFYZIKÁLNÍ PROCESY A METODY LASEROVÉHO SKENOVÁNÍ S ULTRAKRÁTKÝMI PULZY V POVRCHOVÉM STRUKTUROVÁNÍ

Denys Moskal

disertační práce
k získání akademického titulu doktor
v oboru Fyzika plazmatu a tenkých vrstev

Školitel: doc. Ing. Milan Honner, Ph.D.

Katedra: Katedra fyziky

Plzeň 2019

This dissertation has been submitted to the Faculty of Applied Sciences, University of West Bohemia in collaboration with New Technologies - Research Centre. The Ph.D. dissertation was developed within the CENTEM project, reg. no. CZ.1.05/2.1.00/03.0088, co-founded by the ERDF as part of the Ministry of Education, Youth and Sports OP RDI programme and, in the follow-up sustainability stage, supported through CENTEM PLUS (LO1402) by financial means from the Ministry of Education, Youth and Sports under the ”National Sustainability Programme I” and project SGS-2019-008.

I hereby declare that this doctoral thesis, my original investigation and achievement, is submitted for the doctoral degree at the University of West Bohemia and has not been submitted before for any academic degree.

In Pilsen __.__.2019 ……..

Denys Moskal

Acknowledgements

Here I want to thank my supervisor Doc. Ing. Milan Honner, Ph.D. for his insight in leading of my Ph.D. work and his help with strategic decision-making. At the same time, I need to say thanks to the Head of the Department of Physics, Prof. RNDr. Jaroslav Vlček, for giving me the opportunity to work in the New Technologies - Research Centre and all support. A special thanks for my colleague Doc. Jiří Martan, Ph.D. for help in experimental work and many good discussions of results. And, of course, thanks to my other colleagues for collaboration on the different parts of the work: Ing. Martin Kučera, Ph.D., Ing. Vladislav Lang, Ph.D., Bc. Lucie Prokešová, Bc. Ladislav Smeták and others.

In Pilsen 2019

Abstract

Laser surface texturing is one of the methods used for controllable surface structuring and acquisition of specific surface physical properties. This Ph.D. dissertation is focused on the characterization of the thermo-physical processes in ultrashort pulse laser surface texturing (LST) and development of the laser scanning methods for high-speed processing with high precision and low heat accumulation.

In the first part of the dissertation, a review of LST for several applications is presented: in biology, material engineering, medicine, optics, semiconductor electronics and other areas. The different physical mechanisms of ultrashort laser pulse interaction with an irradiated surface are considered. The physical limitations, such as heat accumulation and shielding effects, are discussed. The current state of the art of modern LST methods is presented.

Based on the literature review, the aims of the work and main tasks are defined: measurement and analysis of the thermal IR radiation signals detected during laser surface processing and comparison with theoretical predictions; the proposal and implementation of new scanning strategies for high-speed LST; evaluation of the precision, processing rate and heat accumulation in the LST methods; and practical application of the developed LST methods.

In the next part, the research methods used in the study are presented. The heat accumulation and ablated plasma glow duration measurements with fast IR detectors and data processing methods are described. The new shifted LST method is developed and compared with classic LST methods. The methods for evaluation of the precision and processing rate are presented. The semi-planar thermo-physical model for analytical prediction of surface temperature changes is described.

The next part contains the achieved results and discussion. The laser surface processing regimes obtained during experiments were characterized by three levels of heat accumulation: low heat accumulation, critical and overheated. A decrease of ablated plasma glow duration at higher scanning speeds was detected. The possible reasons for this dependence are proposed. It was discovered that the shifted method reaches a more than ten times higher processing rate with negligible microobject geometry deviation. Similar results were achieved in experiments with depth profile testing on the laser-textured microobject array. The highest processing rate was achieved with the shifted LST method in burst regime. The analysis of the temperature regimes shows that the heat accumulation is similar for both the classic and shifted LST strategies and the overheated regime was not reached. For the shifted LST method, the heat accumulation is even lower than the critical boundary. The temperature distribution in material obtained by the analytical model shows a reasonable agreement with experimental results of the IR radiation measurements. The practical application of the shifted LST method is presented in comparison with classic methods.

The conclusion and proposals for further research are presented at the end of the dissertation. The benefits of the IR radiation signal analysis and shifted LST method are underlined.

Anotace

Laserové texturování povrchu je jednou z metod pro kontrolované strukturování a získávání specifických fyzikálních vlastností povrchu. Disertační práce je zaměřena na charakterizaci termofyzikálních procesů laserového texturovaní povrchu (LST) s ultrakrátkými pulzy a vývoj laserových skenovacích metod pro rychlé zpracování povrchu s vysokou přesností a nízkou akumulací tepla.

V první části práce je uveden přehled laserového texturovaní povrchu pro několik aplikací: v biologii, materiálovém inženýrství, medicíně, optice, polovodičové elektronice ad. Jsou zvažovány různé fyzikální mechanismy interakce ultrakrátkých laserových pulzů s ozářeným povrchem a představena fyzikální omezení, jako je akumulace tepla a účinky stínění plazmatem. Rovněž je prezentován aktuální stav moderních metod LST.

Na základě literární rešerše jsou definovány cíle práce a hlavní úkoly: měření a analýza tepelného infračerveného záření detekovaného při laserovém zpracování povrchu a porovnání s teoretickými předpověďmi; návrh a implementace nových skenovacích strategií pro vysokorychlostní LST; vyhodnocení přesnosti, rychlosti zpracování a akumulace tepla v různých LST metodách; praktická aplikace vyvinutých metod LST.

V další části jsou uvedeny výzkumné metody použité v práci. Jsou popsána měření akumulace tepla a doby ablačního záření pomocí rychlých IR detektorů a metody zpracování dat. Nová posuvná metoda LST je vyvinuta a porovnána s klasickými metodami LST. Jsou uvedeny metody pro vyhodnocení přesnosti a rychlosti zpracování. Je popsán polorovinný termofyzikální model pro analytickou předpověď změn povrchové teploty.

Další část obsahuje dosažené výsledky a diskusi. Režimy laserového zpracování povrchu získané během experimentů byly označeny třemi úrovněmi akumulace tepla: nízká akumulace tepla, kritická a přehřátá. Bylo zaznamenáno snížení doby ablačního záření při vyšších skenovacích rychlostech. Jsou navrženy možné důvody takové závislosti. Bylo zjištěno, že posuvná metoda dosahuje více než desetkrát vyšší rychlosti zpracování se zanedbatelnou odchylkou geometrie vytvořených mikroobjektů. Posuvná metoda dosáhla nejmenší odchylky geometrie v experimentech s laserovým vytvářením hloubkového profilu povrchových mikroobjektů. Nejvyšší rychlosti zpracování bylo dosaženo s posuvnou metodou LST v režimu seskupení laserových pulzů (*burst*). Analýza teplotních režimů ukázala, že akumulace tepla je podobná pro klasickou i posuvnou strategii LST a přehřátý režim nebyl dosažen. U posuvné metody LST je akumulace tepla dokonce nižší než kritická hranice. Rozložení teploty v materiálu získané analytickým modelem ukazuje přiměřenou shodu s experimentálními výsledky měření IR záření. Ve srovnání s klasickými metodami byla prezentována i praktická aplikace posuvné metody LST.

Závěr a návrhy na další výzkum jsou uvedeny na konci práce. Jsou zdůrazněny výhody analýzy infračerveného záření a posuvné metody LST.

Designations

α	energy exchange rate between electron gas and lattice
α_{th}	thermal diffusivity
A	absorption of the surface
c	speed of light
c_e	electron specific heat
c_l	lattice specific heat
c_p	specific heat capacity
Δ_g	goal diameter of laser-textured microobjects
Δ_g^P	goal depth profile
$\Delta_{major,i}$	length of major axis of laser-textured microobject
$\Delta_{minor,i}$	length of minor axis of laser-textured microobject
$\Delta_{max,i}$	i_{th} object diameter deviation from major axis length
$\Delta_{min,i}$	i_{th} object diameter deviation from minor axis length
Δ_k^P	depth deviation of k_{th} profile from a goal profile form
f_c	fraction of water-solid contacted area divided by the projected area
f_{trg}	external trigger frequency
F	laser fluence (or energy density)
F_0	fluence in the center of the laser beam
F_{th}	threshold laser fluence
F_{heat}	residual heat after laser surface ablation
F_a	absorbed laser fluence
f_{pulse}	laser pulse frequency
h	Planck constant
h_i	vertical distance between measured i_{th} profile and goal profile lines
ΔH	hatch distance
i, p	summation indexes
ΔIL	interlace distance
$I(\lambda)$	IR radiation emitted by the laser heated surface
$I(t)$	time distribution of the laser intensity in a laser pulse
k_e	thermal conductivity of electron subsystem
k_p	thermal conductivity of phonon subsystem
k	thermal conductivity of material
k_b	Boltzmann constant
l_{trg}	distance between laser spots formed with external trigger
l_a	absorption depth
l_{th}	thermal penetration depth
l	step value along horizontal direction on profilogram
λ_{ball}	ballistic electron penetration depth
λ_{opt}	optimal wavelength
λ	light wave length
λ_{th}	heat conductivity

M number of rows in an array of microobjects
M_o number of microobjects in one row of array
N_b number of recorded values in the sequence without laser influence
N_r number of signals analyzed in the closest to the next laser pulse segment
η fraction coefficient
N number of objects (laser spots, microobjects or laser pulses)
N_f full number of laser pulses in a sequence
N_{sh} amount of data for shifted method
N_{cl} amount of data for classic method
n_g parameter of the laser spot geometry
n number of a laser pulse applied over a fixed point
P_o laser pulse overlap
P laser average power
Q_p laser pulse full energy
Q laser pulse energy absorbed in material, before ablation
Q_r residual energy absorbed by material after material ablation
Q_l line energy
Q_{th} laser energy distribution in irradiated surface
r_{wa} factor representing increase in the wetted surface area
R full number of analyzed segments in data sequence
r distance from laser spot center
r_s distance from heat source
r_d laser spots distance
ρ mass density
δ penetration depth
S incubation coefficient
ΔS distance between pulses in the laser beam scan direction
s standard deviation
ξ_i relative diameter deviation of i_{th} object from goal diameter
$\overline{\xi}$ mean value of the relative diameter deviation at one speed
ξ relative depth profile deviation
σ tensile strength
t_p laser pulse duration
t_{lp} period between laser pulses
T_e electron temperature
T_l lattice temperature
T_v evaporation temperature
T_s surface temperature
T_m melting temperature
T_{th} critical temperature
t time
t_n time from application of n_{th} laser pulse
t_i time moment, which corresponds to the signal value index i

t_w	plasma glow duration time
t_d	time moment when the integral signal lower from boundary limitation
t_u	time moment when the plasma glow signal higher from boundary limitation
ΔT	residual temperature after laser pulse
ΔT_{Sum}	residual temperature after sequence of laser pulses
θ_f	contact angle for flat surface
θ_m	contact angle measured on real rough surface
U_b	background signal level
$U_{b,i}$	background signal detected at time moment t_i
U_r	mean value of residual heat signal
$U_{r,i}$	value of i_{th} residual heat signal recorded in time moment t_i
U_h	heat accumulation signal
U_{mb}	difference between absolute peak maximum and background level
U_{mr}	difference between absolute maximum and resistive heat signal
v_{sc}	laser beam scanning speed
v_{pr}	processing rate
ΔV	ablated volume
ω	laser spot radius
γ_{sg}	solid-gas surface tension
γ_{sl}	solid-liquid surface tension
γ_{lg}	liquid-gas surface tension
z	depth coordinate
z_{abl}	ablation depth

Abbreviations

AFM	Atomic Force Microscopy
AOD	Acousto-Optic Deflector
bcc	body-centered cubic
DLIP	Direct Laser Interference Patterning
EDX	Energy-Dispersive X-ray Spectroscopy
EOD	Electro-Optic Deflector
IR	Infra-Red
LIPSS	Laser-Induced Periodic Surface Structures
LP	Low Pass
LSP	Laser Shock Peening
LST	Laser Surface Texturing
NDT	Nondestructive Defect Testing
NIR	Near Infrared Radiation
SLM	Selective Laser Melting
SLMs	Spatial Light Modulators
SD	Standard Deviation
sLST	shifted Laser Surface Texturing
TTM	Two-Temperature Model
XTT	Tetrazolium Salt

1. Introduction

Laser Surface Texturing (LST) offers the most promising concept in terms of industrial improvement of surface functionalization. The small size of a laser spot with significant energy density becomes an excellent tool for the formation micro- or nanoobjects on material surfaces [1]–[4]. Laser-controlled material ablation gives the possibility to form surface microobjects with high precision and specific geometry: dimples, columns, riblets, polygonal or hierarchical structures [5]–[8]. The consequent location of microobjects in an array on a material surface provides wide area LST. Such laser-textured arrays of microobjects are able to change the physical, chemical or biomedical properties of processed surfaces. Currently, LST is one of the most flexible methods for forming new functional surfaces: hydrophobic, antibacterial, adhesive, self-cleaning, light absorbing, wear resistance or low frictional [9], [10]. One of the popular ways of forming functional surfaces is laser texturing with mimicry of an existing natural surface, like lotus leaves, insect's wings or eyes, gecko's legs or shark skin [11]–[13].

For many cases, the desired functional properties of laser-textured surfaces are predefined by the correct geometry of laser-formed microobjects. High precision of material processing is often limited by the dynamic parameters of a laser beam deflection system, such as inertia of the mirrors and mirror positioning control. For the most popular galvanometer scan systems, this is the main limitation for achieving high precision at higher scanning speeds. Moreover, the quality of the resulting surface is affected by physical effects, which are initiated under laser-pulsed surface machining: heat accumulation, surface shielding by ablated materials or incubation effects [14]–[21]. Such effects are limiting for application of high-frequency lasers with high scanning speed and high precision of the laser surface micromachining.

This work is devoted to the characterization of thermo-physical processes in scanning surface processing with ultrashort laser pulses and definition of the principal limits of existing LST strategies of surface texturing with a galvanometer scanner. The next goal is to propose an improved scanning strategy for overcoming the physical and principal limitations of existing methods of LST and real application of the developed LST methods on different functional surfaces.

2. Current state of the art in the laser surface texturing (LST) of functional surfaces

2.1. The main principles of the LST with material ablation processes

In this work, the concept of LST described as forming a wide array of microobjects by laser beam scanning surface modification with a series of laser pulses (Fig. 2.1, *a*). The geometry of the output surface structure depends on laser beam scanning strategy and physical processes under every laser pulse irradiation. The initiated physical processes in an irradiated surface depend on the parameters of the laser pulse, such as intensity, wave length and pulse duration [22], [23]. There are several intermediate physical processes from the laser pulse surface absorption till the post-ablation surface cooling: reflection, scattering, plasma plume and ablating material explosion, shock and pressure waves spreading, energy dissemination by IR radiation and convection (Fig. 2.1, *b*). The correct choice of laser pulse parameters and the scanning method of LST is the key solution for production of functional surfaces with uncial physical properties.

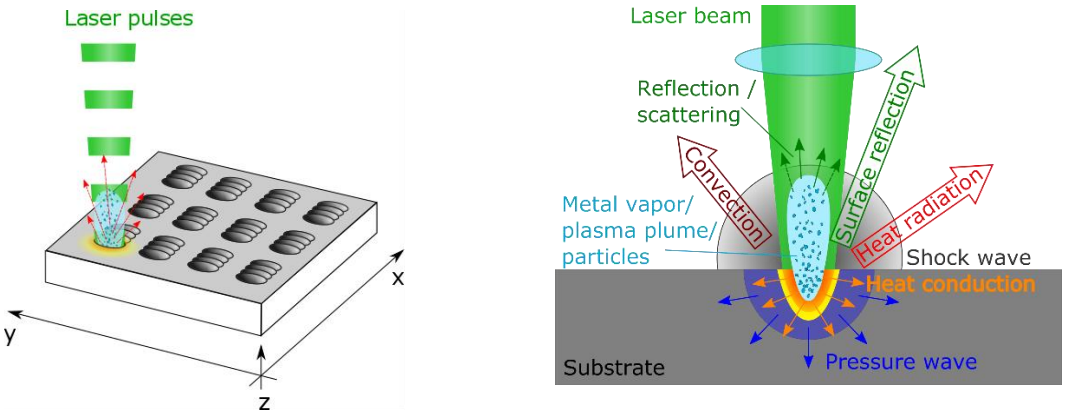

a *b*

Fig. 2.1. The basic principles of LST: *a* – laser-pulsed surface texturing with formation of the microobjects array; *b* – physical processes occurring under laser pulse interaction with a solid state substrate.

In this chapter, the best known applications of LST for laser surface functionalization are described. The most attention will be paid to the current state of the art for functional surface micromachining by scanning laser systems in pulsed mode. The physical phenomenon of laser ultrashort pulse interaction with metals in connection with laser scanning techniques will be presented in the two last sections of this chapter.

2.1.1. Wettability of textured surfaces

One of the best known examples of laser material surface functionalization is preparing superhydrophobic structures, where the water contact angle is higher than 150° [24]–[26]. The main principle of preparing superhydrophobic structures lies in forming micro-columnar structures [27]. Physical principles of wettability decreasing for textured surfaces can be explained by the Cassie-Baxter model [28]. It can be explained by comparison of the

wettability of a flat surface with that of a textured surface. On a flat surface, contact angle θ_f is in direct dependence on surface tension [29]:

$$\gamma_{sg} = \gamma_{sl} + \gamma_{lg} cos\theta_f, \quad (2.1.)$$

where γ_{sg} – solid-gas surface tension, γ_{sl} – solid-liquid surface tension and γ_{lg} – liquid-gas surface tension.

On a textured surface, two opposite scenarios can be observed. If roughness is not high and water drops are in contact with the tops and bottoms of the textured structure, then the surface obtains hydrophilic properties [27], [30] (Fig. 2.1.1, *a*). In this case, the energy of the system decreases for a smaller measured contact angle θ_m, which can be defined from the Wenzel equation [31]:

$$cos\theta_m = r_{wa} \cdot cos\theta_f, \quad (2.2)$$

where r_{wa} – factor representing an increase in the wetted surface area. Such structures can be applied for forming self-cleaning, cell manipulation, adhesion enhancement, anti-fogging, fluid flow control, evaporative cooling and others [30], [32]–[34].

a *b*

Fig. 2.1.1. Wetting of a textured surface. *a* – wetting of a low roughness surface; *b* – hydrophobicity on a surface with high density of textured microobjects [27].

Increasing the surface roughness with a higher density of textured microobjects leads to the appearance of hydrophobic properties. In this case, the water drop does not have direct contact with the bottom surface between microobjects (Fig. 2.1.1, *b*). A decreased contact area of water drops with the solid surface leads to an increase in interfacial energy between water and gas. The contact angle of such a heterogeneous surface can be defined by the Cassie-Baxter equation:

$$cos\theta_m = f_c cos\theta_{flat} + f_c - 1, \quad (2.3)$$

where f_c – is the fraction of the water-solid contacted area divided by the projected area. This dependence of the real contact angle on the textured microobject's density gives the possibility to form superhydrophobic surfaces, when the contact angle becomes larger than 150° [25]. The main advantage of superhydrophobic surfaces was inspired by nature. When water drops absorb particles of dust from a textured surface without wetting it, is well known the Lotus effect [13], [35]–[37].

The flexibility and precision of modern laser technologies allows us to combine surface microtexturing with nanometric texture to form a hierarchical structure. This application of an

LST method is the most popular technology for formation of superhydrophobic surfaces on different materials (Fig. 2.1.2): metals [24], [38]–[42], glasses [43], [44], polymers [45], [46], ceramics [47] and so on [48]–[50].

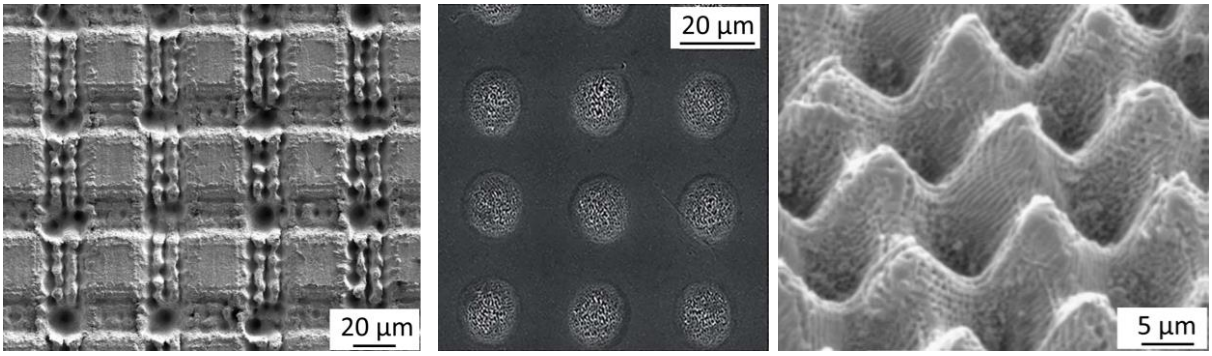

a *b* *c*

Fig. 2.1.2. Superhydrophobic laser-textured surfaces on: *a* – metal (AISI304) [41]; *b* – glass (silica glass) [43]; *c* – polymer molded in laser textured form (polypropylene) [27].

There are several methods for achieving hydrophobicity on metallic surfaces. One of the well-known way of superhydrophobic surface formation is the application of laser beam writing with a nanosecond pulses. Commonly, a laser is used together with a galvanometer scanner system for machining of arrays of square pillars or microgrooves. In the series of the papers of V. D. Ta et al. [24], [38], the nanosecond laser texturing of superhydrophobic surfaces was reported. The spot size in these experiments is $\omega = 20$ µm and pulse duration in the range of $t_p = 4 \div 200$ ns, pulse frequency 20 ÷ 100 kHz and peak power in the mJ range [24], [38], [39], [50]. Distance between microgrooves or pillars is about 10÷100 µm [24], [51]. The scanning speed for such applications is not high and commonly is smaller than 1 m/s [24], [52]. Superhydrophobic properties of nanosecond laser-scanned surfaces are explained by the formation of burrs and debris from molten material [24], [53]. It is difficult to predict the goal geometry of the surface texture with a nanosecond laser. For the direct forming of the surface microtextures, ultrafast lasers are widely used [24], [42], [54]–[59]. Laser machining with pico- and femto-second lasers gives the possibility to achieve a predefined geometry of microobjects more precisely. In this way, unusual wetting properties of functional surfaces can be formed. For example, there can be a combination of superhydrophobic and superhydrophilic properties on the same surface [60].

2.1.2. Friction and wear resistance

The presence of a lubricant between two sliding surfaces is the main way to decrease the friction forces between them. This is the main reason for application of LST for sliding bearings [61], [62]. An array of dimples on the sliding surface can work as a field of pockets for the

lubricant and is able to change hydrodynamic flows between sliding areas [63]–[66]. The correct distribution and form of laser-textured microobjects on sliding surfaces is able to significantly change the dynamic character of the sliding bearing [67]. Several factors have an influence on the optimal friction surface texturing geometry. It can be affected by sliding speed, oil pressure, temperature and viscosity [68]. An optimal laser-textured dimple size is basically determined by tribology experiments. Fig. 2.1.3 is shows an example of experimental results obtained by pin-on-disc tribology tests with a laser-textured C85 balls section (Fig. 2.1.3, *a*) [69]. In these tribological tests, it was specified that the minimal value of the friction coefficient corresponds to the diameter 40 µm of the laser-textured dimples. A friction reduction up to 80% was possible with the optimal diameter for certain sliding speeds of the bearing surface (Fig. 2.1.3, *b*) [69].

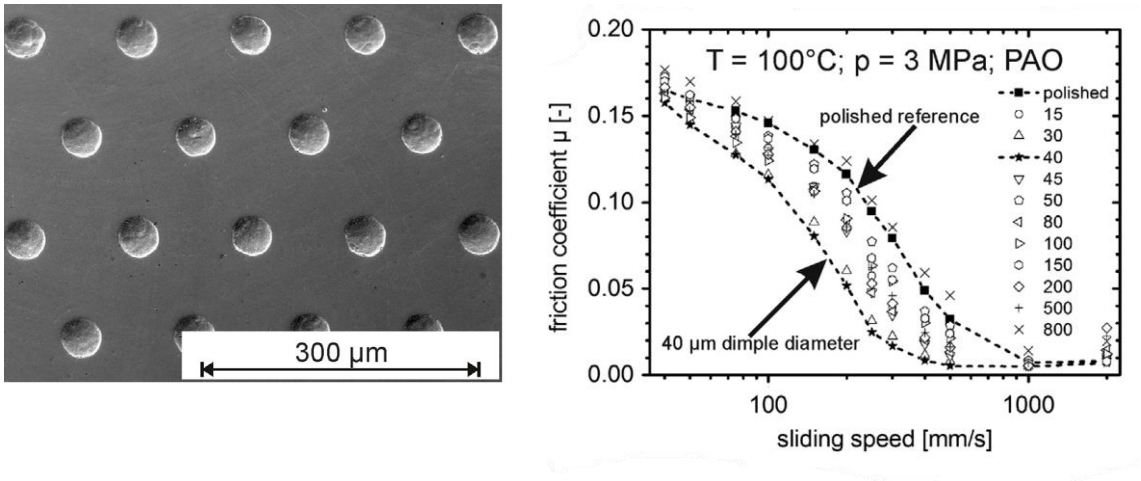

a *b*

Fig. 2.1.3. LST for tripological tests: *a* – laser-textured surface of C85 steel; *b* – friction coefficient plotted against the sliding speed of laser-textured surfaces with different diameter of dimples 15÷800 µm [69].

Exploiting the flexibility and micrometric accuracy of laser-scanning systems gives the possibility to realize complex micro-structural modifications of bearing surfaces. The form and relative location of microobjects in the laser-textured array has a great influence on the friction coefficient. A rectangular dimple-textured pad exhibited an overall lubricated friction coefficient which was approximately 20% lower than the elliptical dimple counterpart. The improved tribological performance was ascribed to the better morphology of the rectangular dimples. Partial texturing of a bearing surface with a lattice of finite-sized grooves with a certain angular misalignment to the sliding direction is able to reduce the friction too [70], [71]. Such non-uniform surface texturing allows development of a new generation of so-called “super-bearings”, with unique and enhanced tribological performances that, in addition, can be tailored according to the sliding direction (Fig. 2.1.4) [71], [72]. Another possibility for decreasing the friction coefficient is the application of a combination of different textures. In

the work of Segu et al., a multi-scale textured surface which showed a three times smaller friction coefficient in comparison with a polished surface was created [73].

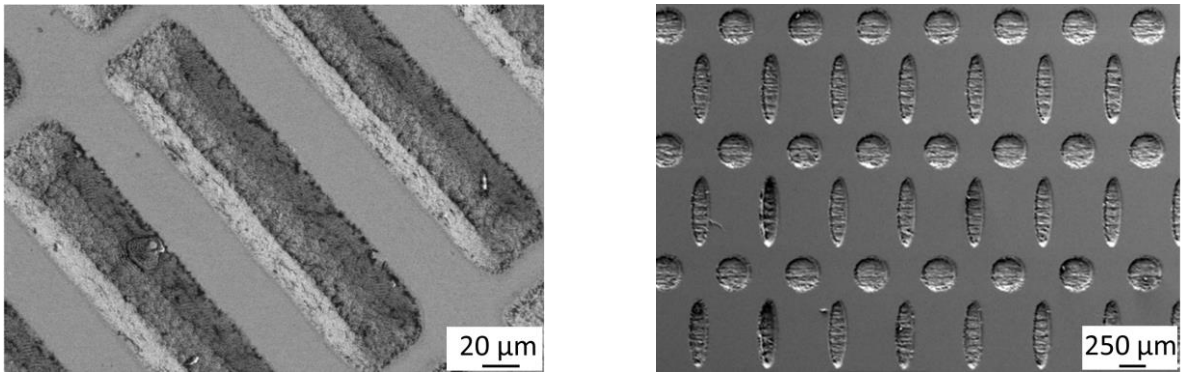

a *b*

Fig. 2.1.4. Non-uniform surface texturing of a bearing surface: *a* – laser-textured rectangular microobjects in non-uniform alignment [71], [72]; *b* – multi-scale textured surface with high density of 20% of the surface [73].

An additional feature of laser-textured surfaces is increase in wear resistance. On a flat surface, the wear particles keep rolling between sliding surfaces (Fig. 2.1.5, *a*) [74]. This leads to longitudinal erasure of contact areas and increasing friction leaks and temperature. The oxidation of the bearing surfaces under lubrication-starved conditions can be observed [75]. In contrast, the laser-textured surface is able to prevent this. Laser-machined microobjects on such surfaces work as traps for wear particles (Fig. 2.1.5, *b*) [74], [75]. This benefit of laser-textured surfaces can be obtained even in the case of dry friction [76], [77] (Fig. 2.1.5, *c*).

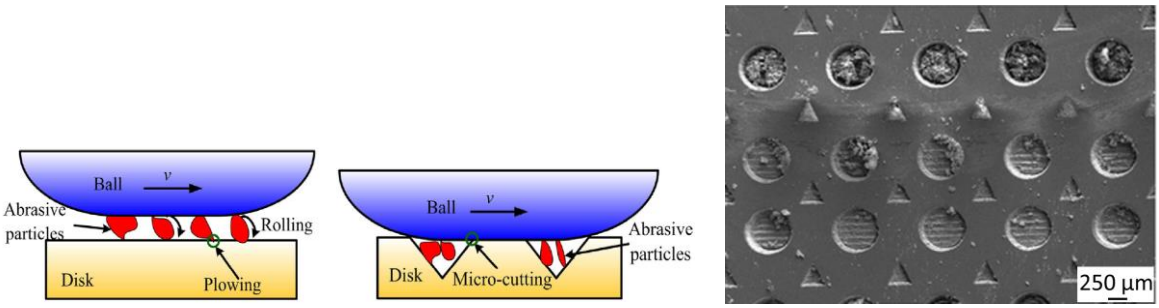

a *b* *c*

Fig. 2.1.5. Wear particles: *a* – between flat sliding surfaces [74]; *b* – between flat and laser-textured surfaces [74]; *c* – laser-textured surface in dry friction test. The wear particles are trapped inside of laser-textured microobjects; texture depth 5.5 µm, object size 500-250 µm [76].

Wear resistance of soft materials, like plastics, is achieved with laser surface texturing with hierarchical structures. In this method, a sequence of two LST techniques is applied – microtexturing with the next nano-texturing [78]. In this way, the weakest nano-texturing will

be protected against mechanical damage. On such hierarchical structures, only the upper part will be damaged, but the nano-texture remains protected in the bottom parts of the macrotexture. A similar technique can to be applied to a wide range of materials: polycarbonate [79], metals [80], [81] and glasses [82] (Fig. 2.1.6).

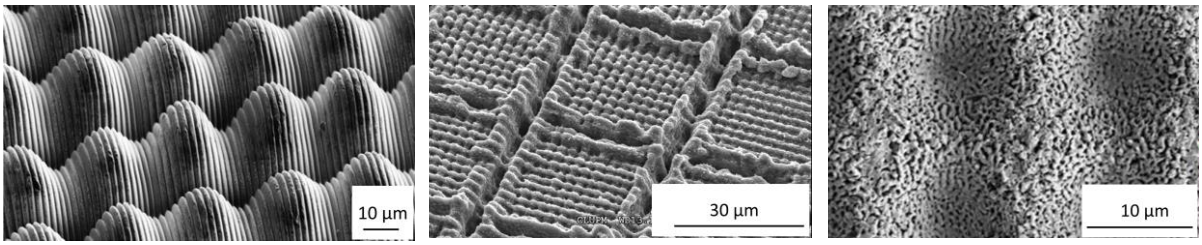

a *b* *c*

Fig. 2.1.6. Hierarchical structures on different materials: polycarbonate [79], metals [80] and glasses [82].

Improving wear resistance by using LST has great potential due to the flexibility of the laser technologies. This two-level LST gives the possibility to create persistent surface structures with unusual physical properties [83]. This clever solution can find application everywhere, when the specific surface properties should be kept at least partially: in medicine, metal production, bearings or the chemical industry.

2.1.3. Optical properties

The application of LST on photovoltaic elements is one of the common ways of improving the optical properties of laser-processed surfaces [6], [84]–[87]. Multiscale texturing of a surface can cause significant deviations in how light is reflected and scattered, leading to enhanced absorption unlike with flat smooth surface. For surface features with dimensions greater than several wavelengths of light, this enhancement can most easily be described using the principles of ray optics. A portion from a ray of light will specularly reflect from a flat surface and have no further interaction with the material. But the protruding features can reflect and scatter light back onto the surface. Light can effectively become trapped in crevices and holes with multiple reflections. Once inside these protruded structures, multiple internal reflections can guide the light into the bulk. Refraction at the surface of these structures also leads to transmission at oblique angles, effectively increasing the optical path length, enhancing absorption. The degree of enhancement depends on the particular geometry and dimension of the surface features (Fig. 2.1.7, *a*) [84], [88], [89]. After laser texturing of polycrystalline silicon solar cells, the reflection from their surface was reduced by up to 14 ÷ 18% (Fig. 2.1.7, *b*) [85], [87].

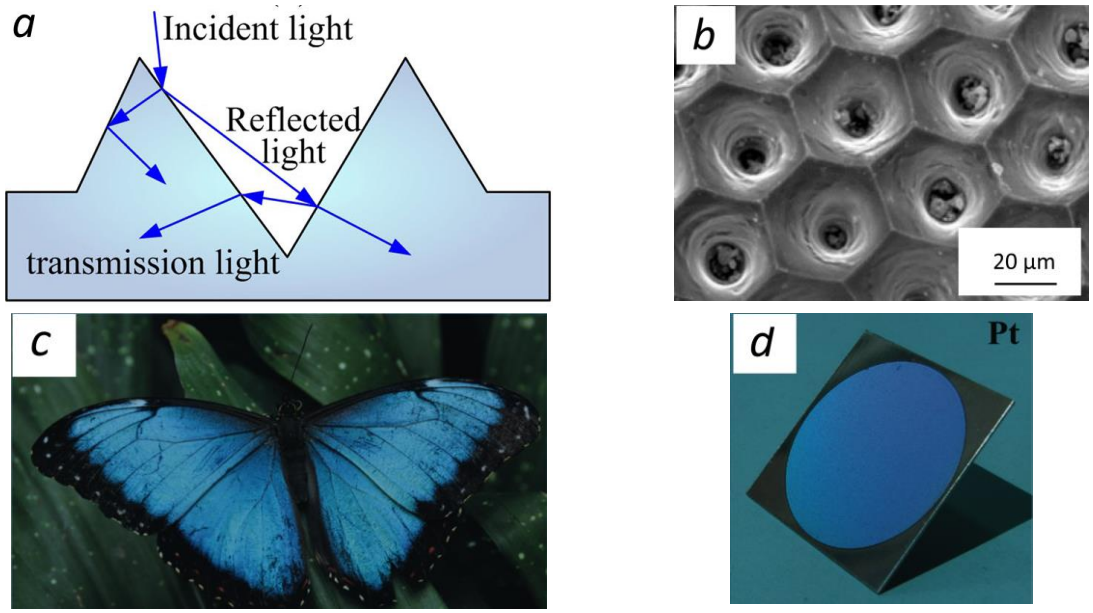

Fig. 2.1.7. LST of antireflective surfaces: *a* – principle of light waves propagating on a laser-textured surface [88]; *b* – laser-textured surface of a photovoltaic multicrystalline silicon element [87]; *c* – the butterfly Morpho with iridescent blue wings due to sophisticated periodic microstructures of the wings [9]; *d* – iridescent color of a platinum sample with femtosecond laser-induced periodic structures [9].

In the case of LST of metals, the optical properties of a surface can be dramatically changed. Ultra-high light trapping structures are in the literature called “black” metal [9], [88], [90]. Such LST structures on TC4 titanium are able to increase surface absorption 10 times. Another application of metal LST is “colorization” of a surface. An example of structural coloration in nature is the wing of the Morpho butterfly (Fig. 2.1.7, *c, d*). Its metallic, iridescent blue color is not caused by pigments, but originates from light interference and diffraction on complicated periodic microstructures [9], [91], [92].

Similar principles of changing optical parameters with LST can be applied for other optical devices – detectors, emitters, light guides, Bragg gratings and photonic crystals [6], [9], [93]–[95]. For all these applications, the precision of material processing should be at wavelength scale. Specific materials of optical devices often have a temperature-sensitive structure. For example, diamond-based detectors and grates should be processed with minimal heat degradation to prevent laser transference into the graphite phase [96]–[99].

2.1.4. Biomedical laser-textured surfaces

Laser surface functionalization has also found its application in biomedicine [100]. Texturing of bone implants is one of the most known techniques for increasing biocompatibility of allenthesis surfaces [101]–[104]. Such an application of LST improves mechanical interlocking of implants in a bone [105], [106]. It was shown, that selective laser-modified titanium implants have a 250% increased removal torque [107]. Study of cell attachment of laser-textured surfaces has shown that cell density is very sensitive to the geometry of the surface pattern [101], [108]. Kumari et al. [101] found that there was increased bioactivity on an LST-treated Ti6Al4V surface. As expected, LST did not produce any cytotoxic substances reflected by an XTT ($C_{22}H_{19}N_7Na_2O_{14}S_2$) assay test. It was shown that cell

adherence preferred ridges and corners and was less present in dimple-textured surfaces (Fig. 2.1.8, *a*), in respect of linear-textured surfaces (Fig. 2.1.8, *b*), cells were preferentially attached along the direction of texturing in the textured zone.

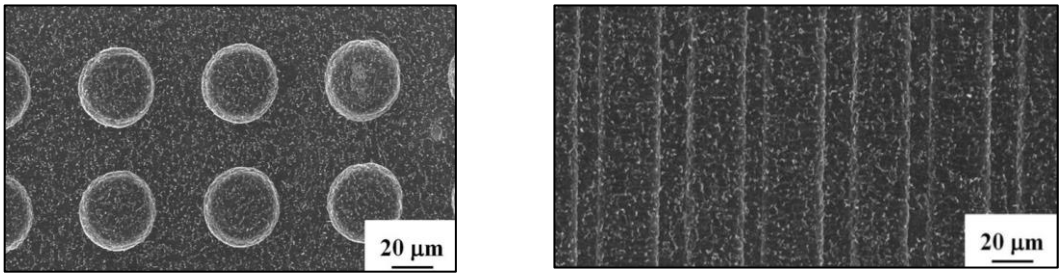

a *b*

Fig. 2.1.8. Scanning electron micrographs of the surface of laser-textured Ti–6Al–4V using an ArF excimer laser in air with *a* – dimple geometry (laser fluence of 3.2 J/cm2, repetition rate of 200 Hz, number of laser pulses of 100) and *b* – linear geometry (laser fluence of 2.4 J/cm^2, repetition rate of 200 Hz, number of laser pulses of N = 50 (pulse overlap in laser scan direction) [101].

Laser surface texturing of an implant can be used for improving surface biocompatibility: cell adhesion, cell spreading, proliferation, actin cytoskeleton and focal adhesion organization [101]–[103], [109]. Anisotropic surface texturing promotes driven cell orientation and cell motility [110]. Initial studies using laser-generated grooves demonstrate that direct-write laser-machined grooves lead to contact guidance for osteoblast cells (Fig. 2.1.9 *a*, *b*) [42], [111]. LST of titanium-based alloys shows no toxic effect and good cell viability [101].

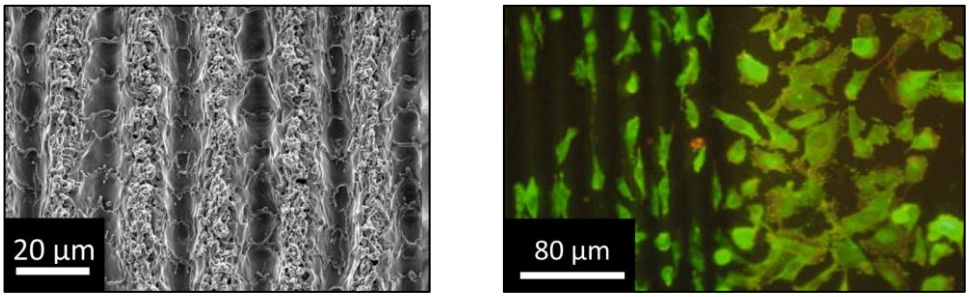

a *b*

Fig. 2.1.9. Titanium-based alloy direct laser texturing for bioapplications: a – demonstration of laser-formed surface grooves; *b* – contact guidance by linear grooves causes elongation of the cells (left) as compared to a polished surface (right). (Images by LaraIonescu) [111].

The behavior of the cells on a surface is largely affected by the amount and direction of stress on the cytoskeleton, which, in turn, depends on the surface chemistry and surface topography. Changing different laser-scanning parameters, such as speed or power, creates different narrower or sharper surface structures. Additional application of external triggering for laser generation gives the possibility to form secondary surface structures. Peak distance on a scanned surface controlled by laser on/off trigger frequency and beam movement speed:

$$l_{trg} = v_{sc}/f_{trg}, \quad (2.4)$$

where l_{trg} – distance between laser spots formed with external trigger, v_{sc} – laser beam scanning speed, f_{trg} – external trigger frequency. At the same time, it is possible to control

the width of the laser-processed segments by laser on/off trigger delay settings. In this way, laser pulse bursts with millisecond intervals of inburst pulses will be formed. Correct combination of laser scanning speed, power and burst length leads to the generation of surface ripples (Fig. 2.1.10). Such laser-induced surface ripples improve the cell attachment and differentiation by 50% [112].

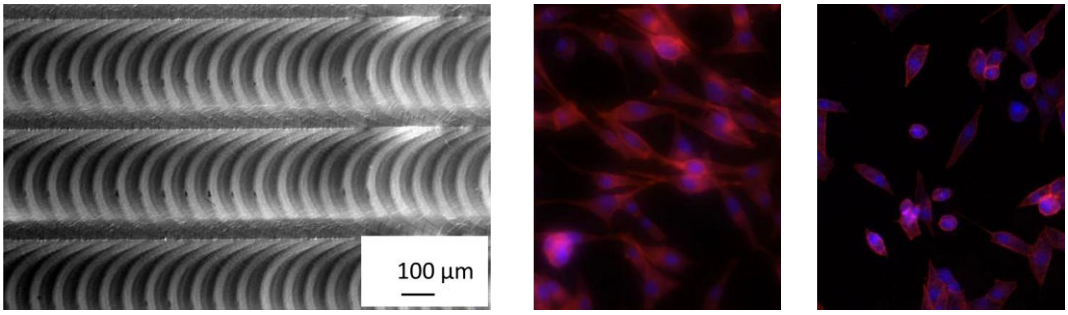

a *b* *c*

Fig. 2.1.10. Laser-triggered formation of ripples inside the grooves, along the direction of laser scan bursts: *a* – grooves formed at constant speed; *b* – cell spread and cytoskeleton structures on burst-textured surface; *c* – cell spread and cytoskeleton structures on untextured surface [112].

As the cell cytoskeleton has low stiffness, getting attached to a surface with sharp features can induce the type of stress, which can be beneficial for cell activities. A surface with such feature dimensions can be effective in influencing the cellular activities on the surface and thus enhancing the biocompatibility.

2.1.5. LST for adhesive bonding

There are several laser adhesive bonding techniques, where the LST plays a key role. The main idea of this technology is to improving adhesion forces by increasing the active area and interlocking the two connected surfaces [113] (Fig. 2.1.11). One popular application of laser surface adhesive bonding is the thermal connection of metal with plastic or composite. In this case, the surface of the metallic substrate should have a specially prepared structure. It can be rows, dimples or an array of random cones [114]–[116].

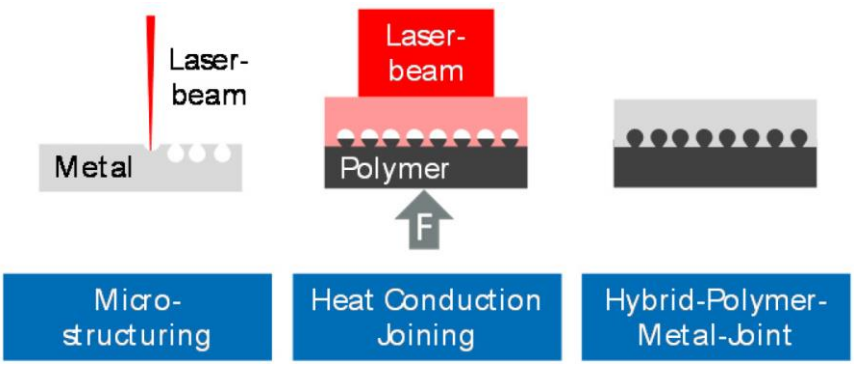

Fig. 2.1.11. Process chain of the laser-based polymer-metal connection [113].

Another application of the laser texturing of a substrate can be found in spray coating technology. Pre-treatment of the material by laser texturing involves physico-chemical and mechanical modification on the surface with a significant increase of the surface contact area between the coating and substrate [117]. Pattern dimensions of LST for thermal spray coating should be chosen depending on the spray process (powder size and material viscosity) [118]. Moreover, correctly choosing the laser texturing strategy gives the possibility to exclude voids [119]. This was demonstrated in an application of nanosecond laser pulses for metal LST for thermal spraying [120], [121]. In this case, incorrect laser parameters leads to the covering of surface texture by recast material and blocking of the laser-drilled holes (Fig. 2.1.12).

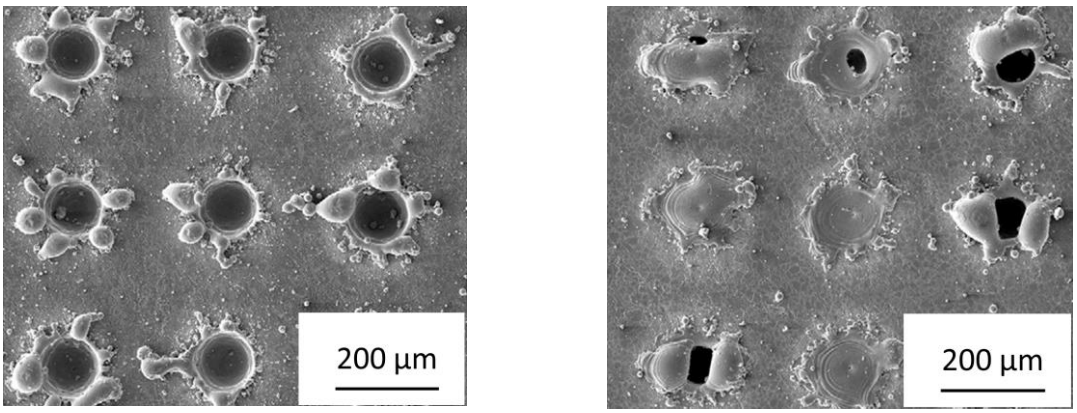

a *b*

Fig. 2.1.12. LST of 1.4401 steel with application of 50 laser pulses per hole: *a* – at fluence 29 J/cm^2 and 40 kHz repetition rate holes stay open; *b* – at fluence 20 J/cm^2 and 56 kHz repetition rate holes are blocked [120].

In the known literature sources, the diameter of the textured holes for thermal spray applications has 60 ÷ 80 µm. Distance between holes is about 100 ÷ 200 µm with depth 30 ÷ 80 µm. Such parameters of the surface texture correspond to the particle volume and the particle diameter [120], [122]. The diameter of the texture's open area needs to be larger than the particle diameter [123]. On the other hand, increasing the holes' diameters makes the filling of the cavities more difficult. This might be due to the fact that the bigger amount of laser surface ablated products goes to fill the cavities during the spraying operation [117]. However, the application of the laser texturing with correct pattern geometry is able to increase the adhesion stress 2 ÷ 3 times [119], [124].

2.2. Physical principles of laser surface processing with ultrashort laser pulses

Ultrashort laser pulse ablation, that is, the removal of matter from solid surfaces, has great interest for experimental and theoretical research [125], [126]. Experiments have shown that with ultrashort irradiation a better controllability and precision in material modification can be achieved as compared to longer pulses [127], [128]. From the theoretical point of view, the ultrashort time of interaction allows the separation of the involved processes as excitation, melting, and material removal. The precise mechanisms of laser ablation for different materials are still debated, especially for ultrashort picosecond and femtosecond laser pulses [125], [129]–[132]. In the following text, the general physical principles of phase transformation and ablation processes under ultrashort laser pulse irradiation will be

discussed. The physical processes of laser pulse interaction with material will be discussed in relation to applied laser pulse intensities.

2.2.1. Thermal energy transfer in ultrashort laser pulse metal ablation

The energy of the irradiating laser is mainly absorbed by the electrons of the solid. The laser therefore initiates a transient non-equilibrium of the electron gas with the lattice [125], [133], [134]. If the intensity of the laser pulse is below the range $\leq 10^{13} - 10^{14}$ W/cm^2, then the free-carrier number density has not achieved the critical value and non-thermal ablation does not appear [125], [129], [135]. In this case, the energy transport from electrons to the lattice can be described by the Two-Temperature Model (TTM) [125], [126], [129], [136], [137]. In the TTM, the laser initiates a transient non-equilibrium of the electron gas with the lattice, which was first noted by S. I. Anisimov et al. [133]. During a short period of a few picoseconds or less, the lattice remains at its considerably lower temperature. The energy exchange between electrons and the lattice can be described by the equations [125], [133], [138]:

$$c_l \frac{\partial T_l}{\partial t} = -c_e \frac{\partial T_e}{\partial t} = \alpha(T_e - T_l), \tag{2.5}$$

where T_e, T_i and c_i, c_e are the electron and lattice temperatures and specific heats, respectively; α is the energy exchange ratio between two subsystems. Temperature changes in the laser irradiated surface are affected by heat transport of energy to both subsystems:

$$c_e \frac{\partial T_e}{\partial t} = div(k_e \nabla T_e) - \alpha(T_e - T_l) + Q, \tag{2.6}$$

and

$$c_l \frac{\partial T_l}{\partial t} = div\left(k_p \nabla T_l\right) + \alpha(T_e - T_l), \tag{2.7}$$

where Q is the laser pulse energy absorbed in a material, and k_e and k_p are thermal conductivities of the electron and phonon subsystems, respectively. Equations 2.5 – 2.7 in combination with electrodynamic, hydrodynamic and solid state physics allows to analyze the ablation process in detail [131], [136], [139], [140]. The TTM model is able to predict time intervals, when the consequent physical mechanism of energy transformation will be activated [132], [141]. Due to the limited value of the energy exchange ratio α between electrons and ions in the metals (Eq. 2.5), the subsystems stay be in a nonequilibrium state more than 10 ps [125]. Heat transfer in such a nonequlibrium state is different from classic thermal diffusion, and it can be described by an specific model, like wave or parallel heat diffusion [142], [143].

2.2.2. Ultrashort laser pulse surface modification at different energy fluencies

When a metal is subjected to an ultrashort light pulse, a fraction of the electrons are excited from below the Fermi energy to above (Fig. 2.2.1) [125], [144]–[146]. Strong interaction between electrons leads to forming local equilibrium in the electron gas at a few femtoseconds. A variety of thermal and structural effects are temporarily gaped from the initial photon absorption by the target (yellow region line in Fig. 2.2.2) in a timescale of tens of picoseconds. Under such early non-thermal processes, the lattice of the target remains intact during the pulse [146]. High-speed phonon emission leads to overheating of the subsurface metal layer at a couple picoseconds to the depth of 100 nm [125], [141], [147]. The

next evaluation of the surface ablation depends on the absorbed energy density [148]. The possible ablation mechanisms will be discussed in the subsequent text ascending to the absorbed energy density.

At energy density slightly higher than the melting threshold ($F \approx 100 \div 170$ mJ/cm^2), the overheated subsurface layer has a temperature of more than $T_s = 1.5 \cdot T_m$ and has no temperature gradient, due to ballistic electron transport [125], [147], [149], [150]. As a result, the overheated crystal lattice will be melted by homogeneous nucleation of the liquid phase in the bulk of a highly superheated solid [149]. Such fast resolidification of the metal surface can be used for forming a new phase of the solid called metallic glass [132]. In this process, the laser-induced periodic surface structures (LIPSS) might occur because of laser beam interaction with scattered light or by hydrodynamic effects [130], [151], [152].

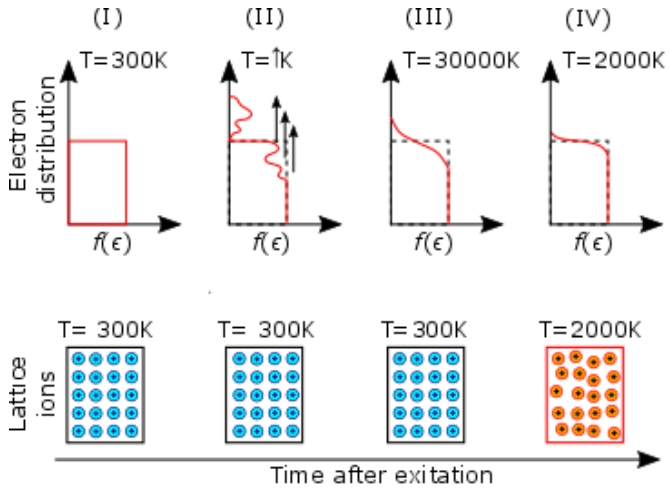

Fig. 2.2.1. The physical mechanism of laser ultrashort pulse electron excitation in metals: initial state of electron gas (I), rapid generation of non-equilibrium state by ultrashort laser pulse (II), electron thermalization to a new high temperature state (III), energy transfer to the lattice at a few picoseconds (IV) [125], [144].

For intensities close to 170÷200 mJ/cm^2, the fast homogeneous melting can be followed by a much slower heterogeneous melting. As a result, the additional 15÷50 nm layer within ~500 ps will be melted and resolidified in several nanoseconds (Fig. 2.2.2.) [153]–[155]. Such a high speed of the resolidification initiates high tensile stresses and photomechanical spallation of surface layers [136], [153], [156].

At energy densities higher than 200 mJ/cm^2 and laser pulse intensities $\leq 10^{13}$ W/cm^2, a temperature can be reached up to the region of overcritical fluid formation [141], [146], [157], [158]. In this case, ablation will start at 20÷100 picoseconds after laser excitation, due to the time of energy transfer from electrons to lattice ions [150], [159], [160]. The dynamic of surface explosion was measured in a series of experiments with detection of Newton rings (Fig. 2.2.3) [150], [159], [160]. It was shown that ultrafast solid-to-liquid phase transition appears in the first few hundreds femtoseconds [150]. But material expansion is detected at a later time, after 10÷20 picoseconds [145], [150], [159]. Exposed materials are able to achieve

a great speed, more than 8÷10 km/s [136], [161]–[163]. The ablation plume ejected at the highest speed in the phase explosion regime and contained atomic clusters in the front part of the plume. The following part of the ablated plume has slower medium-size clusters (up to 10,000 atoms) that have ejection velocities of less than 4 km/s and droplets that are slower than 3 km/s [136]. The pressure in the front shock wave typically has 100÷200 atm and decays close to ambient pressure at about 100 ns [164]. Under the ablated area remains thin remelted layer with a number of point defects and dislocations produced by ultrafast cooling [130], [165].

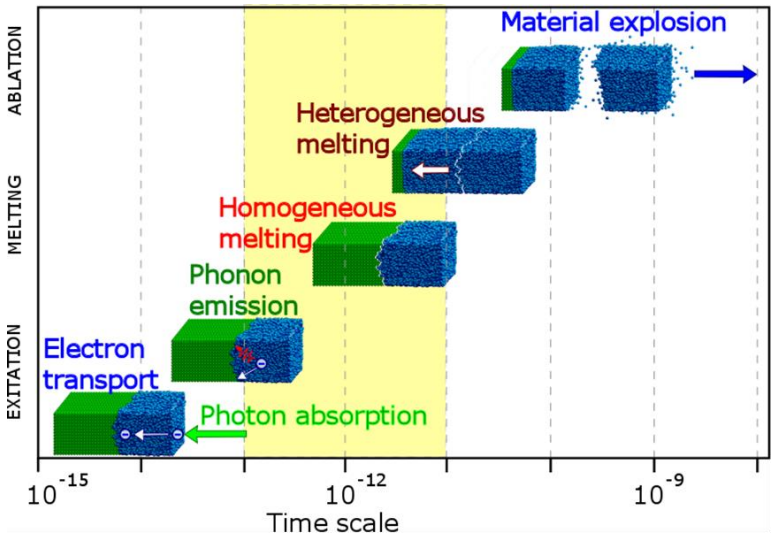

Fig. 2.2.2. Scheme of early processes during laser-metal interaction (adapted from [166]).

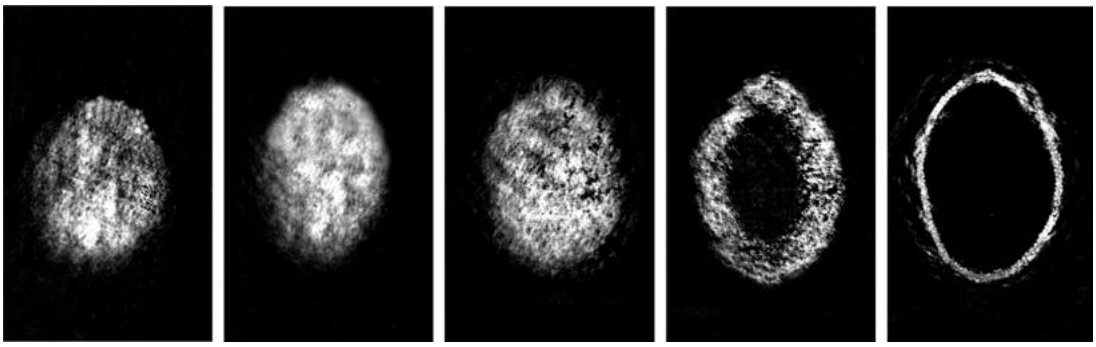

Fig. 2.2.3. Snapshots of the Newton rings formed after 35 fs laser pulse ablation (energy density 1.5 J/cm^2). The surface deformation and the first Newton ring forming is detected at 10 ps after laser pulse irradiation. See detailed information in the source [145].

At the higher laser pulse intensities $\geq 10^{13} - 10^{14}$ W/cm^2 ($\geq$1 J/cm^2 in femtosecond laser pulses), it becomes possible to achieve electrostatic laser ablation of a material [135], [146], [153], [155]. It is an extreme non-equilibrium and non-thermal mechanism of metal ablation

removal when the energy of the electrons is much higher than the lattice ions' temperature ($k_B T_e \gg k_B T_l$) [167]. The energetic electrons escape the solid and create a strong electric field due to charge separation from the parent ions. It should be underlined that electrostatic ion removal has a different nature from the Coulomb explosion, when electrons are swiftly, faster than the Coulomb force action, removed from the parent ions [146]. The electrostatic ablation process occurs in time shorter than the plasma expansion time, the heat conduction time and the electron-to-ion energy transfer time [135], [167].

High-speed plasma expansion initiates great subsurface stresses, more than 10 ÷ 20 GPa, which is higher than the ultimate tensile strength for most materials [125], [146], [164]. The pressure shock wave causes plastic deformation of subsurface layers and the generation of dislocation nets [168], [169]. Such material processing leads to increasing surface hardness up to four times [170]–[172]. This laser pulse stimulated surface hardening is called laser shock peening (LSP) and it is widely used in industrial applications [173], [174].

Afterwards, the laser-irradiated surface contains an upper resolidified layer with some amount of point defects and a subsurface plasticity shock wave deformed layer [130], [165], [168], [175]. The ablated plasma plume and following vapor explosion create a shielding effect, when the irradiated surface remains covered by ablation products at 2 ÷ 3 μs [157], [163]. Then the output laser-irradiated surface will be contaminated by precipitation of the shielding dissipation products and associated oxidation of the upper surface layers [176]–[178]. In most cases, the surface ablation process has a semi-thermal character ($k_B T_i \geq \varepsilon_b$), for example by Gaussian distribution of energy in the laser spot. In this case, even the ultrashort laser-pulse irradiation is able to leave residual heat in the subsurface layer by secondary effects: heat conductivity from upper layers, ballistic and diffusion effects, convective and radiating energy exchange between the ambient and solid target, and shock wave spreading [134], [136], [146], [176], [179]. These residual effects have a great influence on the quality and efficiency of LST in a high-repetition multi-pulse regime. The influence of laser pulse parameters and residual effects on LST will be discussed in the follow section.

2.2.3. Efficiency and quality of LST with ultrashort laser pulses

The laser microstructuring manifests between the efficiency and quality of processed surface. Correction of pulse duration is one of the possible ways to optimize the laser-processing parameters. It should to be noted that a bigger ablation depth will be achieved by deeper thermal penetration at longer laser pulses (ns ÷ μs). But in this case the main part of the material will be ablated by undesired thermal effects with deeper material melting [128]. Ultrashort laser pulse (ps ÷ fs) material processing will reduce thermal damage and melt accretions of the workpiece [128]. The efficiency of the ultrashort laser-induced material ablation depends on the ablated volume per laser pulse [180], [181]:

$$\Delta V = \frac{1}{4} \cdot \pi \cdot \omega^2 \cdot \delta \cdot ln^2 \left(\frac{F_0}{F_{th}}\right), \tag{2.8}$$

where ΔV – ablated volume, ω – spot radius, δ – penetration depth, F_0 – fluence in the center of the laser beam, and F_{th} – threshold laser fluence. The ablation efficiency can be evaluated as ablated volume per time unit or per applied energy. At short and ultrashort laser pulses the

efficiency directly depends on penetration depth. The penetration depth of the laser pulse energy can be realized in two ways, optically and thermally [136], [179]:

$$\delta = l_a + l_{th}, \tag{2.9}$$

where l_a – absorption depth and l_{th} – thermal penetration depth. In the case of the short laser pulses, the absorption depth of the laser energy is about tens of nanometers for metallic surfaces and it is much smaller than the thermal penetration depth. But for ultrashort laser pulses the ballistic electrons should be taken into account. It is possible to do this with a simple approximation that the ballistic electrons merely contribute to the heat-penetration length. The laser energy distribution term in the irradiated surface then becomes [182]:

$$Q_{th} = \frac{AI(t)e^{-2r^2/\omega^2}e^{-z/(l_a+\lambda_{\text{ball}})}}{l_a+\lambda_{\text{ball}}}, \tag{2.10}$$

where A – is the absorptivity of the surface, $I(t)$ – the distribution of the laser intensity in a laser pulse, r – the distance from the laser spot center, λ_{ball} – the ballistic electron penetration depth and z – the depth coordinate inside of the irradiated sample. The energy transport by ballistic electrons increases the penetration depth up to hundreds of nanometers and this was confirmed by experiments with ablation depth detection [182]. Deeper injection of the energy inside of the irradiated metal may explain the significant decrease of the threshold laser fluence and better ablation efficiency for ultrashort laser pulses [135], [181], [183]–[185] (Fig. 2.2.4). A further reduction of pulse duration below 10 ps is expected without significant effect on thermal behavior for metals, but shorter laser pulses are able to activate nonlinear effects. The nonlinear effects can be undesired due to the decreased precision of laser surface processing [179].

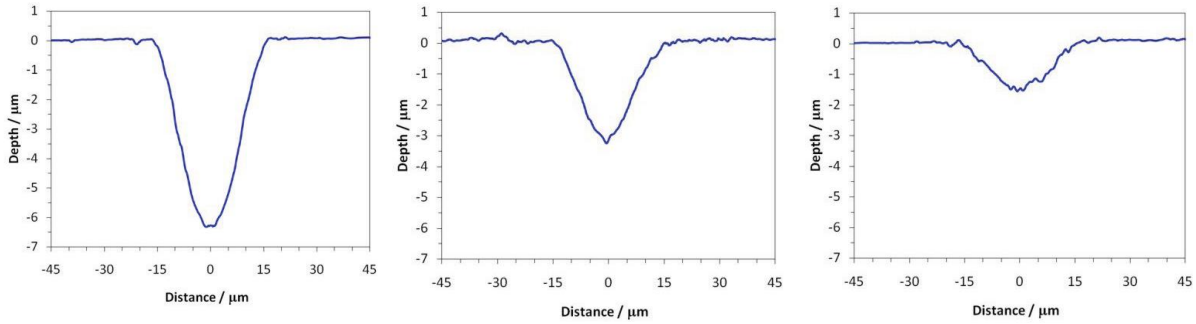

a *b* *c*

Fig. 2.2.4 Penetration depth detected by cross-section of a scanned line for AISI304 steel versus pulse duration at fluence 3.62 J/cm^2 and fixed scanning speed: *a* – penetration depth at 10 ps; *b* – penetration depth at 30 ps; *c* – penetration depth at 50 ps [183].

The TTM is able to predict logarithmic dependency between absorbed fluence F_a of the laser pulse, the laser pulse penetration depth and the ablation depth z_{abl} [126], [134]:

$$z_{abl} = \delta \cdot \ln\left({}^{F_a}/_{F_{th}}\right). \tag{2.11}$$

The threshold fluence F_{th} is described as the minimum energy which is needed to ablate material. For the metals the threshold fluence varies between 0.5 J/cm^2 for stainless steel and 1.7 J/cm^2 for copper [186].

The penetration depth and threshold fluence are parameters of the material and they are depend on the surface state and structure. The laser pulse interaction with the material involves a lot of physical changes on the surface and in the subsurface layer of the material [130], [153], [165], [187]–[191]. Repeated application of laser pulses on the same surface has several advantages for effective material processing. Laser irradiation of the surface is able to increase the surface absorptivity several times [59], [98], [159], [192], [193]. Häfner et al. found that the absorptivity significantly increases already after the second pulse application. At a higher number of applied laser pulses, up to $N = 1000$, the absorptivity will be increased seven times, due to incubation effects [19]. The absorptivity of the surface has a strong influence on the depth distribution of the laser pulse energy in subsurface layers of irradiated material (see Eq. 2.10.). Increasing the laser pulse number induces a decrease of the threshold fluence ten times and more [20], [183], [192], [194] (Fig. 2.2.5, *a*). Decreasing the threshold fluence with a higher number of laser pulses is defined in exponent form [181]:

$$F_{th}(N) = F_{th}(1) \cdot N^{S-1}, \tag{2.12}$$

where $F_{th}(N)$ – threshold fluence after N pulses, N – number of applied laser pulses, $F_{th}(1)$ – the single shot ablation threshold and S – the incubation coefficient. The typical value for metals is $S = 0.8 \div 0.9$ [186]. The reason for the incubation effects with multipulse laser material ablation is described as the accumulation of subsurface defects from pulse to pulse [183], [195]. The incubation effects can be increased at higher repetition rates with microsecond intervals between laser pulses [183], [194] (Fig. 2.2.5, *b*).

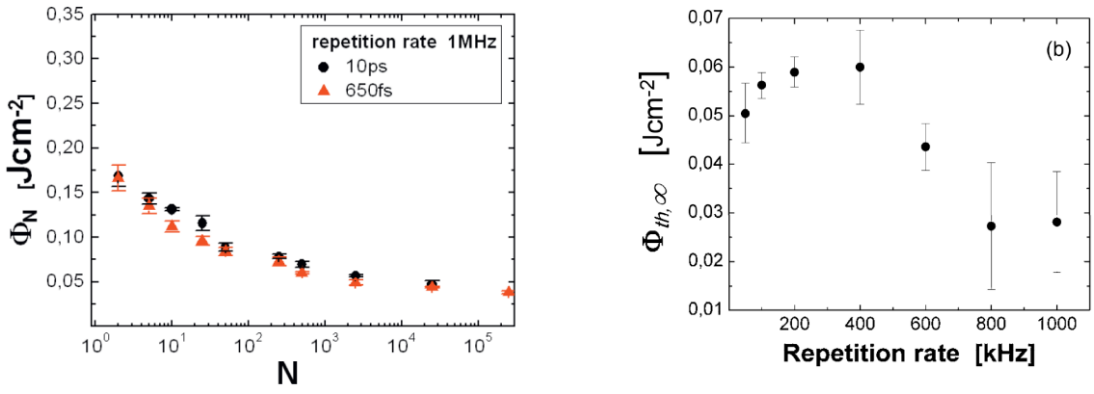

a *b*

Fig. 2.2.5. Decreasing threshold fluence during multipulse laser ablation of stainless steel: *a* – decreasing fluence threshold depend on the laser pulse number (pulse duration 650 fs and 10 ps at 1 MHz) [192]; *b* – decreasing fluence threshold at infinity pulse number as a function of repetition rate (pulse duration 10 ps) [194].

2.2.4. Heat accumulation in ultrashort laser surface ablation

The reason for decreasing threshold fluence during multipulse material processing was suggested as a heaping of laser-induced defects and heat accumulation [14], [20], [181], [186], [194], [196]. When the repetition rate becomes higher, then the heat accumulation leads to a

decrease in of surface quality and processing efficiency. The reason for such a negative influence of heat accumulation lies in the undesired increase in residual surface temperature higher than melting or boiling point [197]. Uncontrolled heat accumulation at a very high repetition rate and low scanning speed leads to the onset of melting, oxidation, and pileup of material [14], [198]–[200].

There are several research results where a higher efficiency was determined to be a result of material processing at optimal high repetition rates [201]–[204]. It was found that the efficiency has a maximum at a specific repetition rate and this was explained by the beneficial change in the thermo-physical properties of the preheated surface state after a previous laser pulse and before the next one in the pulses sequence [3], [203], [204]. Reaching the maximal ablation efficiency is highly material dependent and it can be described as positive heat accumulation [205]. For steel, a major positive effect (+80%) was detected at frequencies up to 2 MHz (Fig. 2.2.6., *a*) [204], [206]. Moreover, there are some papers where it was noted that a higher repetition of laser pulses leads to achieving a higher quality of the laser-processed surface (Fig. 2.2.6., *b*) [207]–[210]. The achievement of a smoother output surface at higher repetition rates is not fully explained yet. One of the possible mechanisms of surface smoothing is described as a result of thermo-fluidic phenomena with material replacement, driven by temperature gradients [21], [211]. The other parameters of the laser surface processing, such as fluence or laser spot spacing, should be taken into account for optimization of the ablation process [210], [212].

The residual temperature after application of one laser pulse can to be determined from this well-known heat conduction equation [14], [213], [214]:

$$\Delta T = \frac{Q_r}{\rho \cdot c_p \sqrt{(4 \cdot \pi \cdot \alpha_{th} \cdot t)^{n_g}}} \cdot e^{-\frac{r_s^2}{4 \cdot \alpha_{th} \cdot t}}, \tag{2.13}$$

where ΔT – residual temperature after laser pulse, Q_r – residual energy absorbed by the material after material ablation, r_s – distance from the heat source, c_p – specific heat capacity, ρ – mass density, $\alpha_{th} = k/(\rho \cdot c_p)$ – thermal diffusivity, k – thermal conductivity, t – time after laser pulse irradiation and n_g – parameter of the laser spot geometry (equals 1 for flat heat flow, equals 2 for elongated heat source and equals 3 for point heat source). The heat accumulation is determined as the sum of the residual heat from all laser pulses in a laser pulse sequence [14], [198]:

$$T(r,t) = \sum_{i=0}^{N_f} \Delta T_i \left(r,\ t + i \cdot {}^{1}/_{f_{pulse}} \right), \tag{2.14}$$

where $T(r,t)$ – temperature in the point r at the time moment t, N_f – full number of the laser pulses in the pulse sequence, ΔT_i – residual temperature after i-th laser pulse and f_{pulse} – laser pulse generation frequency. The calculated temperature increase due to the heat accumulation under pulsed laser beam scanning gives the possibility to evaluate the critical saturation temperature for AISI 304 stainless steel equal to $T_{th} = 607$ °C. At this temperature, the character of the laser surface machining is changed and the output surface becomes smoothed (Fig. 2.2.7) [215].

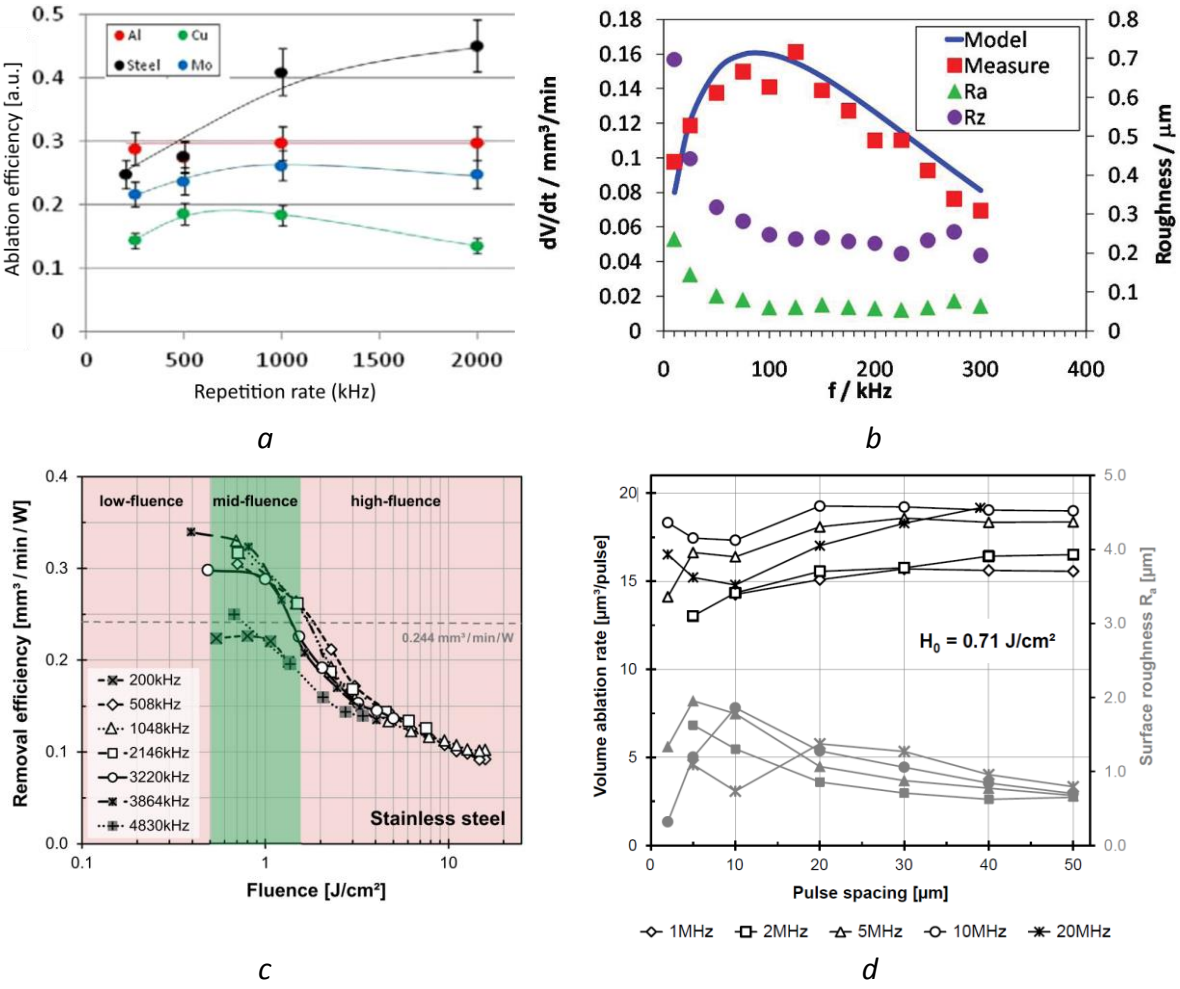

Fig. 2.2.6. Influence of positive heat accumulation on ultrashort laser pulse processing of metals: *a* – ablation efficiency as a function of repetition rate (kHz) for stainless steel, aluminum, copper, and molybdenum [204]; *b* – roughness versus the repetition rate, copper [183]; *c* – decrease of efficiency at higher fluencies [212]; *d* – efficiency and roughness at different laser spot overlapping, stainless steel (2ω = 58 µm, λ = 1064 nm, P = 270 W, τ = 10 ps, maximal pulse energy 180 µJ) [210].

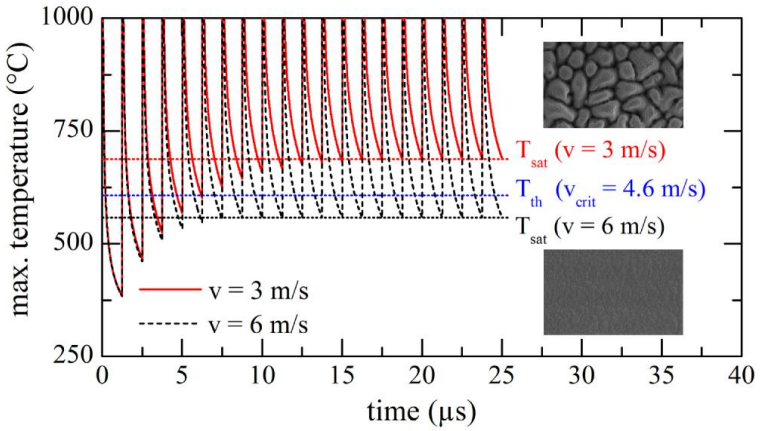

Fig. 2.2.7. Maximum temperature value plotted as a function of time for a fluence of 0.37 J/cm^2, a spot diameter of 50 µm, a repetition rate of 800 kHz and different scanning speeds [215].

The pulse overlap is another important parameter for quality surface processing with ultrashort laser pulses [206], [210]. The spatial overlap P_o is defined by scanning speed v_{sc} and laser pulse frequency f_{pulse} [168]:

$$P_o = 1 - \frac{v_{sc}}{2\omega \cdot f_{pulse}}. \quad (2.15)$$

There are many studies provided for determination of an optimal value of overlapping between laser pulses [16], [209], [212], [216]–[218]. In the detailed study of Jaeggi et al., it has been shown that minimum surface roughness is achieved with a distance from pulse to pulse of half to one spot radius, i.e. a spatial overlap of 50 - 75% [219]. The optimal pulse overlapping is described as a basic limitation for application of high-power lasers, due to the limited scanning speed [181].

In most cases, the experimental evaluation of heat accumulation and laser pulse overlapping was controlled by microscopy or profilometry [56], [198], [220]–[222]. Whereas it is possible to determine the laser pulse overlapping directly by microscopy, the heat accumulation is evaluated indirectly by EDX measurements of oxygen concentration, surface relief evaluation or deformation of the laser-processed substrate [14], [194], [198], [199], [220].

Direct monitoring of heat processes initiated by laser irradiation was performed using IR photodiodes. The pioneer work of noncontact direct detection of temperature changes under laser pulse with a Ge photodiode was provided by Xu Xianfan et al. [223], [224]. The main idea of such measurements lies in evaluation of the IR signal emitted from a laser-irradiated surface [225]. Laser-induced changes of the phase composition of the surface, the IR emissivity and plasma emission affect the waveform of the IR response. Analysis of IR signals gives the possibility to detect characteristic peaks and plateaus on time dependences of the IR response. J. Martan et al. [226], [227] have used this technique for investigation of laser melting of Cu, Mo, Ni, Si, Sn, Ti, steel 15330 and stainless steel 17246 samples. The laser beam

from a KrF excimer laser ($\lambda = 248$ nm, $t_p = 27$ ns) was homogenized and focused on a surface in a spot with a 2.1×1.8 mm area (Fig. 2.2.8). The IR signal was detected by a liquid-nitrogen-cooled HgCdTe photodiode. This photodiode detector, battery-powered and coupled with a Ge filter, has sensitivity in the spectral range 1.8-12 µm, with the frequency range DC-100 MHz. The IR radiation signal was recorded by a digital oscilloscope. Additionally, the signal from a reflected He-Ne CW laser was recorded by a photodiode with a narrow-band interference filter. Solidification of the laser-melted surface was detected as plateaus in the nanosecond resolved record of the IR radiation signal which appeared after laser irradiation.

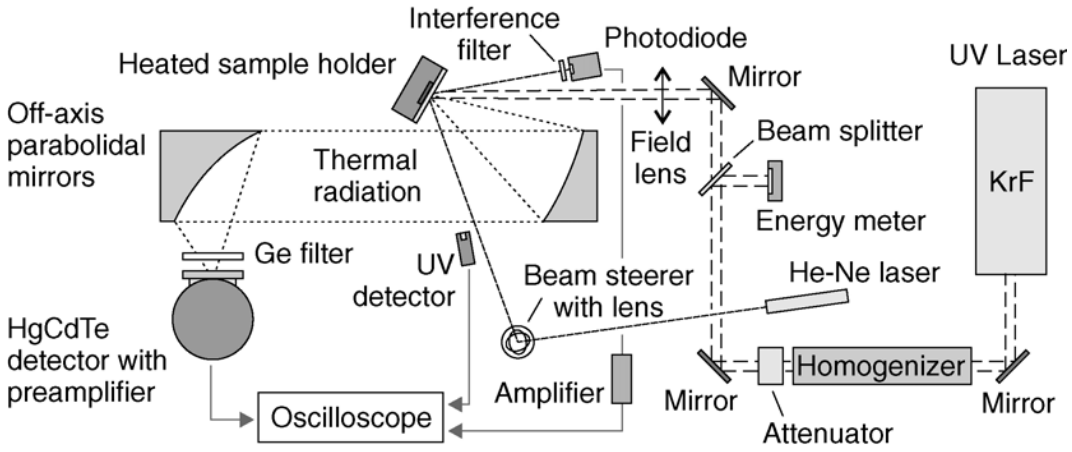

Fig. 2.2.8 Schematic representation of the experimental system for detection of the melted phase using a KrF excimer laser [226]

In later studies, the process of metal resolidification of stainless steel under nanosecond laser pulses was performed with two fast PIN Si photodiodes [228]. The benefits of application of the PIN Si photodiodes are a higher response frequency, up to 500 MHz, and not needing to use liquid-nitrogen cooling. The IR signal was recorded by a SI PIN photodiode (Hamamatsu S5052) with a short-pass filter FES1000. The triggering of IR recording was provided by a second PIN Si fast photodiode without optical filter. The measurement system with two PIN Si photodiodes and a galvanometer scanning head was applied for providing time-resolved temperature tracking of the laser marking process. Similar to previous studies [226], the crystallization process was identified by detection of plateaus on a IR time-resolved signal. Application of this method allows one to explain the optimal parameters for corrosion resistant laser marking of stainless steel.

2.3. Scanning methods for providing LST

2.3.1. Scanning techniques applied for LST

Increasing the throughput of LST technology stimulates development of new strategies for high-speed laser surface processing. There are several scanning technologies for high-

speed laser beam deflection: galvo scanners, polygon scanners, piezo scanners, static and resonant scanners, micro-lens scanners, electro-optic deflectors (EOD) and acousto-optic deflectors (AOD) [221], [229], [230]. The inertial scanning systems have a maximal deflection angle and number of resolvable spots on the scanned surface [229]. There are two traditional techniques for high-speed laser surface machining with a large processing area – galvanometer beam scanning and polygon optical scanning systems (Fig. 2.3.1) [231], [232]. The maximal scanning speed of the available galvanometer scanners lies in the range 10 ÷ 40 m/s, whereas the polygon scanner is able to achieve a scanning speed of more than 1000 m/s [233]–[235]. The higher speed of the polygon scanners is a great benefit for fast provision of LST on large areas. However, the polygon scanners do not provide the smooth wall profiles of vector scans for cutting circumference or trepanning large holes, greater than 50 − 150 µm. The laser beam deflection in polygon scanners should be corrected by an additional galvanometer scanner. For LST, when the processed area is smaller than 15% of the working field, the polygon scanners are not cost-efficient and alternative techniques will be more suitable [234]. Correct choice of the scanning strategy helps to improve the laser-processed surface quality and precision of the laser pulse delivery.

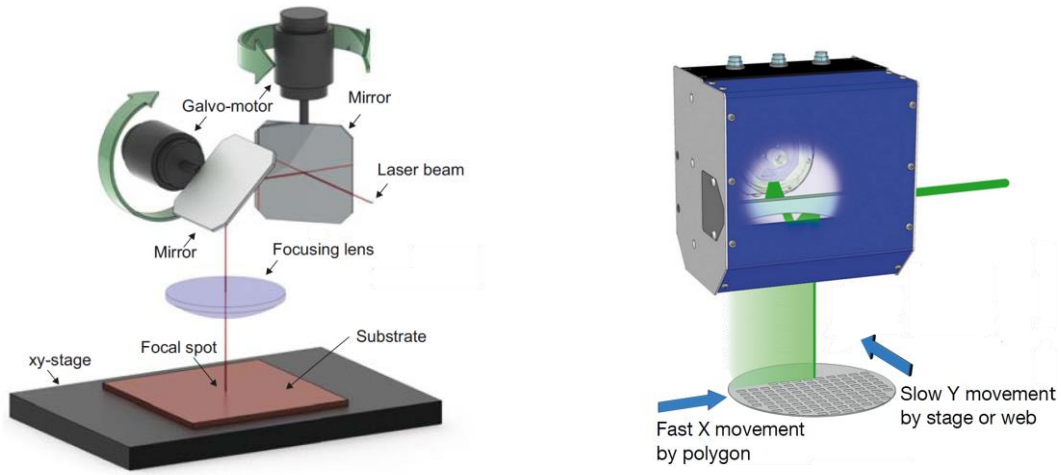

a *b*

Fig. 2.3.1. Inertial laser scanning systems *a*) galvanometer scanner *b*) polygon scanning technique (adapted from [229], [231]).

The output processing rate of LST is depends on a favorable choice of the combination of the scanning strategy with different scanning techniques (see Appendix A, rows 1 and 2). The maximal processing rate of 9000 cm^2/min for direct laser interference patterning (DLIP) was found by a team from Fraunhofer Institute IWS [236]–[239]. The period and distribution of laser surface textured objects with DLIP is directly dependent on the wavelength of the laser beam [240]. This limitation makes it difficult to apply the DLIP for texturing surfaces in cases of irregular structure or complex nonsymmetrical textures. It was shown that a combination of the DLIP technique with dynamic systems decreases the processing rate down to 0.7÷10 cm^2/min [241], [242]. The benefit of the combination of DLIP

with regular micro-texturing techniques gives the possibility to create unique hierarchical structures [242].

Submicron surface structures might be created by laser scanning formation of LIPSS [243]. In this case, the laser scanning parameters, such as laser spot overlapping and scanning speed, have a key role for highly regular LIPSS (see Appendix A, rows 3 and 16). The achieved processing rate for LIPSS formation directly depends on the applied scanning speed. For example, I. Gnilitskyi et al. [244] have reported processing rate of LIPSS forming on stainless steel equal to 6.3 cm^2/min with scanning speed 3 m/s. The last study predicts several times higher processing rates with polygon scanners [245]. LIPSS forming is competitive with industrial standards of nano-manufacturing (~1 cm^2 in 10 s) [41]. Like the DILP technique, LIPSS might be applied for formation of hierarchical surface structures in combination with micro-texturing. But, in this solution the period of the upper LIPSS is smaller than half of the laser wavelength [41].

Another highly productive LST strategy is forming an array of microobjects by dividing the laser beam with diffraction or shadow masks [217], [246]–[248] (see Appendix A, rows 12 and 17). This scanning strategy is used in cases when the pulse energy is high enough to divide into several beams. The distance between laser spots is given by mask parameters. In the case of application of a solid state static mask, the spot distance is constant and part of the laser beam energy will be lost. Application of spatial light modulators (SLMs) gives the possibility to change the laser spot distribution of the scanning process, but the average power will be limited to under 300 W [249]. However, a processing rate of up to 1800 ÷ 5400 cm^2/min in a multibeam scanning solution can be achieved [249], [250].

LST by straight hatch lines is the most suitable strategy for the polygon scanner technology (see Appendix A, rows 13 – 16). In this case the laser beam scanning speed achieves high values, up to 800÷2000 m/s [210]. The polygon scanner has several times higher throughput in comparison to galvanometer scanners [211]. But providing LST with a polygon scanner needs to involve a correlation between mirror position and laser pulse generation for precise formation of microobjects. This imposes a restriction on the scanning speed for LST. The maximal processing rates up to 7680 cm^2/min were achieved for linear texture and this was done at 320 m/s [251]. But for polygon scanners, the problem of processing arrays of microobjects with specific geometry remains unresolved [252]. It is difficult to control laser drilling of microobjects with high-speed scanning, because there is a lot of data about large arrays with small objects or microobjects, up to 800 MB per second [235]. Additionally, there is not enough time for precise control of laser spot distribution inside every microobject in the array. Moreover, the ultra-high-speed laser beam processing with polygon scanning involves artefacts like jitter, banding, bow and other problems characteristic for these systems. These artefacts involve two components: periodical and random. There are several hardware techniques for reduction of polygon scanner artefacts, but known classic methods of laser beam processing of the array of objects in ultra-fast scanning systems do not have a fully finished solution of the mentioned problems and scanning techniques still must be improved [252], [253].

The galvanometer scanner has a possibility to create curved lines purposefully with the fast swinging of two deflection mirrors (Fig.2.3.1, *a*). This technique was applied in direct laser formation of an array of microobjects with different structures (see Appendix A, rows 6 – 11). The galvanometer scanner is able to achieve a processing rate up to 428 cm^2/min for forming an array of microobjects with a one-beam simple scanning technique at one pulse per object [254]. The high precision formation of surface structures with hatch filling of more complex microobjects reduces the processing rate down to 25 cm^2/min [255]. Noticeable higher processing rates with galvanometer scanners might be achieved by splitting the laser beam into several spots. In this case, a processing rate of up to 5400 cm^2/min is reached. A multibeam solution has potential for industrial applications, especially where there is a need to create a wide array of periodical surface microstructures [249].

2.3.2. Classic methods of laser beam scanning

The precision of laser surface machining is reached by continuous control of the laser beam movement. Mirrors' inertia in galvanometer scan heads requires additional time for acceleration and deceleration. Incorrect delays in laser switching on and off leads to floating of the overlapping at the edges of the scanning paths (Fig. 2.3.2, *a*). Correction on the laser path edges is provided by sky-writing or by additional synchronization between laser mirror position and laser pulse generation. Strong correction between laser pulse delivery and scanning mirrors' position improves the precision of LST close to 1÷2 µm [221], [233] (Fig. 2.3.2, b - c). On the other hand, every additional correction of the scanning parameters may lead to escalation of the processing time up to 50% [233], [256].

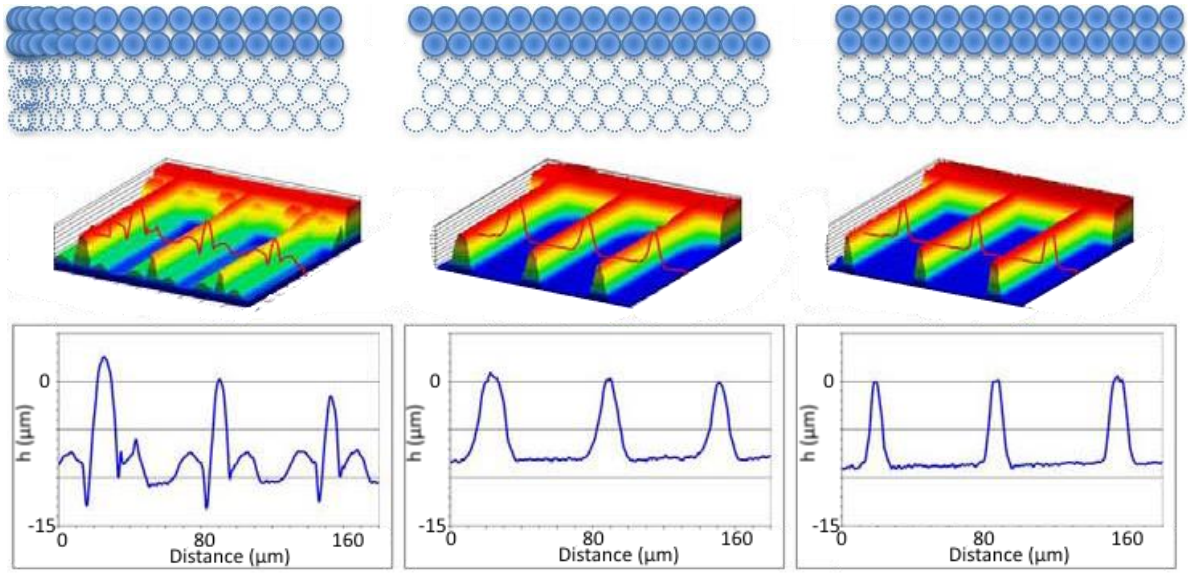

Fig. 2.3.2. Precision and quality of bar texturing (from top to bottom: laser spots disposition, 3D and section profilometry): *a*) without sky-writing; *b*) with sky-writing; *c*) synchronized system (10 ps, diameter 5.7 µm, 120 mW, 300 kHz, 1 µm pitch, 60 layers) [219], [220].

The quality of laser surface machining also depends on the applied laser beam paths' arrangement [193], [257], [258]. There are several main scanning strategies for filling the laser-textured objects by laser spots: straight hatching, path filling, interlaced filling, criss-cross texturing, unidirectional or bidirectional scanning, angular hatching, wobble scanning and their combinations [199], [200], [221], [237], [259]–[263] (Fig. 2.3.3.).

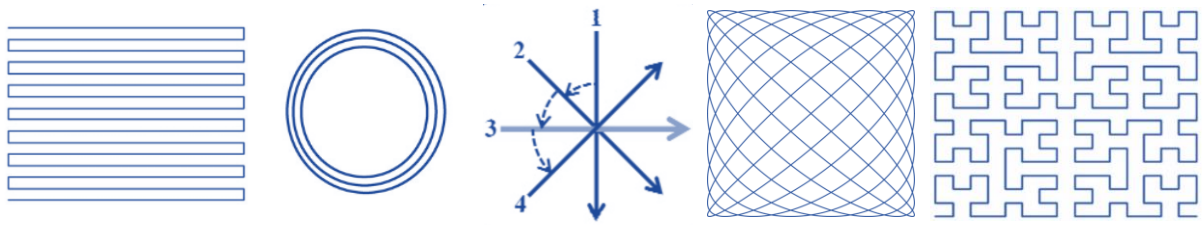

Fig. 2.3.3 Scanning strategies for laser surface machining with different laser beam movement arrangements (adapted from references): *a*) straight line hatching [264], *b*) path filling [200], *c*) angular hatching [262], *d*) filling by Lissajous carves [263], *e*) filling by Hilbert curves hatching [264].

The correct choice of scanning method significantly affects the efficiency and quality of laser material processing. Dold [263] has provided a detailed study of the influence the different scanning strategies on the ablation rate, roughness and processing time of the laser surface machining (Fig. 2.3.4).

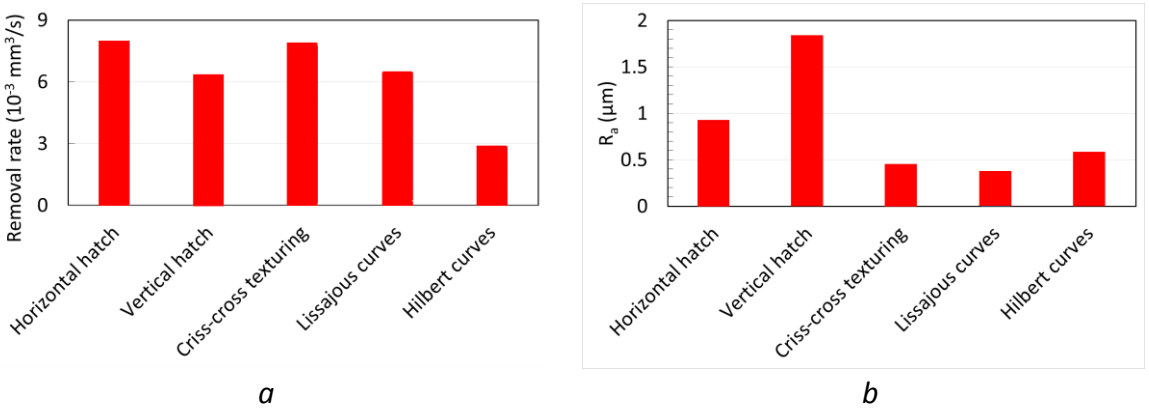

Fig. 2.3.4 Evaluation of different hatch geometries: *a*) matter removal rate; *b*) average roughness analysis (4.5 W, 800 kHz, τ_p = 10 ps, diameter 34 µm, 0.63 J/cm^2, hatch overlap 1.7 µm, 25 scans. Adapted from [263]).

It was shown that the highest efficiency of laser surface processing with scanning by straight hatching lines has more than two times higher efficiency in comparison to fractal filling. The quality of a laser processed surface depends not just on the laser beam filling strategy, but on the direction of the scanned lines – is it in a vertical or horizontal direction.

This distinguishing feature of horizontal and vertical directions can be explained by the difference in the dynamics of X-scanning and Y-scanning galvanometer mirrors.

2.3.3. Interlaced method of laser beam scanning

The distance between hatching lines and their ordering becomes important in the case of laser machining of temperature sensitive materials. For example, in selective laser melting (SLM) technology, composite materials treatment, and formation of biocompatible structures [14], [265]–[267]. There is not only heat accumulation between inline laser spots responsible for the thermally damaged results. There are several types of heat accumulation leading to material damage: pulse-to-pulse-, rerun-, and geometry-density heat accumulation [268]–[270]. Overcoming the heat accumulation at high repetition rates of laser pulse surface processing can be achieved with the interlaced mode, when scanning lines do not have sequential ordering (Fig. 2.3.5) [199], [260], [271]. Application of the interlaced scanning method is able to improve the ablation rate up to 13 times in comparison to the classic sequential method (Fig. 2.3.6, *a*).

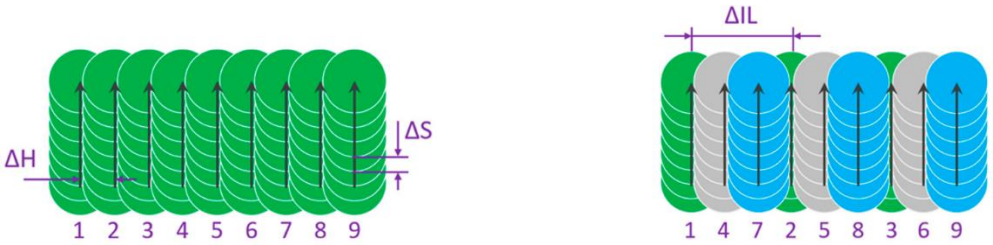

a *b*

Fig. 2.3.5 Straight line laser scanning strategies: *a*) classic unidirectional sequential; *b*) unidirectional interlaced. Meaning of symbols: ΔH – hatch distance; ΔS – distance between pulses in the laser beam scan direction; ΔIL – interlace distance [260].

The interlaced method of laser beam surface scanning of stainless steel was studied by Neuenschwander et al. [199]. In the interlaced method, the distance between laser spots is the same as for classic scanning methods, but the time interval much longer. With the interlaced method, the time interval is not equal to the period of the laser pulses, but it is given by the full scanning time of one pattern. The classic sequential surface scanning initiates heat accumulation and the processed surface is damaged by cavity formation (Fig. 2.3.6, *b*). Unlike with classic method, a surface machined with the interlaced method with the same spot distance between two neighboring spots shows a good surface quality (Fig. 2.3.6, *c*).

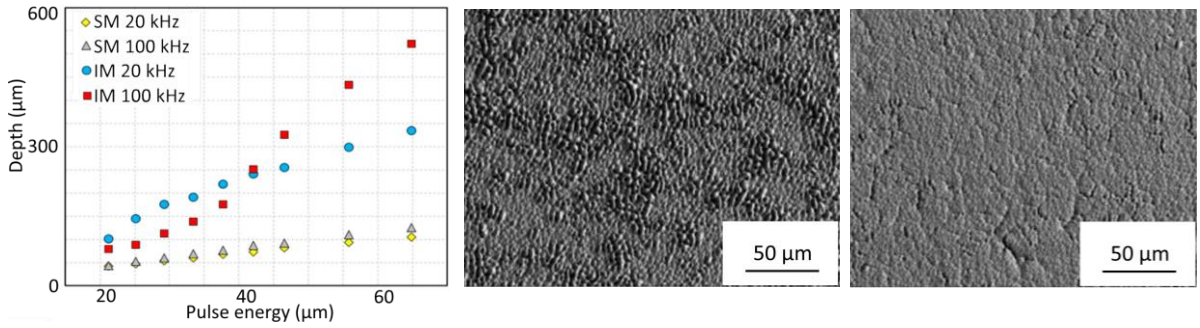

a *b* *c*

Fig. 2.3.6 Application of the interlaced scanning method with a polygon scanner: *a* – increasing the ablation rate 13 times as compared to the classic sequential method (adapted from [260]); *b* – surface machined with a pitch 4.9 µm with the sequential method *c*) surface machined with a pitch 9.8 µm with four interlaced patterns [199].

It can be concluded that the interlaced method has great potential for laser surface processing with high repetition rates of several 10 MHz. For overcoming heat accumulation, the lateral distribution of the laser spots should be comparable to the laser spot diameter. It requires great scanning speeds – several hundred meters per second. At such scanning speeds laser switching for controllable pulse picking will definitely not be possible any more [199], [259].

2.4. Summary of the literature review

The literature overview presented in this chapter has shown the wide area for application of laser-textured surfaces in biology, materials engineering, medicine, optics, semiconductor electronics, etc. Although there are some exceptions, the one feature the laser micro-textured functional surfaces have in common: periodic distribution of the laser-formed microobjects with equal geometry. The three main types of laser-formed microobjects for surface micro-texturing can be identified: straight lines, dimples and rectangles. The typical size and distance between the laser-textured microobjects lies in the range of 10 ÷ 200 µm, with structure depth from ten nanometers to hundreds of micrometers.

Application of ultrashort laser pulses for LST allows minimalization of the heat affected zone in the laser surface processing. The physical processes activated under ultrashort laser pulses can be predicted by a two-temperature physical model. The interaction of the ultrashort laser pulses with metals is described as stage-by-stage evolution of the surface ablation. At low fluencies, ultrashort laser pulses are able to remelt thin surface layers in the pre-ablation regime: fast homogeneous melting ($F \approx 100 \div 170$ mJ/cm^2) and slower heterogeneous melting ($F \approx 170 \div 200$ mJ/cm^2). For the fluencies higher than 200 mJ/cm^2, the ablation will occur in 20 ÷ 100 picoseconds after laser excitation, due to the time of energy transfer from electrons to lattice ions. A shorter time of laser material explosion can be achieved at intensities higher than $\geq 10^{13} – 10^{14}$ W/cm^2 ($F \geq$ 1 J/cm^2 in a femtosecond laser pulse). The extremely high intensity of laser pulses leads to electrostatic laser ablation or even Coulomb material explosion. Higher intensities lead to activation of the nonlinear processes which can be undesired for high-precision laser surface processing.

The laser pulse overlapping at a high repetition rate of the laser source is different from single-pulse laser surface ablation. The coupling between successive laser pulses may have a positive effect with a decrease of the ablation threshold due to ablated materials' dynamic and incubation effects. Heat accumulation is another phenomenon which is characteristic for laser surface processing with high repetition rate lasers. The heat accumulation has two opposite effects. With non-controlled increasing of the laser-processed surface temperature, the undesired high heat accumulation appears and it leads to surface degradation, oxidation in the air atmosphere and pileup of the melted material. But a fine adjustment of the scanning speed with repetition rate and pulse energy leads to achieving an optimal thermo-physical state of laser pulse interaction with the processed surface. The positive effect of optimal heat accumulation may lead to increasing the ablation efficiency by 80%. Similar to this, the optimal overlapping of laser pulses 50÷75% leads to an increase the laser surface processing quality with low roughness of the output surface.

There are several indirect methods for detection of heat accumulation in laser surface processing – surface roughness measurements, oxidation level detection or laser-processed crater analysis. The direct detection of heat accumulation may be performed with fast PIN photodiodes. An experimental setup with two PIN Si photodiodes gives the possibility to detect temperature changes with time resolution close to 2 ns. The time-resolved measurement of heat accumulation was already used for determination of an optimal regime of laser surface marking of stainless steel.

The quality of the laser-processed surface depends not only on correct choice of laser pulse parameters, like duration, intensity and fluence, but also on a successful scanning strategy. A successful scanning strategy is able to increase the efficiency more than two times at the same parameters of the laser source. The quality of the output surface also depends on the selected scanning strategy. The correct filling strategy may have a 3÷4 times lesser roughness of the laser-processed surface in comparison with other classic filling methods.

At the present time, several groups work on optimization of laser surface scanning strategies for overcoming heat accumulation and for high quality laser surface processing. The interlaced method of laser beam scanning paths arrangement has shown good results in laser surface processing. Decreasing the negative heat accumulation with the interlaced laser scanning strategy leads to an increase in the ablation rate by several times. Application of the interlaced laser beam method with a high-speed polygon scanner achieves a high quality of laser-processed surface. Unlike the interlaced method, the classic hatching method leads to cavity formation on the output surface due to heat accumulation at a high repetition rate of laser pulses. As was mentioned, the interlaced method will demand high scanning speeds of several 100 m/s and laser repetition rates up to tens of MHz. In that case, controllable switching of laser pulses will become a very tough issue.

3. The aim of the Ph.D. dissertation

The dissertation is focused on the characterization of thermo-physical processes in ultrashort pulse laser surface texturing (LST) and the development of laser scanning methods for high-speed processing with high precision and low heat accumulation.

The main tasks of the research presented are:

1) Proposal of new scanning strategies for a high-speed LST method based on inertial laser scanners.
2) Implementation of the LST method with a picosecond laser and galvanometer scanner.
3) Elaboration of evaluation methods for precision of LST and induced heat accumulation.
4) Evaluation of heat accumulation and ablated plasma glow processes during LST by IR radiation measurements and comparison with theoretical predictions.
5) Evaluation of precision, processing rate and thermo-physical processes in the different LST methods.
6) Application of the developed LST method for preparation of functional surfaces.

4. Methodology and materials

4.1. Laser equipment

For the LST experiments, a PX25-2-G solid-state ultrashort laser with InnoSlab technology (EdgeWave GmbH) was used. This laser has wavelength 532 nm, pulse duration 10 ps, average power $P = 13.8$ W, maximum pulse energy 128 µJ and beam quality M2 <1.1 with horizontal polarization vector in the abscissa direction. The frequency of the laser generator applied in the experiment was in the range 140 kHz ÷ 1.2 MHz and the pulse energy used was 10 ÷ 100 µJ. A full laser data sheet can be found in [272]. Scanning of the laser beam was provided by an intelliSCAN III 14 galvanometer scanhead (SCANLAB GmbH) [273] with laserDESK software (version 1.4). Laser beam focusing was provided by an F-Theta objective with 255 mm focal length. This combination gives a maximal laser beam scanning speed equal to 8 m/s. The scanning surface positioning in the focal plane was provided by z-positioning high-resolution vertical translation stage (resolution 0.8 nm) MLJ150/M from Thorlabs. The surface machining setup with ultrashort pulsed laser and galvanometer scanner is presented in Fig. 4.1.1.

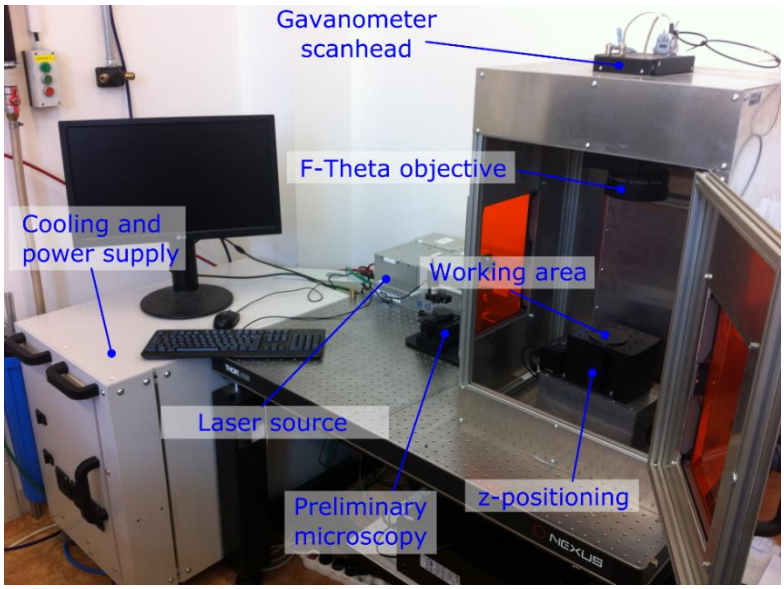

Fig. 4.1.1 Laser surface micro-processing station with galvanometer scanhead.

4.2. Methods of laser surface texturing

Thermo-physical processes were studied in two strategies of laser beam surface scanning: one-dimensional linear scanning and two-dimensional LST with formation of circular microobjects (dimples). The linear surface-scanning was applied for detection of heat accumulation regimes and determination of speed limitations of laser scanning beam treatment.

Another two-dimensional surface texturing (lateral) was performed in the form of a dimple array. The equidistant dimples on a laser-scanned surface is the simplest method of two-dimensional LST with laser formation of microobjects. The precision of microobject's planar

geometry and their depth profile depends on the successful choice of the applied scanning method. In this work, four scanning methods of lateral LST were analyzed: classic scale, classic hatch, shifted path filling and shifted burst. The last two LST methods – shifted path filling and shifted burst – were specially developed in this study for high-speed laser surface processing. The detailed description of all the applied methods of LST are presented in the next paragraphs.

4.2.1. One-dimensional laser surface scanning strategy

The one-dimensional laser surface scanning strategy was performed with a linear raster. The linear raster is the basic strategy of scanning laser surface treatment. The simplest raster with straight lines is presented in Fig. 4.2.1. Only one scanned line from the raster was in use for IR radiation signals detection after adjustment of the scanning and measurement systems. The distance between laser spots depends on applied laser frequency and scanning speed. For example, at a fixed frequency and low scanning speed the laser spots are overlapped (Fig. 4.2.1, *a*). Increasing the scanning speed ten times with the same laser frequency leads to a ten-fold increase in the distance between laser spots, and overlapping between them disappears (Fig. 4.2.1, *b*).

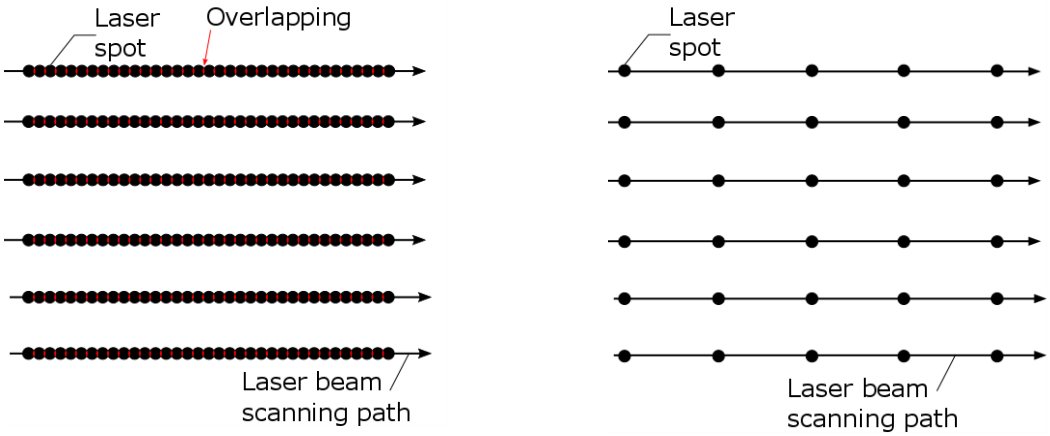

Fig.4.2.1 Linear raster formation with different scanning speeds: *a* – linear raster with low scanning speed and the laser spot overlapping; *b* – linear raster with high scanning speed and distant laser spots.

4.2.2. Classic two-dimensional LST methods

Two-dimensional LST was done by two different classic methods of microobjects (dimples) filling: classic path filling and classic hatch. The in this section the principal features of the both classic LST methods will be discussed.

The first classic-path filling method of a dimple array formation is similar to helical scanning with several concentric circles (Fig. 4.2.2, *a*). The dimple texturing is performed consecutively, as every next dimple in the array is formed only after all the filling paths inside

the previous dimple have been completely finished. The short length of the laser beam paths inside every microobject can increase the interline heat accumulation in addition to the inline heat accumulation.

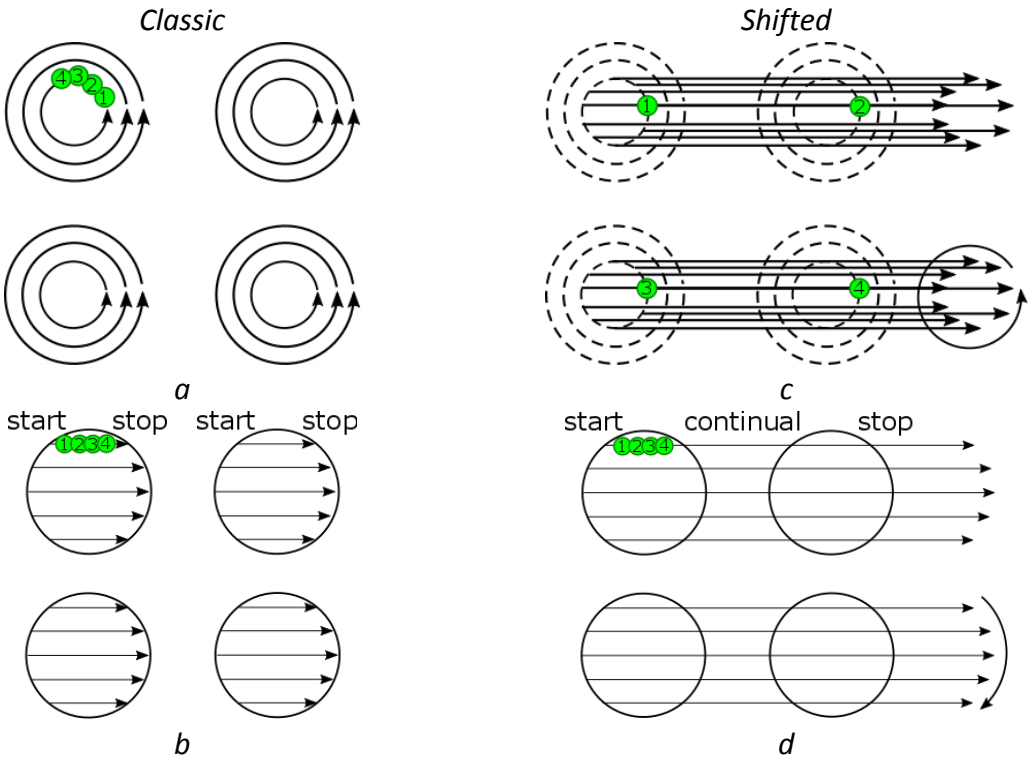

Fig. 4.2.2 Laser pulse distribution for different scanning strategies for laser writing of microobjects: *a* – classic path filling; *b* – classic hatch; *c* – shifted path filling; *d* – shifted burst.

The second classic method is hatch scanning of microobjects in an LST array. The dimples on the textured surface are formed by straight scanning of the laser beam through all the microobjects in one row (Fig. 4.2.2, *b*). This means that one hatching line belongs to the several dimples in the scanned LST array in one horizontal direction. The next hatching line is started only after fully finishing the writing of the previous hatching line in a row. Inline laser pulse generation should be stopped after writing one hatching segment and again started on the next dimple hatching segment.

The classic methods of LST described in the previous paragraphs have several disadvantages. In both these methods, the processing rate v_{pr} is a slowdown of LST speed by "on-fly" synchronization between mirrors' position and laser pulse generation. In the case of the classic path filling method, the inertia of the galvanometer mirrors becomes an additional limitation of scanning speed [274]. Application of the classic LST methods with high repetition rate lasers is additionally limited by physical effects, such as heat accumulation, plasma shielding effects and non-effective short laser spots distance. Moreover, there are some technical limitations of the application of the classic LST methods at high scanning speed: low

precision and a large amount of data needed to be processed in a short time [221], [235], [274].

4.2.3. Developed two-dimensional shifted LST methods

The classic methods' limitations can be overcome by using a non-synchronized surface scanning method. This method, called shifted Laser Surface Texturing (sLST) was developed for fast laser writing of array microobjects with continual movement of the scanner mirrors [275]. The shifted scanning method should help to overcome the physical and technical limitations of the LST by specific ordering of the laser beam paths and inactivation of the on-fly synchronization of the scanner.

The algorithm of the sLST can be explained in detail on an example with an LST array of triangles. Scanning is done on straight lines and laser pulsing has a continuous character during processing of the whole scanning line. In this approach, the laser pulses are rapidly rasterized on the whole processed surface by applying only one laser spot per one microobject in the array (Fig. 4.2.3, *a*). The scanning raster is slightly shifted on the surface at every next application of the raster (Fig. 4.2.3, *b*). The sequence of shifts along a triangular shape produce an array of triangular microobjects (Fig. 4.2.3, *c*).

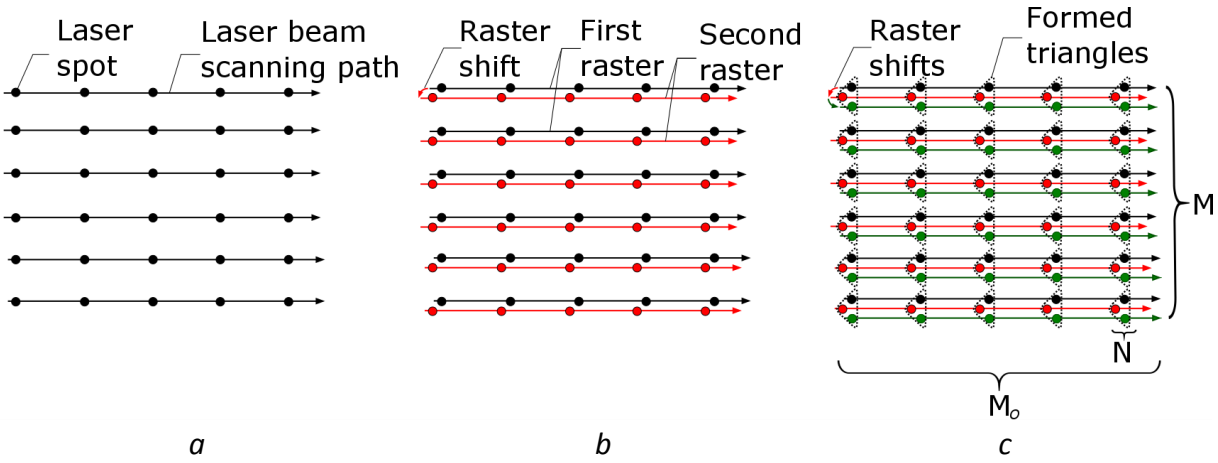

Fig. 4.2.3. The shifted LST method of triangle array formation: *a* – linear raster with one shot per one microobject location; *b* – one small shift of the linear raster to the next position; *c* – formation of triangular objects in an array by two sequenced raster shifts.

The presented shifted LST can be applied for writing different arrays of small objects (dimples, cylinders, cones, donuts, micro-cubes, etc.) on a surface or inside of a material. "Writing" refers to any process induced by a laser which produces a material change, e.g. engraving, marking, recrystallization, melting, foaming, or film removal. The whole array of objects is produced by repeated linear raster laser processing with sequential shifting of the

linear raster between each repetition of the scanning process. Each object in the array is formed by a sequence of laser spots – one spot during each raster repetition. One laser spot contains one laser shot (one-shot mode, Fig. 4.2.2, *c* and Fig. 4.2.3) or several shots per one spot (burst regime, Fig. 4.2.2, *d*). The distance between spots in the line of the raster is defined by the speed of laser beam scanning and by the period between the laser pulses (usually defined by the pulse repetition frequency). The overlapping of the spots inside of the objects is defined by a shifting vector value of the linear raster replacements. There is not a direct determination of the location for every object in the whole array, but the form of objects, distance between spots in the objects and delays between shots are defined by the sequence of shifts between linear rasters. The depth of objects drilled in the shifted LST is generally controlled by repetition of the whole sequence of shifts between linear rasters. For an array of objects with a simple depth structure, the sequence of shifts of the linear raster is the same in all repetitions. For an array of objects with a complex structure or a combination of objects inside the array, the sequence of shifts and rasters is different – in dependence on the target structure and depth profile of the objects.

The data value needed for processing the task is significantly reduced by the shifted method. The amount of data for the shifted method N_{sh} is given by x and y positions of the start and end of M lines ($2 \cdot 2 \cdot M$) multiplied by N rasters on shifted positions (N corresponds to the number of spots in an object) (Fig. 4.2.3, *c*):

$$N_{sh} = 4M \cdot N. \tag{4.1}$$

It is not necessary to know exactly the position of every object in the array and not necessary to know the number of the microobjects in a row M_o. The amount of data for a classic methods N_{cl} is given by the number of rows M multiplied by the number of x and y coordinates of the objects in one row M_o and x and y positions of N spots:

$$N_{cl} = M \cdot 2M_o \cdot 2N. \tag{4.2}$$

As a result, the shifted method needs M_o times less data than classic methods and it can be more than two orders of magnitude less. In practice, the classic method does not have direct control of the position of every laser spot. The amount of data remains in the order of M_o for microobject array formation, because there is a need to know the coordinates of all the filling segments. For example, a textured area of 10 cm^2 with 25 objects per mm^2 and 50 spots per one object with the path filling classic method needs more than six times the amount of data transfer in comparison with shifted LST.

The equidistant position of the equal objects in LST allows the application of indirect control for the laser object formation at the highest speed of the scanning system. In this way, the laser beam scanning is achieved by continual movement of the scanning mirrors without interruption of laser pulse generation at a constant repetition frequency. The emission of required laser pulses is provided by a fast shutter asynchronously with the inline mirror position (Fig.4.2.4). The shutter is based on a Pockel Cell with switching speed on the order of 50 ns and frequency up to 100 kHz [276]. Such a high-switching speed of the shutter forms strongly defined ends of the segments with laser spots on the processed surface. For

commonly used precise galvanometer scanners with a scanning speed of 8 m/s, the tolerance in the length of the segments will be around 0.1 µm.

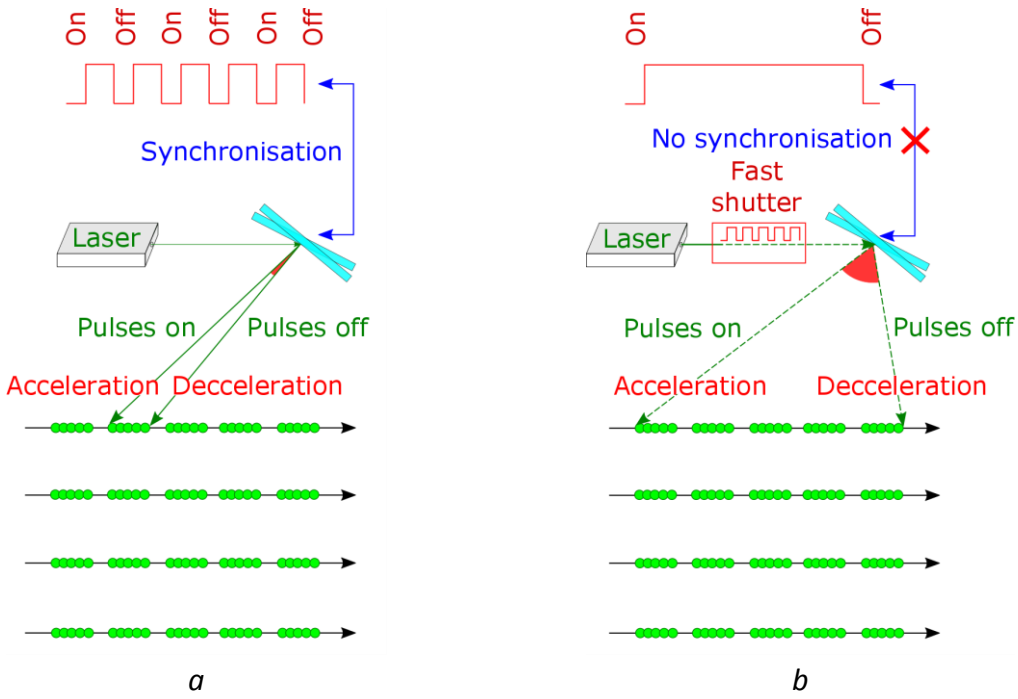

a *b*

Fig. 4.2.4. Equidistant straight segments formed by: *a* – classic hatch strategy. It is necessary to control the mirror position and laser switching for every object in the array; *b* – shifted LST in burst regime. No need to know the position of every object. Synchronization between laser and mirrors is provided only at the start and finish positions on the scanning field.

Unlike in the pulse on demand solution (PoD), in the solution presented here the shutter works asynchronously with the laser generator and mirrors' positions. This means that the position, length and distance between passed segments with laser spots is controlled entirely by the switching of the shutter. No laser pulse will be applied on the scanned surface in the areas which correspond to the closed state of the shutter. The laser pulses will be only inside the allowed segments. For laser pulse generation in the MHz range, the laser pulses inside the scanned segments can have a microsecond delay. This means that the maximal jitter length for the galvanometer scanner with maximal scanning speed 8 m/s can reach up to 8 µm. But the mean value of the laser pulse deviation in scanned segments' ends will be near 4 µm. Such a limitation indicates a technical deviation of the segments length for an LST strategy.

The application of the shifted scanning method may lead to overcoming the physical limitations mentioned before. The heat accumulation effect should regress, because overlapped spots are applied with a time interval equal to one scanning process. The plasma shielding effect decreases, because each two laser spots in a sequence are applied on distant positions on the surface. There is no need for additional computational resources, because

there is not a direct determination of each object in the array. And finally, precision at high scanning speeds is possible because no acceleration/deceleration is necessary and the laser pulse generation works in a stable manner on one of its internal frequencies. The method was submitted in a patent application [274], [277].

4.3. Experiments of laser surface scanning

The combination of laser pulse energy, generation frequency and beam scanning speed is responsible for the level of heat accumulation on a scanned surface. In this study, the three parameters of laser beam surface scanning were changed: time interval between laser pulses, energy of laser pulses and scanning speed.

The time interval between laser pulses was changed by setting the frequency or by involving a switching trigger in the optical path of the laser beam. The switching trigger was built on the Pockels effect with fast rise times (about 50 ns). The energy of the laser pulses depends on the frequency of the main laser pulse generator and only three pulse energy levels were applied: 10 μJ, 30 μJ, 100 μJ. The scanning speed was regulated by electric current in the galvanometer motors, which were driven by control card RTC5. The same card was used for control of the laser generation parameters and external trigger switching.

4.3.1. Parameters of the one-dimensional laser surface scanning strategy

At the low scanning speed speeds and high frequency of laser pulses, the spot distance is at the nanometer scale. The big laser spot overlapping can initiate high heat accumulation and material degradation. When the speed of the laser scanning is high enough and the laser has low frequency, then the laser spot distance on the scanning line becomes more than 57 micrometers and this is twice as wide as the applied laser spot size. Heat accumulation disappears, because the laser spots have not overlapped. All the applied scanning speeds, frequencies and energies in the laser pulses for the straight lines laser scanning experiments are presented in Table 4.1.

Table 4.1. Scanning parameters and laser spot distances for three different frequencies of laser pulse generation.

Speed v_{sc} (m/s)	0.007; 0.03; 0.07; 0.15; 0.3; 0.7; 1; 2; 3; 4; 5; 6; 7; 8
Energy Q_p (μJ)	10; 30; 100

Frequency f_{pulse} (kHz)	Laser spots distance r_d (μm)
1176 (for 10 μJ)	0.006; 0.03; 0.06; 0.1; 0.3; 0.6; 0.9; 1.7; 2.6; 3.4; 4.3; 5.1; 6.0; 6.8
454 (for 30 μJ)	0.02; 0.1; 0.2; 0.3; 0.7; 1.5; 2.2; 4.4; 6.6; 8.8; 11.0; 13.2; 15.4; 17.6
140 (for 100 μJ)	0.1; 0.2; 0.5; 1.1; 2.1; 5.0; 7.1; 14.3; 21.4; 28.6; 35.7; 42.9; 50.0; 57.1

For the laser beam surface scanning, the heat accumulation depends on the linear energy density arriving on the material surface. The line energy is defined as the total laser pulse energy applied per length unit on the scanned surface:

$$Q_l = P/v_{sc}, \tag{4.3}$$

where P defines the average power of the applied laser pulses and v_{sc} is the laser beam scanning speed.

4.3.2. Parameters of two-dimensional laser surface scanning strategies

The dimples' size used was equal to 80 µm, with the periodicity of LST microobjects equal to 200 µm. The chosen geometry has practical sense and it can be used in several applications, like LST of oiled sliding parts or adhesion surface modification [278], [279]. There are five common parameters for the LST methods with dimples applied in this study:

- inline spot overlapping is equal to 7 µm with optical trigger pulse switching;
- scanning paths overlapping is equal to 10 µm;
- the energy in the laser pulse is equal to 10 µJ, 30 µJ and 100 µJ;
- the lateral precision of the LST methods was tested in a wide range of scanning speeds: 0.02, 0.04, 0.05, 0.06, 0.07, 0.15, 0.3, 0.7, 0.08, 0.1, 0.15, 0.2, 0.3, 0.4, 0.5, 0.6, 0.7, 1, 2, 3, 4, 5, 6, 7, 8;
- the laser-textured array has a rectangular form with 10 mm length in the laser beam scanned direction and 2 mm height.

The classic path filling LST and shifted path LST methods were applied with three circles with increasing diameters: 20 µm, 40 µm and 60 µm. This corresponded to the distance between scanning round paths equal to 10 µm. The overlapping between laser spots was 7 µm and it was controlled by external trigger frequency in connection with scanning speed. The periodical distribution of 200 µm of the dimples was set directly with the repeat function of the laserDESK software.

In the classic hatch and shifted burst methods, the distance between hatching paths was equal to 10 µm. The inline overlapping of 7 µm in the hatching lines for the classic method was controlled by the external trigger, similar to the classic path filling. The process of the laser pulse generation was driven by the galvanometer control board with correction between mirrors' position and laser pulse generation for every microobject in the LST array.

Another series of experiments was done without the application of an external trigger for the classic LST methods. The overlapping of the laser spots was directly dependent on the applied scanning speed and frequency. The combination of these two parameters gives the distance between laser spots, similar to the one-dimensional laser surface processing (Table 4.1).

Every LST experiment was performed minimally five times for statistical evaluation of the results. The wide rectangular scanning area of 2.4 × 170 mm^2 and multiple repetition of the scanning process were applied for processing rate evaluation of the different LST methods.

4.3.3. Laser control software for application of sLST methods

The classic methods of LST are possible to implement with standard available laser driving software, like LaserDesk or Scaps. The new shifted methods of LST have not been implemented yet in the standard functions of the software for programming of a galvanometer or polygon scanning head. The application of the shifted methods was done with specially developed software LaserControl (Fig. 4.3.1, *a*). The main principle of the sLST was applied in the algorithm of the LaserControl software for decreasing data transfer between the galvanometer scanner and laser source. The scanned area is represented by one wide scanning rectangle without a full description of every microobject in the laser-textured array. Only global parameters are in use, like scanning speed, number of rows and laser pulse frequency. In contrast, the classic methods need to represent every scanned microobject directly (Fig. 4.3.1, *b*) and this leads to an increase of LST processing time (compare Eq. 4.1 for sLST with Eq. 4.2 for the classic LST).

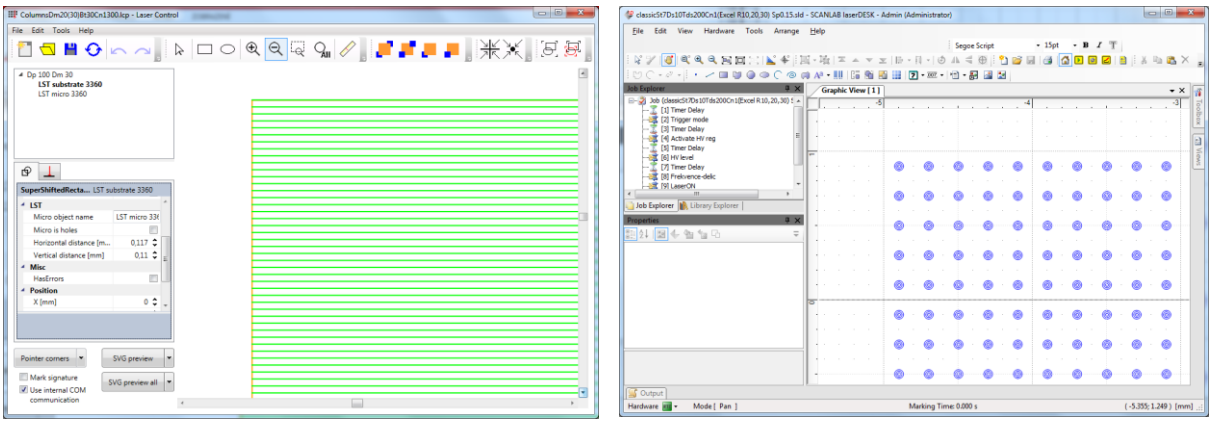

a *B*

Fig. 4.3.1. Software interface for providing LST with a galvanometer scanner: *a* – LaserControl (the texturing array in the sLST method is described as one raster); *b* – LaserDesk (every microobject in the array is described with detailed path scaling parameters).

The LaserControl software has several special functions for providing shifted path filling LST, shifted burst LST and their variations. One of the most original functions is formation of inverse structures – concave dimples or protruding columns. Another uncommon function is the gradient and formation of the microobject array by monotonically increasing the distance between them. The gradient textures are useful for the optimization of the LST process for achieving the desired functional properties of the laser-textured surface.

4.4. Materials

The experiments presented in this thesis were conducted on stainless steel metal sheet X5CrNi18-10 (1.4301, AISI 304) with 1 mm thickness. The samples were factory polished with protective foil and cut in a rectangular form with size 50x15 mm^2. The chemical composition of the stainless steel is: Fe(base), 0.03% C, 0.3% Si, 1.2% Mn, 17.2% Cr, 9.3% Ni, 0.2% Mo

[280]. The physical properties of the steel are presented in Table 4.2. The temperature hanges in the physical properties of the AISI 304 stainless steel are presented in Appendix B.

Table 4.2. Physical properties of stainless steel AISI 304.

Properties	Value	Source
Absorption (A, 527 ÷ 532 nm)	40%	[281]
Roughness (R_a)	0.01÷0.02 μm	Initial
Thermal conductivity (k)	14.92 W/(m·K)	[282]
Specific heat (c_p)	0.477 kJ/kg·K	[14], [283]
Density (ρ)	7.90 g/cm^3	[284]
Thermal diffusivity ($\alpha_{th} = k \cdot \rho^{-1} \cdot c_p^{-1}$)	4·10^{-6} m^2/s	[285]
Melting range (T_m)	1.399 – 1.421 (°C)	[284]
Evaporation temperature (T_v)	3000 (°C)	[14], [286]
Tensile strength (σ in range 21 ÷ 815 °C)	620-160 (MPa)	[284]
Ablation threshold (F_{th} for 532 nm)	0.5 J/cm^2	[186]

In experiments with evaluation of the LST method's precision, the stainless steel samples were covered by high-emissivity LabIR® paint (Fig. 4.4.1) [287]. The first series of samples were painted all together at once to ensure equal paint thickness. The thickness of the paint was 8 ÷ 10 μm. The pulse energy corresponds to a paint removal spot with a diameter equal to 20 μm (effective spot size). The second series of samples were used without LabIR® paint for LST on a polished surface ($R_a = 0.01 \div 0.02$ μm). These clear samples (without paint) were used for experiments for evaluation of the volumetric precision and efficiency of different methods of LST.

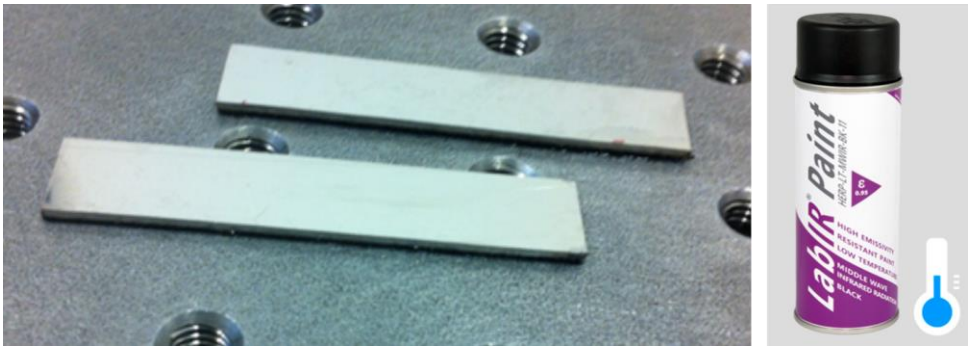

a *b*

Fig.4.4.1. Preparation of a surface for detection of the precision of a laser-scanning strategy: *a* – source stainless steel samples; *b* – low-temperature high-emissivity LabIR® paint [287].

Several other materials have been used fin these experiments or different practical applications of LST: nickel-based superalloy AM1, aluminium oxide, silicon carbide, aluminium

alloys and steel molding forms, titanium and tungsten, glasses, etc. Several types of the surface texturing already were used in real-world applications.

4.5. Surface geometry analysis

The LST surfaces were analyzed using different methods of microscopy and profilometry. The measured data was statistically processed using different mathematical methods and software equipment. In the next sections, the methods of data processing and the evaluation of results are presented. The statistical data were processed with a MATLAB® processor and profiles of the LST were analyzed with MountainsMap® software (ISO 4287). There are several supporting programs were created for data conversion and preprocessing.

4.5.1. Microscopy and profilometry measurements

The first examination of laser-textured surfaces was performed with digital microscopy Dino-Lite AM4515T8 (700 – 900x). The contrast imaging and optical profilometry were performed with 3D microscope HIROX KH-7700. Black and white high contrast images from LabIR®-coated steel samples were taken at a long exposure time regime (1 ms, Fig. 4.5.1, *a*). The contrast images were collected from three different areas (left-edge, center and right-edge) with 12 ÷ 17 microobjects in an area.

The primary depth profiles analysis of laser-textured surfaces was done using a multifocal algorithm with the 3D HIROX optical microscope. The detailed analyses of the laser-textured surface relief were done using a contact surface profiler, KLA-Tencor P-6 Profiler. The laser surface processed textures were measured in parallel lines with a length of 400 µm and a separation distance of 8 µm. The profiler tip angle was 60°, its radius 2 µm, used load 1 mg and speed 50 µm/s. Texture depth measurements were taken from three areas (left-edge, center and right-edge) with four scanned microobjects (Fig. 4.5.1, *b*).

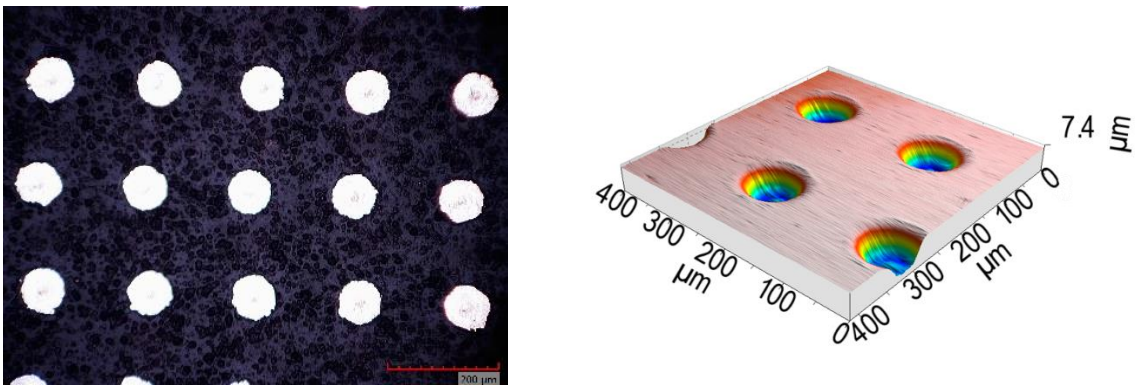

a *b*

Fig. 4.5.1. The LST analysis: *a* – high contrast long exposure time microscopy; *b* – 3D profilometry of laser-textured area with 4x microobjects.

Surface structure and chemical analyses of the laser processed surfaces were studied with SEM FEI Quanta 200 with an EDS (Energy Dispersive Spectrometer). Subsurface structure of the LST on the stainless steel samples was provided by high resolution SEM (JSM 7600F from JOEL). This SEM has maximal magnification up to 1,000,000× and it was used for analysis of the bottom structure of the laser-textured microobjects.

4.5.2. Evaluation methods of LST microobjects diameter deviation

The different scanning strategies of LST were applied on the LabIR® paint-surface covered samples with subsequent surface microscopy with constant exposure time of 1 ms. The contrast image of the lateral LST was used for determination of the microobjects' geometry on the processed surface with a morphological reconstruction [288]. A similar contrast method was applied for the entrance diameter of the laser-drilled microobjects used by M. Ghoreishi et al. [289]. The three textured areas were analyzed for statistical processing of the LST precision. The principal scheme of the evaluation of the LST precision can be described as a logical chain with six steps (Fig. 4.5.2).

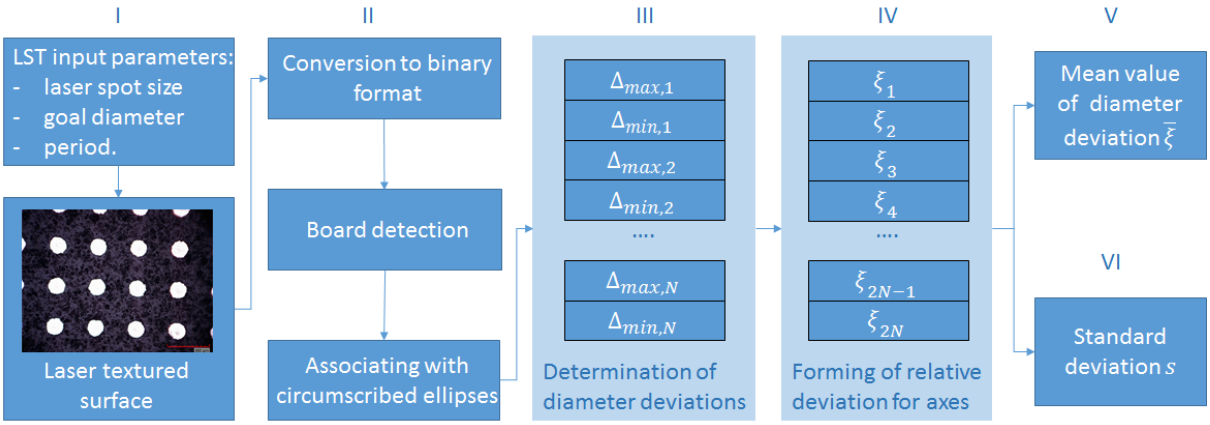

Fig. 4.5.2. Block scheme of the evaluation of the LST precision with binary conversion.

I. In the very first step, the galvanometer scanhead was programmed for providing LST based on effective laser spot diameter 20 µm and goal diameter Δ_g of the textured microobjects 80 µm with periodicity equal to 200 µm (Fig. 4.5.2, step I).

II. In the next step, the microscopy images of the laser-textured surfaces were converted to binary format (Fig. 4.5.2, step II). The obtained binary arrays were inspected by a morphological reconstruction algorithm [288], [290]. The detected boards were associated with circumscribed ellipses with corresponding major and minor axes (Fig. 4.5.3). The following evaluation of the LST precision is defined as the value of the axes length deviation from the goal size, and it was done in the next four steps.

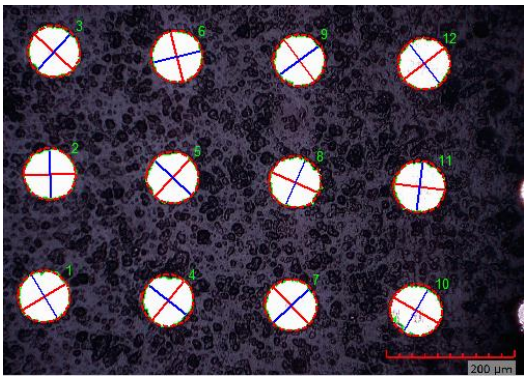

Fig. 4.5.3. Laser-textured surface and board detection with major (red line) and minor (blue line) axes. The analysis was provided only for fully detected microobjects (red dotted ellipses).

III. The maximal and minimal diameter deviations were calculated as the difference of the major and minor axes from goal diameter value Δ_g:

$$\Delta_{max,i} = \left|\Delta_g - \Delta_{major,i}\right|, \Delta_{min,i} = \left|\Delta_g - \Delta_{minor,i}\right|, \quad (4.4)$$

where $\Delta_{major,i}$ – length of major axis of laser-textured microobject, $\Delta_{minor,i}$ – length of minor axis of laser-textured microobject, $\Delta_{max,i}$ – object diameter deviation from major axis length, $\Delta_{min,i}$ – object diameter deviation from minor axis length.

IV. Defining the relative deviation ξ from goal diameter for all N objects. Two values of relative deviation from one object are defined:

$$\begin{aligned} \xi_1 &= \Delta_{max,i}/\Delta_g\,; \\ \xi_2 &= \Delta_{min,i}/\Delta_g\,; \\ &\cdots \\ \xi_{2N} &= \Delta_{min,N}/\Delta_{g.} \end{aligned} \quad (4.5)$$

V. Defining the mean value of the relative deviation $\overline{\xi}$ through all measurements for one speed:

$$\overline{\xi} = (\xi_1 + \xi_2 + \cdots + \xi_{2N})/2N. \quad (4.6)$$

VI. Defining the standard deviation for selected scanning speed:

$$s = \left(\frac{1}{2N-1}\sum_{i=1}^{2N}(\xi_i - \overline{\xi})^2\right)^{1/2}. \quad (4.7)$$

The processed results give the possibility to estimate the speed limits of the tested LST methods, to observe the influence of speed on the precision of LST and to predict speed efficiency for the different LST methods.

4.5.3. Depth profile analysis of LST microobjects

There are several factors that have an influence on the tapper angle and the depth of the laser-formed surface dimples [291]. The shape profile analysis gives information about the efficiency and accuracy of the volumetric material ablation in LST [185]. In this study, the depth profile of the laser-textured microobjects was analyzed by comparative evaluation of the cross-section area. Similar to lateral LST evaluation, the depth profiles for 500 textured

microobjects array (2×10 mm^2) were analyzed. The main difference of the depth profile evaluation is in laser processing of a non-painted steel surface. The profiler lines were scanned perpendicular to the laser scanning direction. A 3D surface profile was reconstructed from the linear profiles (MountainsMap Imaging Topography software). The linear depth profile of each dimple was obtained from the 3D profile by placing the line at a 45° inclination (diagonal). This inclination was used to include data and errors from both laser scanning and profiler scanning. The accuracy of the LST depth profiles was evaluated in comparison with the goal profile area. The goal profile had a diameter of 80 µm at the surface and the goal depth of the laser-textured microobjects was taken as 6.5 µm. A similar texture depth was performed by LST on several types of functional surfaces [71], [108], [292]–[294]. The shallow depth of the dimples corresponds to a tapper angle of 70° and it is in the range of tapper angles from other experimental works [185], [266], [291]. The comparison method of laser-textured dimple profile accuracy can be presented in a block scheme with six steps, similar to the lateral evaluation (Fig. 4.5.4).

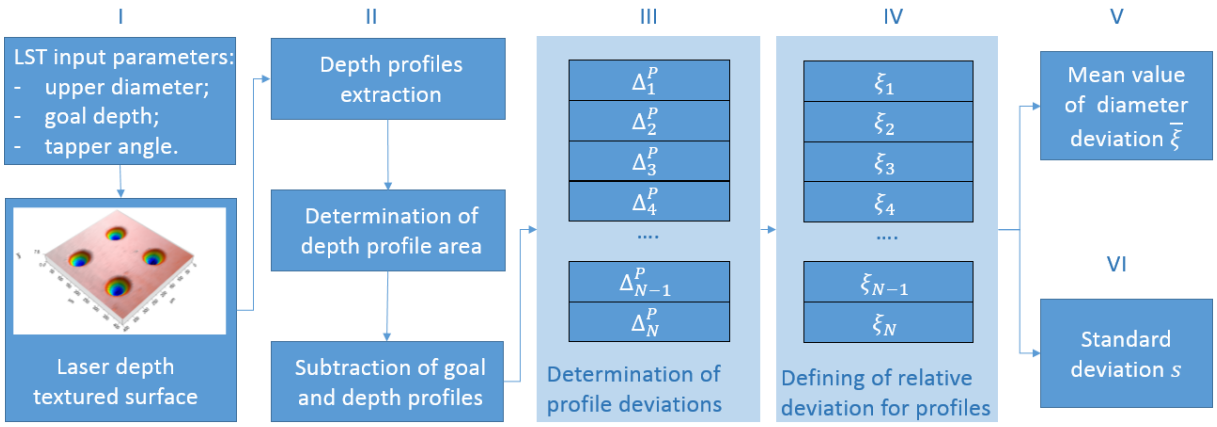

Fig. 4.5.4. Block scheme of the evaluation of the LST accuracy with depth profile subtraction.

I. The first step determines the repetition count of the LST for achieving the goal depth of the texture. The profile depth was considered as achieved when the depth profile of the laser-textured microobjects has minimal deviation from the goal profile. The planar geometry of the LST was kept the same as in the lateral evaluation. The depth profiles were taken from four microobjects from three areas on the textured surface (4 × left side + 4 × central side + 4 × right side).

II. The profiles of microobjects were taken in a 45° direction from the stylus scanning direction. The output profile data were overlayed with the goal profile area (Fig. 4.5.5, *a*). The difference between the measured profile area and the goal profile was defined as vertical semi-trapezoids (Fig. 4.5.5, *b*).

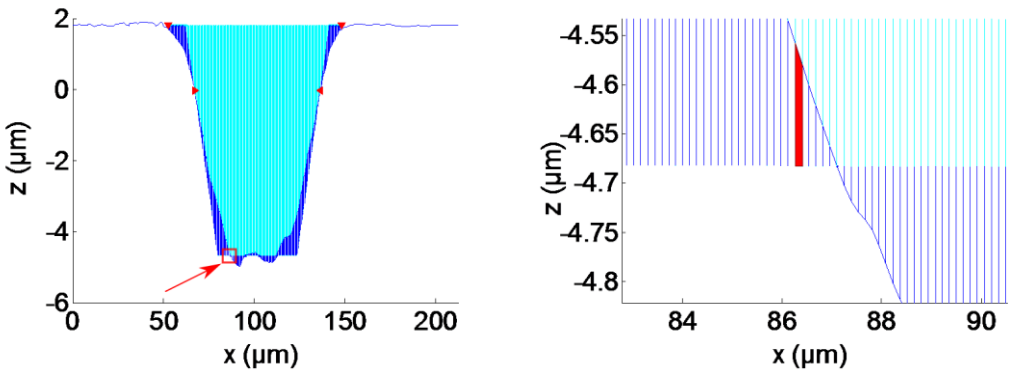

a *b*

Fig. 4.5.5. Evaluation of the LST depth profile accuracy: *a* – depth profile area with overlayed ideal profile form (markers correspond to the entrance diameter and crossed profiles; the arrow shows the zoomed area); *b* – deviation between the measured profile and the goal profile was determined from vertical semi-trapezoids (*b*, one integral trapezoid is marked by red color).

III. The measured profile deviation Δ^P from the goal profile was calculated in integral form:

$$\Delta_k^P = \sum_{i=1}^{N} l \cdot h_i, \tag{4.8}$$

where k – is the order number of profile, i – is the order number of point on the profile line, N – is the full number of points on the profile line, l – is the step value along the horizontal direction on the profilogram and h_i – is the vertical distance between corresponding points on real and goal profiles.

IV. The next step is defining of relative deviation ξ from goal profile Δ_g^P for all N profilometry scanned objects:

$$\begin{aligned} \xi_1 &= \Delta_1^P / \Delta_g^P ; \\ \xi_2 &= \Delta_2^P / \Delta_g^P ; \\ &\dots \\ \xi_N &= \Delta_N^P / \Delta_g^P . \end{aligned} \tag{4.9}$$

Steps V and VI have the same logic as in lateral LST evaluation (Eq. 4.6 and Eq. 4.7, respectively).

The processed results give the possibility to evaluate the depth precision, ablation efficiency and depth processing rate of applied LST methods for repeated laser scanning.

4.6. IR surface radiation detection and analysis

4.6.1. Evaluation methods for induced heat accumulation and plasma glow radiation analysis

The laser-induced temperature changes and ablation plasma glow detections were carried out using an improved measurement scheme, similar to laser marking experiments [228]. There are three parallel detection channels (Fig. 4.6.1) [295]:

1) The low temperature heat accumulation was detected on channel 1 by a variable gap HgCdTe semiconductor photodiode ($\lambda_{opt} = 6$ µm, PVI-3TE-6, VIGO system) with 3-level Peltier cooling and a MIPDC-F-5 control unit (power supply and preamplifier). The optical area of the photodiode is 1×1 mm^2. The photodiode was used together with a Ge filter (2 ÷ 16 µm (IR), 1 mm thick) and the resulting wavelength detection range was 3 ÷ 6 µm. The longer wavelength limit 6 µm corresponds to the spectral maximum of surface IR radiation with temperature 483 K (under Wien's displacement law).
2) The high temperature heat accumulation was detected on channel 2 by Si PIN photodiode S5052 ($\lambda_{opt} = 4.6\ \mu m$, Hamamatsu) with low pass filter FEL0850 (Thorlabs). The effective active area of the photodiode is 7 mm^2. The spectral sensitivity of the S5052 photodiode with the FEL0850 filter is in the range of 0.8 ÷ 1.1 µm (NIR). The longer wavelength limit 1.1 µm corresponds to the spectral maximum of surface IR radiation with temperature 2635 K.
3) The integral signal from reflected laser beam irradiation, plasma glow and IR surface thermal emission from the surface and ablated materials was detected on channel 3 by Si PIN photodiode S5972 (Hamamatsu). The photosensitive area size of the photodiode is 0.5 mm^2. The spectral response range is 0.3 ÷ 1 µm.

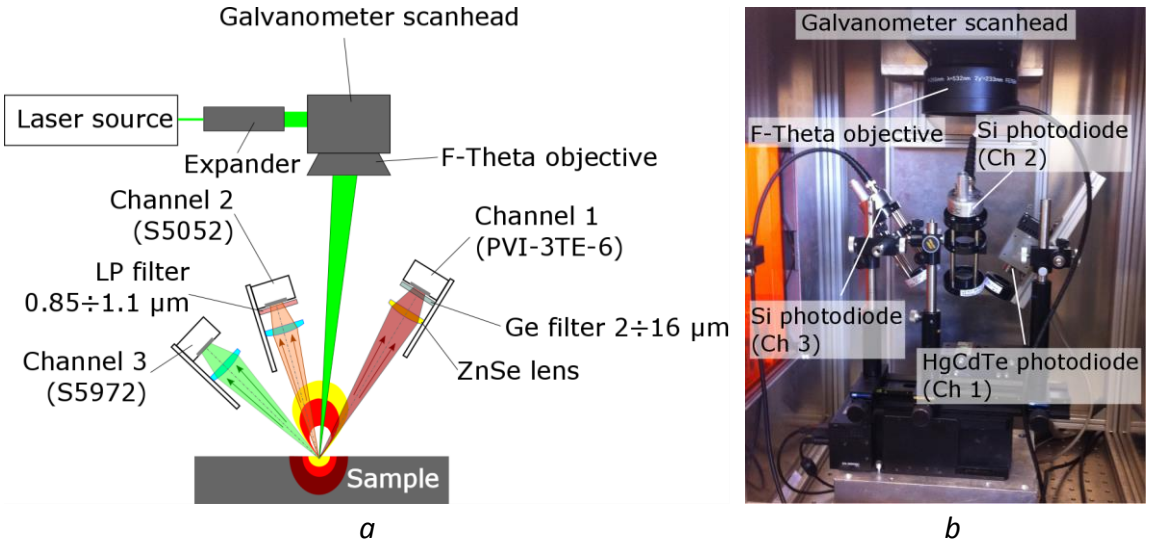

a *b*

Fig. 4.6.1. IR measurement set-up with three IR photodiodes, picosecond laser source and galvanometer scanner: *a* – schematic representation; b – experimental equipment.

The light emission from the laser ablated spot was focused by VIS NIR (350 nm ÷ 2.0 µm) 50 mm focal length lenses on the Si PIN photodiodes and by a ZnSe (0.55 ÷ 18 µm) 25.4 mm focal length lens with a Ge filter on the HgCdTe photodiode (VIGO). The PIN photodiodes are operated with voltage 12 V in reverse bias mode (Fig. 4.6.2). The signals from the IR diodes were recorded by a 1 GHz bandwidth oscilloscope (WavePro 950, Teledyne LeCroy) with a 16 GS/s maximal frame rate. All detectors were directed on a fixed surface point with a detection area near 1 mm^2. The distance between the detectors' lenses and the surface was

near 100 mm, with a 50 degree angle between the scanned surface and the axis of the diodes' optical line-up. The scanning speed in the heat accumulation detection experiments was in the range of 0.007 ÷ 8 m/s (see Table 4.1). Three values of laser pulse energy, 10 – 30 – 100 μJ, were applied for every scanning speed value (all together 36 speed/energy combinations).

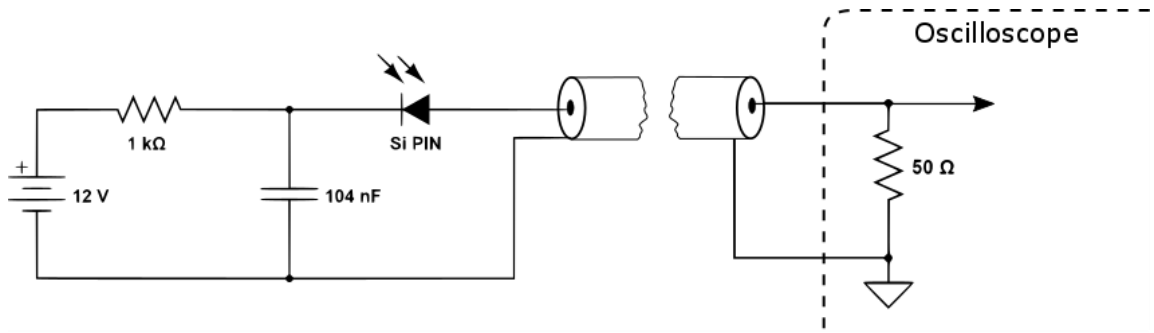

Fig. 4.6.2. Scheme of the Si PIN photodiodes' connection to the oscilloscope in reverse bias mode (adapted from [296]).

The reverse bias mode of the PIN photodiode increases the width of the depletion junction, producing an increased responsivity with a decrease in junction capacitance, and produces a very linear response. The disadvantage of operating under reverse conditions does tend to produce a larger dark current and noise, but it can be suppressed by the statistical data processing, which is described in the next section.

4.6.2. IR radiation data analysis during laser linear surface scanning

The data of IR emission from a laser-processed surfaces were collected by an oscilloscope with record sampling 0.12÷2 ns. The low temperature irradiation data were registered on the first channel (spectral limit 6 μm), the high temperature on the second channel (spectral limit 1.1 μm) and the integral signal was detected on the third channel (no filter, spectral range 0.3÷1 μm) (Fig. 4.6.1). The triggering of the oscilloscope frame was provided on the third channel, because it has a maximal input signal. The trigger was tuned to a maximum for every change of experimental parameters (scan speed, energy or frequency of the laser). Laser beam movement was controlled by a galvanometer scanner with different mirror speeds with three different values of laser pulse energy (Table 4.1).

Due to the significant value of the dark current and noise signals in reverse bias mode of the photodiodes' connection (Fig. 4.6.2), the subtraction algorithm for the data processing was applied, similar to the "Stamp" method. A full description of the "Stamp" method can be found in the author's article [297]. The application of the statistical "Stamp" method for detection of heat accumulation is described in the next section.

The laser beam passed through the detection area of these three diodes in sequential order and the reaching of the maximal peak is detected in the order of the channels' numbers. The wide recording of the data gives the possibility to determine the relative position of maximal heat accumulation on every channel (step 100 ns, Fig. 4.6.3, *a*). The detailed analysis

of the maximal heat accumulation region was done with a smaller time step in a short recording (step 0.125÷2 ns, Fig. 4.6.3, *b*).

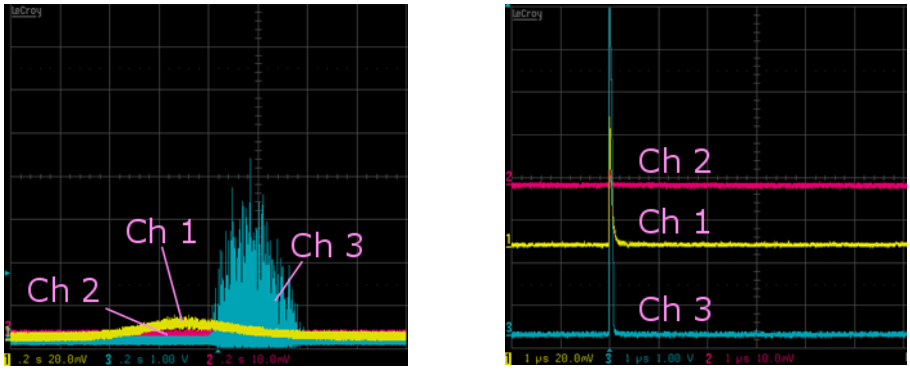

a *b*

Fig. 4.6.3. Oscilloscope experimental frames with signals detected from the three photodiodes: *a* – long recording of the IR response at 7 mm/s scanning speed and laser pulse energy 10 µJ; *b* – short recording of the IR response at 70 mm/s scanning speed and 100 µJ laser pulse energy.

The linear raster was created by laser beam surface scanning along equidistant straight lines. The scanned lines were 5 mm long and the center of the scanned line was matched with the center of the detected area. After centering the scanning on one line, surface scanning was applied with detection of the IR radiation response. The background noise level was defined before heat accumulation IR signal detection as the mean value of the dark voltage:

$$U_b = \frac{1}{N_b}\sum_{i=1}^{N} U_{b,i}, \tag{4.10}$$

where U_b – mean value of the background signal, N_b – number of the recorded values in the sequence without laser influence, $U_{b,i}$ – value of the background signal voltage recorded in the time moment t_i and i – index of the signal value. In the next step, the signals from all three diodes were recorded at the moment when the laser beam scanned on the surface. The signals from all channels were recorded in the 200 ms wide region with the triggered signal in the center (Fig. 4.6.4, *a* (center part)). Detection of the heat accumulation was performed during the 40 µs interval close to the maximal achieved signal. According to the "Stamp" method, the residual heat signal is detected as the mean value from the equidistant signal segments in the closest time intervals to the next coming laser pulse regions (Fig. 4.6.4, *b*):

$$U_r = \frac{1}{R \cdot N_r}\sum_{p=1}^{R}\sum_{i=1}^{N_r} U_{r,i}, \tag{4.11}$$

where U_r – mean value of the residual heat signal, N_r – number of signals which were analyzed in the closest to the next laser pulse segment, R – full number of the analyzed segments, $U_{r,i}$ – value of the residual heat signal recorded in the time moment t_i, p – index of the analyzed segment and i – data index in the signal segment.

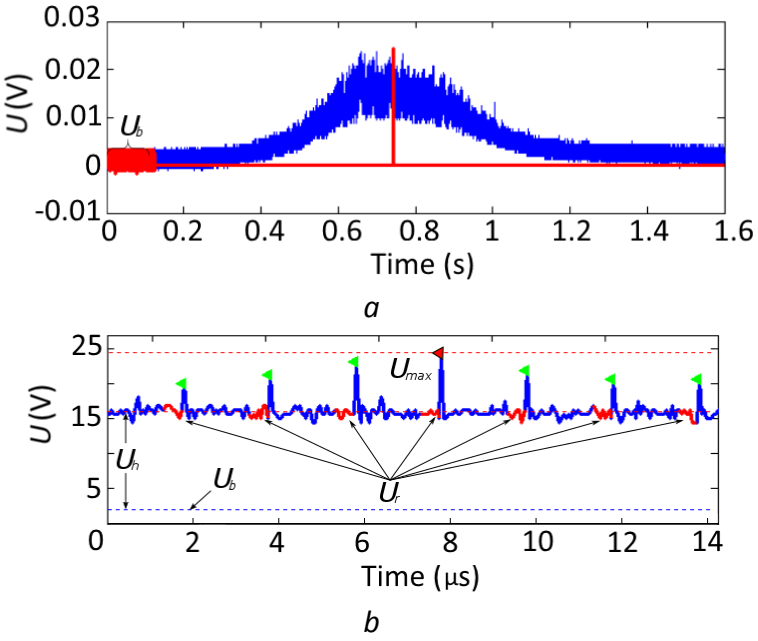

Fig. 4.6.4. Determination of the heat accumulation in the first channel at scanning speed 7 mm/s and laser pulse energy 30 μJ: *a* – determination of the background signal level U_b; *b* – determination of the residual heat signal U_r and maximal peak signal value U_{max}. Heat accumulation U_h is detected as a differential value.

The resulting heat accumulation U_h was defined as the difference between the residual signal and the background signal mean values:

$$U_h = U_r - U_b. \tag{4.12}$$

In a similar way, the maximal value of the signal for all channels U_{mb} was detected as the difference between the absolute maximum in the signal and the background level:

$$U_{mb} = U_{max} - U_b, \tag{4.13}$$

where U_{mb} – value of the relative maximum and U_{max} – absolute maximum value in the signal. The difference between the absolute maximum and residual heat will be indicated as U_{mr}:

$$U_{mr} = U_{max} - U_r. \tag{4.14}$$

The measurements with a short time step are provided in two stages. The data about the background signal level U_b were collected before the laser started to scan the observed area on the surface. After this, the measurement was performed with detection of the residual heat signal U_r during the laser surface scanning. The heat accumulation is again defined as the difference between residual heat U_r and background signal U_b (Eq. 4.12).

The signal from the third channel is integral: mainly it contains the plasma plume glow and partially the IR radiation from the laser spot. The duration of the plasma glow was measured as the distance between two boundaries: arising before the plasma maximal peak signal and decreasing after it, where the value of the signal is 10^2 times lower than the upper limit of the measurements (Fig. 4.6.5). This corresponds to the boundary signal on channel 3 equal to $U_{lim} = 78$ mV.

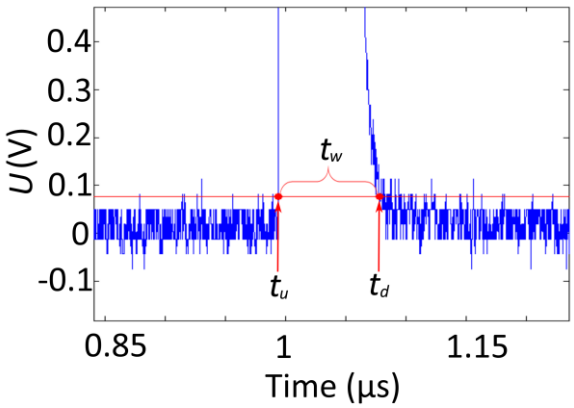

Fig. 4.6.5. Determination of the plasma glow duration for ablation with laser pulse energy 30 μJ and 0.07 m/s scanning speed.

The determination of the plasma glow duration can be described mathematically as the difference between the time of detection limited signal on the downward part and the time of the detection limited signal on the ascending wing:

$$t_w = t_d - t_u, \tag{4.15}$$

where t_w – plasma glow duration over boundary signal 78 mV, t_d – time moment when the plasma glow signal becomes lower than the boundary limitation, t_u – time moment when the plasma glow signal becomes higher than the boundary limitation.

For all channels, the measurements were taken five times. The standard deviation was established in the same way as for precision control experiments (Eq. 4.7). Before every next measurement, a new area of the sample surface was exposed the laser scanning.

4.6.3. IR radiation data analysis during two-dimensional LST

The heat accumulation during laser formation of a dimple array was detected with the same methodology as for straight line scanning. The classic LST strategies were compared with the shifted LST, in the order described in the previous sections 4.3.1 and 4.3.2 (Fig. 4.3.1). The precision limit of the acceptable LST was selected equal to 5% in diameter deviation (Eq. 4.6). The reason for the acceptable precision limit value of 5% can be explained by the technical parameters of the laser scanning system. The applied electronic module based on the Pockels Cell has a real response time in combination with the RTC card of about 0.2 ÷ 0.5 μs. It corresponds to the start-stop jitter length ≤ 4 μm at maximal scanning speed 8 m/s [276], [298]. This technical limitation was detected in experiments with LabIR® paint and it was used for speed selection in the applied LST methods: 0.15 m/s for classic path filling, 8 m/s for path filling sLST, 0.7 m/s for classic hatch and 8 m/s for burst sLST. Similar to the straight line experiments, the heat accumulation for LST with microobject formation is detected as the residual signal mean value before every next laser pulse (Eq. 4.12).

The heat accumulation was detected for two regimes of laser pulse generation. The first regime was applied with the laser pulse delivery controlled via an external trigger with constant overlapping of laser spots. In this regime, the trigger allows only specific pulses,

which in compliance with the distance between laser spots on the scanned surface in an applied LST method 6.8 ÷7 µm. This corresponds to the optimal overlapping of 65% (Fig. 4.2.2). The shifted burst has the fixed 6.8 µm pulsed step at 10 µJ only, due to the increasing in the pulse period at higher pulse energies (Table 4.3). The external trigger gives the possibility to achieve fine control of laser spot overlapping with a time interval between laser shots of 1 µs only, but this regime leads to a dramatic decrease in the output power. The classic scanning strategies have lower output laser power in comparison with the corresponding shifted strategies. The trigger application for the shifted path filling regime has an accentuated feature: the period between laser pulses is about a thousand times longer than in the other methods. The heat accumulation for this method will be minimal even at higher power in contrast to the low frequency classic path filling method.

Table 4.3. Output laser power applied with three laser pulse energies and an external trigger regime of laser spot overlapping control.

Scanning strategy	Scanning speed v_{sc} (m/s)	External trigger frequency f_{trg} (kHz)	Laser pulse period t_{lp} (µs)	Laser power P (W) at 10 µJ	Laser power P (W) at 30 µJ	Laser power P (W) at 100 µJ
Classic path filling	0.15	21	47.6	0.21	0.63	2.1
Shifted path filling	8	40	$17.4 \cdot 10^3$	0.4	1.2	4
Classic hatch	0.7	100	10.0	1.0	3.0	10
Shifted burst	8	40	0.85;2.2;7.14	11.7	13.6	13.8

The second regime of the LST is provided without an external trigger controlling the laser spot overlapping for the classic methods. In this case, all laser pulses are emitted and the laser power is maximal for the applied generator frequency. The classic path filling and hatch strategies have low scanning speeds, and higher heat accumulation can be detected. This regime has a considerably smaller laser spot distance for classic strategies of surface texturing. In shifted strategies, the external trigger remains in use, because it is needed for the microobjects' inline distribution distance control (see Fig. 4.3.1, *c*, *d* and Fig. 4.3.3, *b*). For the laser generation frequency 1.17 MHz (pulse energy 10 µJ), the spot distance is minimal and it is only about 0.13 µm for the classic path filling strategy and 0.6 µm for the classic hatch strategy (Table 4.4). For lower frequencies 454 kHz and 140 kHz (pulse energy 30 µJ and 100 µJ, see Table 4.1), the laser spot distances become bigger. In the classic path filling method, the spot distances become 0.33 µm and 1.07 µm and for the classic hatch method they become 1.54 µm and 5 µm, respectively.

Table 4.4. Output laser power applied with three laser pulse energies without external trigger control of the laser spot overlapping regime.

Scanning strategy	Scanning speed v_{sc} (m/s)	External trigger frequency f_{trg} (kHz)	Laser spots distance r_d (µm)	Laser pulse period t_{lp} (µs)	Laser power P (W) at 10 µJ	Laser power P (W) at 30 µJ	Laser power P (W) at 100 µJ
Classic path filling	0.15	-	0.13	0.85;2.2;7.14	10	13.6	13.8
Shifted path filling	8	40	7	$17.4 \cdot 10^3$	0.4	1.2	4
Classic hatch	0.7	-	0.6	0.85;2.2;7.14	10	13.6	13.8
Shifted burst	8	40	7	0.85;2.2;7.14	10	13.6	13.8

The output power in laser scanning without an external trigger becomes equal for most of the scanning strategies. Only the shifted path filling strategy has low output laser power, but this limitation is dictated by the maximal speed value of the applied galvanometer scanner. The constant laser spot distance in combination with maximal high scanning speed is the main feature of the shifted path filling strategy, in contrast to the classic methods. Modern galvanometer scanners are able to produce scanning speeds up to 30 ÷ 40 m/s [299], [300]. At such speeds, the shifted path filling strategy would be able to use up to 50 W of power. In combination with laser beam dividing technology, for example with ten beams, the applied power escalates up to 0.5 kW.

4.6.4. Thermo-physical model of heat accumulation in laser-scanned surfaces

The heat accumulation can be evaluated from the thermo-physical model as summed heat from a sequence of applied laser pulses (Eq. 2.14). This model does not include full aspects of ultrashort laser pulse interaction with material as phase transformations and ultrashort time heat transfer like in the TTM model, but describes the heat accumulation as post-ablation temperature changes in the laser-scanned subsurface layers. In the calculations with laser beam scanning along the surface, the heat source should be described with consideration of the spot overlapping. The combination of scanning speed and laser pulse frequency defines the value of the spots overlapping. Especially, when we need to know temperature changes under a fixed surface point with laser beam scanning across the surface. In this case, every next laser pulse brings to the analyzed surface point a different value of the thermal energy, according to the Gaussian distribution [301], [302]:

$$F = F_0 \cdot e^{-2r/w_0}, \tag{4.16}$$

where F – laser fluence in the fixed point on the scanned surface (J/cm^2), F_0 – laser fluence in the center of the laser spot, which is given by $F_0 = 2 \cdot P/(\pi \cdot \omega_0^2)$, P – total energy in the

beam, r – distance from the laser spot center to the fixed surface point. The ultrashort duration of the laser pulse and the small lateral gradient of the laser fluence along the laser spot give the possibility to divide the one temperature distribution task into several semi-planar tasks [125]. Temperature distribution from the laser spot at a certain point distance r from the center will be described as temperature distribution from the planar heat source with fluence F, which is defined in Eq. 4.16. This assumption helps to reduce the temperature distribution problem to the well-known instantaneous planar surface source task (Fig. 4.6.6) [214], [303].

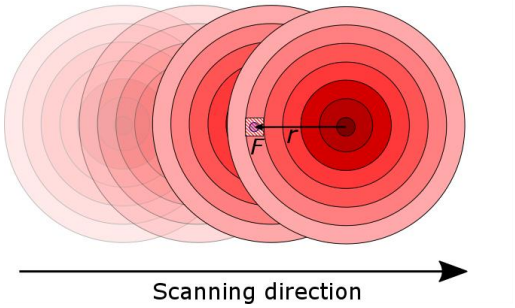

Fig. 4.6.6. The scanning laser spot area divided into thin rings with an internal radius r, where the fluence was defined as instantaneous plane surface source F [304]. Every next laser spot has a different fluence F in the fixed surface point.

Laser pulse-induced energy is reduced by the reflection of the beam and dissipation in the ablated material. The residual heat F_{heat}, which remains in the post-processed surface, can be defined by the fraction coefficient:

$$\eta = F_{heat}/F. \tag{4.17}$$

The fraction coefficient η is assumed to be a constant value equal to 12.5%. The selected value of the fraction coefficient was fitted by comparison of the experimental results of material laser drilling with theoretical prediction of the heat accumulation [14]. The resulting equation for the temperature history for any surface point inside of a single laser spot has the form:

$$\Delta T(t,z) = \frac{\eta \cdot F \cdot e^{-\frac{2r}{w_0}-\frac{z^2}{4\cdot\alpha\cdot t}}}{\rho \cdot c \cdot \sqrt{\pi \cdot \alpha \cdot t}}. \tag{4.18}$$

The temperature changes in a fixed surface point under a multi-pulsed scanned laser beam is described as the summed temperature history from all laser pulses applied in the investigated surface point:

$$\Delta T_{Sum}(t,z) = \left(\eta \cdot F/\rho \cdot c \cdot \sqrt{\pi \cdot \alpha}\right) \cdot \sum_{n=1}^{N} e^{-\frac{2r_n}{w_0}-\frac{z^2}{4\cdot\alpha\cdot t}} \Big/ \sqrt{t - t_n}, \tag{4.19}$$

where n – order number of laser pulse applied over a fixed point, N – full number of laser pulses over a fixed point, which were applied till actual time t, r_n – distance between the fixed point and the center of the applied laser spot, t_n – time, when the laser pulse with index n was applied.

The described thermo-physical model of heat accumulation in a fixed point on a scanned surface has a viewpoint different from the models presented in the literature. In the known literature sources, the heat accumulation is defined for a static laser surface drilling or as the temperature changes under the first leader spot in the laser beam scanning path [14], [215]. The approach presented here is more suitable for the characterization of temperature changes recorded by IR radiation detectors. The temperature changes predicted in this model for a nickel-based alloy has an evident maximum, similar to the IR radiation recorded from a fixed IR detector (Fig. 4.6.7; compare with channel 1 in Fig. 4.6.3, *a* and results from the literature in Fig. 2.2.7).

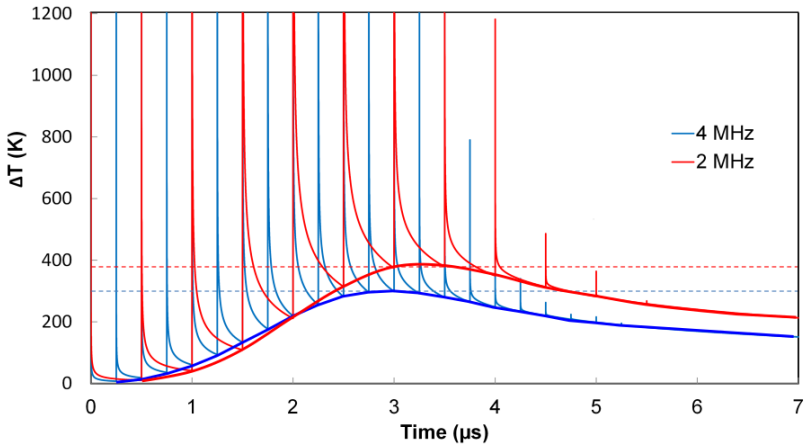

Fig. 4.6.7. Predicted surface temperature changes and heat accumulation temperature increase in a fixed point on the surface of a nickel-based alloy for two different laser beam parameters (red: $f_{pulse} = 2$ MHz, $Q_p = 5.79$ µJ, $v_{sc} = 8$ m/s; blue: $f_{pulse} = 4$ MHz, $Q_p = 2.09$ µJ, $v_{sc} = 8$ m/s) [302].

For the calculations, temperature dependencies of thermal and mechanical properties of stainless steel AISI304 (from MPDB [285]) were applied. Minimal geometry discretization steps were set at Δx, Δy, $\Delta z = 500$ nm and the time step was equal to 0.1 ns. The depth temperature distribution was analyzed at five equidistant subsurface layers to a maximal depth of 5 µm. The calculations of residual temperature which were done by the algorithm presented here were compared with calculations from analogous models from the literature. The semi-planar model presented here and results known in well-cited works of F. Bauer and R. Weber have a deviation of 50 ÷ 100 degrees only [215], [305].

The results of the heat accumulation calculations can be compared with direct IR measurements by conversion of the analytically evaluated temperature to the thermal radiation intensity. The fundamental principle of this conversion is lies in Planck's law for emitted electromagnetic radiation [306]. The intensity of the IR radiation $I(\lambda)$ emitted by the laser-heated surface has exponential dependency on temperature:

$$I(\lambda)d\lambda = \frac{2\pi hc^2}{\lambda^5}\frac{1}{e^{hc/\lambda k_b T}-1}d\lambda. \tag{4.20}$$

The conversion of surface temperature to IR radiation intensity makes a comparison of experimental measurements with analytical calculations more relevant. It is necessary to note that the intensity of the thermal radiation from real materials has dependence on emissivity and wavelength. There is no need to set a precise value of the surface emissivity, since the evaluation of temperature regimes of laser surface processing with different scanning speeds and frequencies is a more relevant concept. However, the emissivity in the analytical model of the heat accumulation was set equal to a realistic value for stainless steel equal to 0.149 [303] in order to improve the theoretical predictions. The spectral radiance was calculated for wave length $\lambda = 3\ \mu\mathrm{m}$ and this corresponds to the shorter wavelength limit of the IR detector on channel 1. This value of the wavelength is close to the lower limit of the PIN photodiode on the second channel.

4.7. Summary of experimental methods and analytical modeling

In this section, the experimental and evaluation methods of laser surface scanning are described. The InnoSlab laser with 10 ps pulse duration and 532 nm wavelength was used. The laser beam delivery was done with a galvanometer scanning head and an F-Theta objective with a 255 mm focal length objective. The laser surface scanning was carried out with one-dimensional and two-dimensional strategies. A new two-dimensional scanning shifted LST method was developed for achieving higher speeds and higher precision of laser surface processing. The methods of evaluating LST microobject diameter deviation and depth profile evaluation are described.

The heat accumulation evaluation method and plasma glow process analysis are described for an experimental setup with three IR photodiodes. The procedure of heat accumulation evaluation is based on a statistical subtraction algorithm. All together experiments: heat accumulation detection, speed limits assessment and plasma glow evaluation takes more than a thousand measurements. The thermo-physical model of heat accumulation in a fixed surface point under a laser beam scanning line is presented for comparison of the experimental results with theoretical predictions.

5. Results and discussion

5.1. Characterization of laser surface scanning regimes

5.1.1. Heat accumulation in one-dimensional laser surface scanning

Dependence of the residual heat IR signal on scanning speed

One of the simplest methods of LST is laser beam writing of straight lines on a processed surface. In this part, the results of heat accumulation evaluation from the IR radiation signal detected in the linear laser surface scanning are presented. The experiments with straight lines were intentionally applied at the slowest scanning speed for definite determination of the heat accumulation IR radiation signal in the laser-affected area. The minimal applied scanning speed was 0.007 m/s, with distance between laser spots ~ 10 nm only (Table 4.1). Such a short distance between laser spots corresponds to the maximal laser spot overlapping, almost full laser spot size. As expected, the high laser spot overlapping initiated noticeable heat accumulation and high IR emission from the laser-scanned surface. The detected heat accumulation IR signal U_h was analyzed using a subtraction algorithm (Eq. 4.12). The heat accumulation IR radiation signal at minimal 0.007 m/s scanning speed was 15 times greater than the signals at the higher speeds (Fig. 5.1.1). The IR heat accumulation signal value promptly decreases with speed increasing to 0.07 m/s. In the region of the speeds 0.07 ÷ 3 m/s, the heat accumulation IR signal slowly decreases to a minimal value and it can be described as a region with medium heat accumulation. At higher speeds, the heat accumulation IR signal is slightly increased and this can be explained by less plasma and ablation cloud shielding at the wider distance between laser spots.

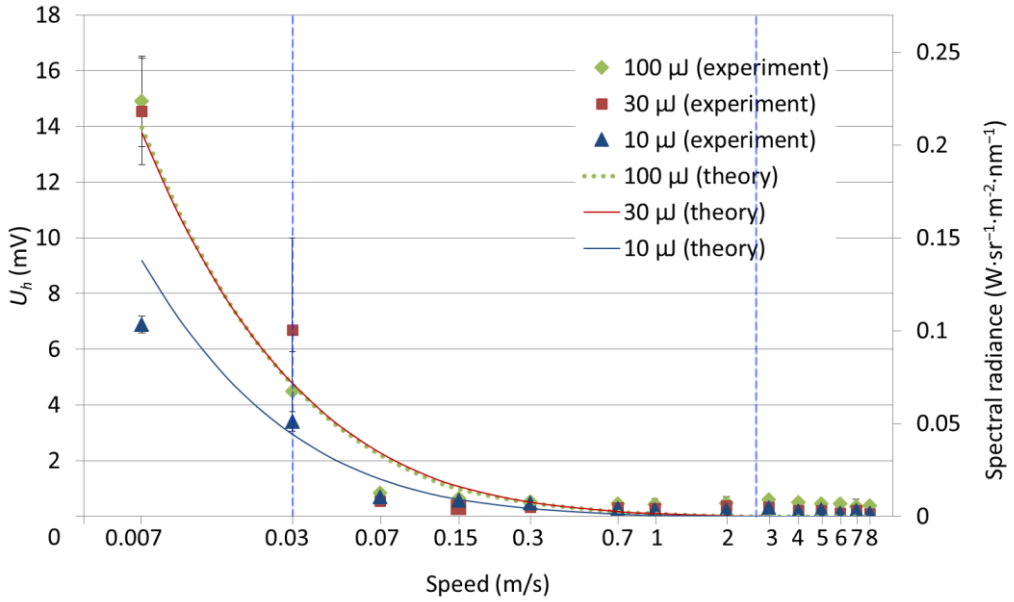

Fig.5.1.1. Residual heat accumulation IR radiation signal detected on channel 1 with linear raster LST (markers with SD bars) and IR radiation predicted from the analytical model (lines). The vertical lines indicate characteristic regions of heat accumulation.

Characteristic speed regimes in one-dimensional laser surface scanning

The data about residual heat, which were obtained from the IR radiation signal by application of Eq. 4.12, were compared with predictions of the analytical model of the heat accumulation (section 4.6.4). In Fig. 5.1.1, the IR signal predicted from the analytical model is marked by lines and experimental values by markers. The thermal regimes of the laser surface scanning are classified by predicted temperatures. The first area corresponds to the lowest speed and indicates the scanning regimes where the predicted temperature exceeds the evaporation point (Table 5.1, red color). The analytical model did not include phase effects, radiation area extension and other optical changes which occur at the extremely high temperatures and low scanning speeds. The calculated temperatures in this case have an approximate character and are presented as indicating values (placed in brackets in Table 5.1).

Table 5.1. The characterization of the laser surface processing by the IR radiation signal and predicted heat accumulation temperature (colors categories are described in the text).

Energy (μJ)	**10**		**30**		**100**	
Speed (m/s)	U_h (mV)	T (°C)	U_h (mV)	T (°C)	U_h (mV)	T (°C)
0.007	6.89	(4866)	14.55	(6423)	14.90	(6478)
0.03	3.40	(2634)	6.69	(3344)	4.49	(3327)
0.07	0.70	(1906)	0.55	(2354)	0.85	(2318)
0.15	0.57	(1472)	0.32	(1762)	0.65	(1712)
0.3	0.47	1200	0.34	1397	0.53	1382
0.7	0.29	918	0.32	1071	0.45	1063
1	0.24	803	0.29	963	0.44	956
2	0.24	607	0.39	735	0.49	645
3	0.31	501	0.35	604	0.60	356
4	0.20	435	0.22	528	0.50	107
5	0.25	383	0.21	463	0.46	52
6	0.13	342	0.12	404	0.47	33
7	0.23	319	0.23	347	0.35	29
8	0.11	299	0.11	293	0.38	28

The scanning speed region between 0.3 ÷ 3 m/s lies under liquid phase appearing and corresponds to the heat accumulation above the critical temperature regime ($T_s \geq T_{th} = 607\ °C$). The boundary speed 3 m/s of the critical temperature regime varies for the different pulse energies and it has maximal value for the laser pulses with 30 µJ energy (Table 5.1, orange color). The lower temperatures at the boundary speed 2 m/s were predicted for the two opposite pulse energies 10 µJ and 100 µJ, whereas the IR signal is higher for the last one (Table 5.1, yellow color). The average power for all three values of the laser pulse energy is nearly the same, 11 ÷ 13 W. The higher IR signal value at 100 µJ can be explained by increase of the spot size and electron ballistic depth penetration at the higher laser pulse energy. The predicted temperature decrease and lower detected IR signal have a similar tendency at higher speeds. This makes it possible to identify the common principles of laser material processing with low heat accumulation:

- heat accumulation can be overcome at speeds higher than 2 ÷ 3 m/s, even with overlapping larger than 10% (compare with Table 4.1);
- with the application of equal average power, lower heat accumulation can be achieved rather with a higher frequency and lower pulse energy, in contrast to a higher pulse energy and lower frequency.

Comparison of the evaluated heat accumulation data with literature sources

The second result, regarding application of equal average power, is opposite to the theoretical predictions published by Weber et al. [14], where higher heat accumulation occurred at a higher frequency of laser pulses. Such a difference can be explained by including the relative movement of the Gaussian laser beam across a fixed surface point. In the theoretical models reported in the literature, the heat accumulation is analyzed in a moving surface point under a scanning laser beam or in percussion drilling [14], [215]. Unlike those, in the model presented here the temperature changes are analyzed under a fixed point on the scanned surface. This relative difference of our model gives an unusual result: that maximal heat accumulation in the fixed spot can be higher at the moment when the direct hit of a laser pulse is already gone and one later pulse is applied – the third, fourth or even later laser pulse.

Dependence of the maximal temperature IR signal on the laser beam scanning speed

The heat accumulation affects the maximal temperature changes in the fixed point on a scanned surface. The dependence of the relative maximum U_{mb} on the scanning speed is presented in Fig. 5.1.2. The thermal IR radiation shows a nonlinear difference between the three applied pulse energies 10 µJ, 30 µJ and 100 µJ (Fig. 5.1.2). At the slowest scanning speeds 0.007 ÷ 0.15 m/s and laser pulse energies 10 µJ and 30 µJ, the value U_{mb} has the exponential character of temperature decreasing. For the highest frequency (1176 KHz and 10 µJ), this effect is most expressed. The maximal value $U_{mb} = 11.250\ \mathrm{mV}$ at speed 0.007 m/s and the later value $U_{mb} = 3.95\ \mathrm{mV}$ at 0.3 m/s show decrease in the maximal temperature, dropping more than 300%. This result demonstrates the greater influence of heat accumulation on the maximal achieved temperature at higher frequencies of the laser pulses.

The reduction of maximal temperature was detected in the experiments with 100 µJ pulse energy. In the middle scanning speed region 0.3 ÷2 m/s, the reduction can be explained by the plasma and ablation products' shielding effects with laser pulse overlapping. The higher maximal IR radiation signal at scanning speeds 2 ÷ 8 m/s can be explained by the increase of the laser spot distance up to the distant distribution of the laser pulses at speeds $v_{sc} \geq 3$ m/s (see Table 4.1). As a result, the shielding effects have a small influence and the maximal temperature under the laser spot becomes higher with the detection of the higher IR radiation peak signal.

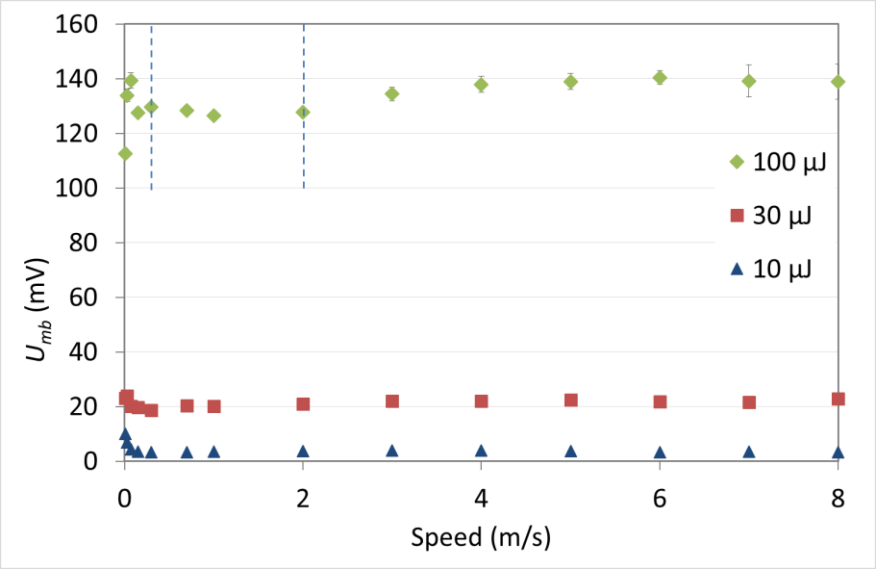

Fig. 5.1.2. The dependence of the maximal IR radiation signal from the laser processed surface detected on channel 1 in linear scanning.

Higher temperature NIR signal changes in one-dimensional laser surface scanning

The NIR radiation signal recorded on channel 2 was evaluated by the same algorithm as it was done for channel 1. The photodiode on channel 2 detects the higher temperature IR signal (lower spectral limit is 1.1 µm, corresponding to 2635 K under Wien's Displacement Law). The residual IR radiation signal of heat accumulation is low, about microvolts only, and it is near the noise value (Fig.5.1.3). The very low level of the residual IR signal on channel 2 indicates that the laser ablated surface has enough time for cooling. Unlike with the application of short laser pulses [228], the laser surface processing with ultrashort pulses is not characterized by a long-term phase plateau of IR radiation and this indicates that there is no melted surface layer remaining between laser pulses.

The maximal NIR radiation signal on channel 2 (Fig.5.1.4) has less expressed dependence on scanning speed in comparison with the first channel, even for the slowest scanning speeds (Fig.5.1.2). Above all, an increase of the SD (Standard Deviation) on channel 2 with the maximal laser pulse energy 100 µJ was detected. In the literature review, it was mentioned that ablated materials after irradiation by ultrashort laser pulses have great speeds, up to 8 ÷ 10 km/s [136], [161]–[163]. The ablated material is distributed with

formation of protuberances [307]. The variety of the NIR temperature signal from the high temperature channel at the highest pulse energy and wider distance between laser spots can be explained by the variable shielding of every next laser pulse by the tattered edge of the ablated cloud.

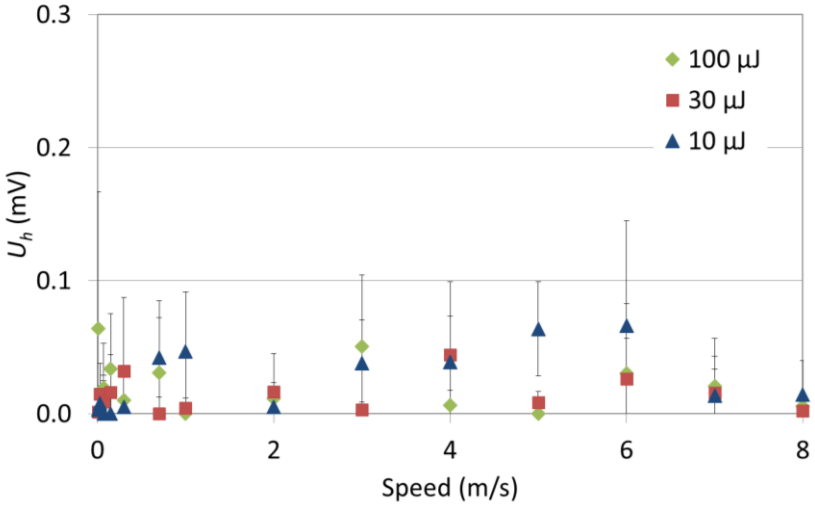

Fig. 5.1.3. The dependence of the heat accumulation IR signal detected on channel 2 in linear scanning.

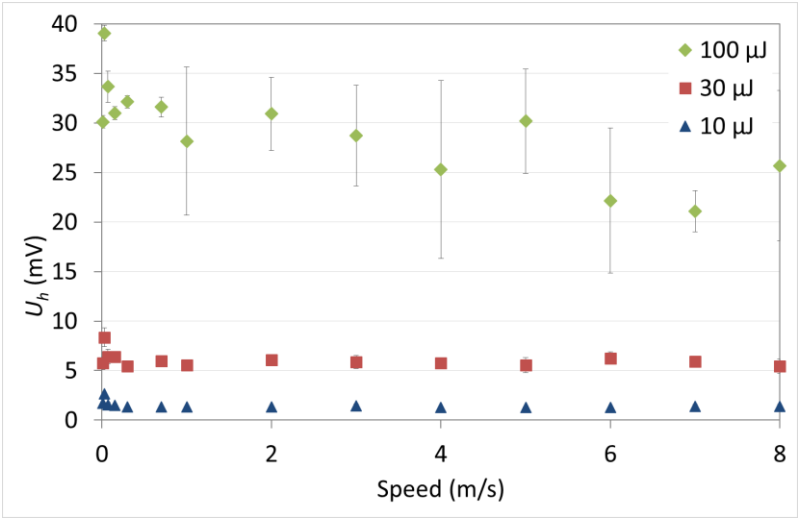

Fig.5.1.4. The dependence of the maximal IR temperature signal from the laser-processed surface detected on channel 2 in linear scanning.

Keynotes of heat accumulation in one-dimensional laser surface scanning

At the end of this section, four keynotes can be specified from the IR radiation signal analysis of the linear surface scanning and the comparison of the experimental data with the theoretically predicted temperature changes:

1. A high IR radiation signal was detected at scanning speeds lower than 0.07 m/s and this indicates an overheated regime (see Table 5.1).

2. At speeds higher than 0.07 m/s, the heat accumulation and maximal IR radiation signals have equal values, with a slight increase at higher speeds.
3. The heat accumulation was not detected on the second channel and this indicates that the real residual temperature has not reached above melting point.
4. The predicted temperature of IR radiation has reasonable agreement with the detected IR signal. Three levels of heat accumulation were defined for the applied scanning speeds: low heat accumulation (3 ÷ 8 m/s), critical heat accumulation (2 ÷ 0.07 m/s) and overheated (< 0.07 m/s).

The defined scanning speed regions are similar to the different laser pulse energies and this can be explained by the different applied frequencies of the laser pulses. At the surface scanning with laser pulse frequency reduction by an external trigger, the speeds of the critical and low heat accumulation regimes can be lower.

5.1.2. Dependence of plasma glow duration on scanning speed in one-dimensional laser surface processing

Interesting results were obtained from analysis of the data on the third channel (Ch 3). On this channel, the time duration of plasma glow was analyzed instead of the signal level. A time analysis of time-depended function is better in this case, because the maximal signal on the third channel is integral and affected by the laser pulse reflection. The detected plasma glow was long, 100 ÷ 250 ns, for most of the applied laser beam scanning speeds (Fig.5.1.5). The plasma glow at lower scanning speeds $v_{sc} < 1$ m/s has the longer duration t_w~250 ns (Fig.5.1.6, *a*). In the scanning speeds region 1 ÷ 3 m/s, the residual temperature of the laser-scanned surface is higher than the critical value (see Table 5.1) and the ablated plasma glow duration has nearly the same duration ~200 ns. At the higher speeds, the plasma glow radiation signal duration becomes shorter and it drops down to 150 ns and shorter (Fig.5.1.6, *b*).

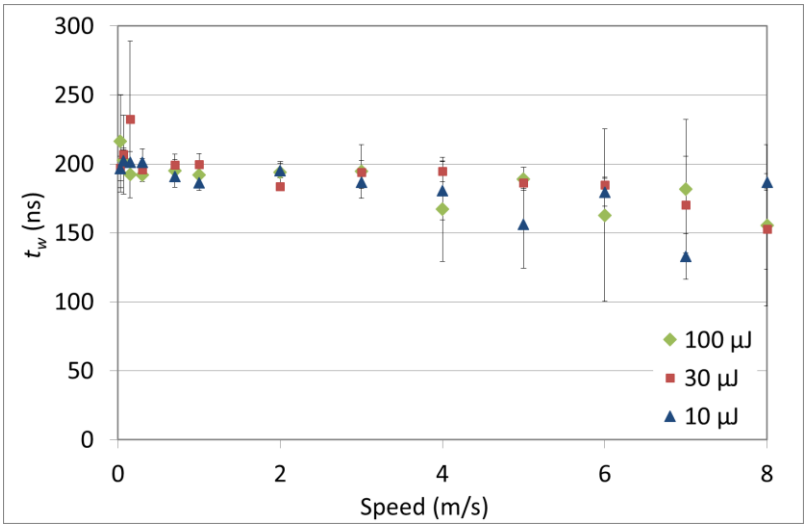

Fig. 5.1.5. Ablated plasma glow duration in dependence on the laser beam scanning speed in linear scanning (channel 3).

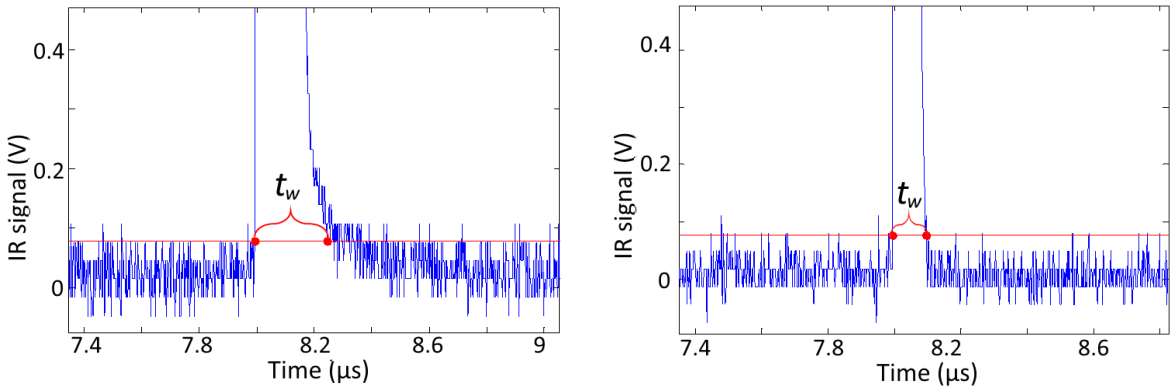

Fig.5.1.6. Examples of ablated plasma glow duration for laser pulse energy 100 μJ and for different linear scanning speeds: *a* – glow duration 249 ns (scanning speed 0.15 m/s); *b* – two times shorter glow duration 102 ns (scanning speed 8 m/s).

The decrease of the laser-ablated plasma glow duration for the higher scanning speeds can be explained by the different state of the irradiated surface with lower heat accumulation. At lower scanning speeds, the processed surface is in a preheated state between sequential laser pulses. This leads to change in several of the physical parameters of the laser pulse interaction with the material, like the absorption value or ablation threshold. As a result, the ablated plasma plume can have a higher part of the absorbed laser pulse energy and a longer time period stay to be exited.

The next feature of laser surface scanning with sequential laser pulses is the presence of the post-ablated materials over the scanned surface. The ablated microparticles and vapors after the previous laser pulse remain in the closest volume to the next laser pulse position. The inhered ablated particles and partially ionized vapor are able to change the laser-matter interaction mode from absorption in a solid to stronger and more localized absorption on a plasma density gradient [308]. Such interaction of the laser pulse with a surface covered by a vapor-particle cloud has a different nature than the single-pulse interaction with a clear target. In these conditions, the ablation threshold can decrease and the ablated plasma glow contains a bigger amount of energy. And again, the higher energy in the ablated plasma plume leads to increase in glow duration.

The decrease of the plasma glow duration at higher scanning speeds can be explained by the mentioned physical principles of the higher energy of the ablated plume from the post-ablated material surface. At higher speeds, every next laser pulse meets the scanned surface with a lower temperature and lower density of the post-ablated cloud due to the wider distance between laser pulses. In other words, the inline energy density becomes lower and as a result, the ablated plume contains a smaller part of the heat energy which was inherited from the previous laser pulses. The total energy of the ablation plume becomes smaller at higher speeds and this leads to the shorter duration of the plasma and ablation products' glow.

Near the critical and low heat accumulation (see Table 5.1), the amount of the residual heat in the plasma plume will be relatively small and the decrease of the plasma glow duration does not express dependence on the scanning speed. This assumption is supported by measurements of the maximal value of the signal U_{mb} on the first and second detectors (Fig. 5.1.2 and Fig. 5.1.4). The maximal value of the IR signals has a similar tendency on both channels – it tends to increase at the speeds up to 3 m/s. The ablated plasma glow duration has an inverse dependence and noticeably drops at the speeds higher than 3 m/s (Fig. 5.1.5). This correlation between plasma glow duration and the maximal value of the thermal IR signal can be considered an alternative way to registration the undesired heat accumulation in the laser surface ablation processes.

Another plasma characteristic can be seen in the dynamics of the plasma glow decrease. The plasma glow signal decrease is affected by both: electron transitions between energy levels in the exited atoms and by the decrease of the particle density in the ablated plasma plume [309]. The process of the spontaneous emission of the exited atoms described by Einstein coefficients and typical of the decay time for such processes is less than 10 ns [310]. A similar decay time of the plasma plume can be achieved by the extremely high expansion speed of the ablated products up to 8÷10 km/s ([136], [161]–[163]) from the high initial density of 10^{22} particles per cm^3 (initial density of the solid). For the differentiation of these two effects, high-speed spectral analysis needs to be applied. Such measurements, in combination with detection of IR radiation from the post-ablated surface, can be used in an comparative analysis in follow-up studies.

5.2. Scanning parameters of the two-dimensional LST methods

5.2.1. Lateral precision and speed limits in laser texturing of micro-dimples

Classic path LST and shifted path LST methods

The processes of laser surface texturing with the formation of a micro-dimples array on a surface are presented in two parts. In this part, results of the detection of laser scanning speed limits for the classic and shifted LST methods are presented. The speed limits were evaluated by detection of the laser-formed microobjects on LabIR® painted surfaces (Fig. 4.3.1). In the classic path filling method, a diameter deviation $\overline{\xi}$ bigger than 5% was already observed at scanning speeds v_{sc} > 0.15 m/s (Fig. 5.2.1). The main reason for such low precision at low scanning speeds can be explained by the inertia principle of the galvanometer scanner and the small radius vector of the microobjects in the classic path method. The microobjects' circularity deviation $\overline{\xi}$ can be detected already at low laser beam scanning speeds as an unclosed outline (Fig. 5.2.2, left column, speed 0.7 m/s). For the classic path filling method, the diameter deviation $\overline{\xi}$ rise to more than 20% at the scanning speeds v_{sc} higher than 0.7 m/s and follow-up evaluation experiments were not done for this method. The standard deviation s in the classic path filling has a minimal value of 1.73% at minimal speed and it increases to more than 5% at higher speeds. The increase of the standard deviation indicates that the laser beam movement in the classic LST with higher speeds becomes unstable. The inability of the

classic path LST method to correctly close the filling paths at higher speeds is caused by the inertia of the mirrors for correct bending of the scanned path at small curvature vectors.

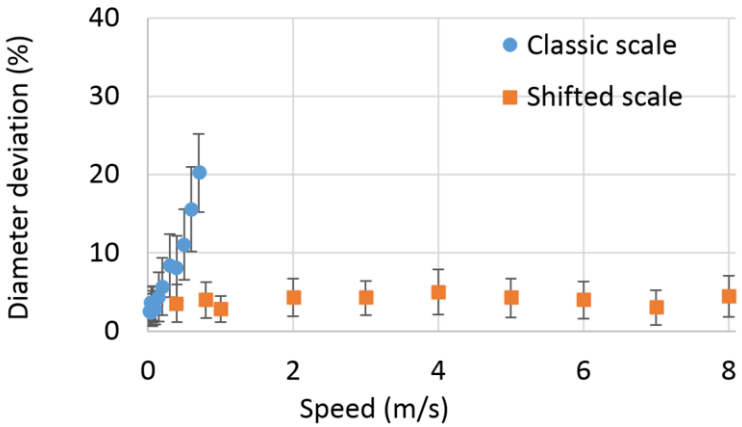

Fig. 5.2.1. Diameter deviation of the laser-textured dimples performed by classic path filling (blue circles) and shifted path filling (orange circles) methods. The vertical bars show the SD of the corresponding LST methods.

The shifted scanning method with path filling has a minimal scanning speed of 0.4 m/s since the limitation of the external trigger frequency is equal to 1 kHz. The diameter deviation $\overline{\xi}$ for this scanning method remains smaller than 5% up to maximal scanning speed $v_{sc} =$ 8 m/s. The SD of the shifted LST remains near 2.5% for all tested speeds. This indicates that the shifted LST process is more stable than classic path filling in the whole range of speeds. The dimple perimeters remains similar, as is demonstrated in Fig. 5.2.2 (right column). Only the relative position of the microobjects in the array rows is changed, due to phase changing of the laser external trigger generator at the different scanning speeds. The relative position of the laser-textured microobjects can be tuned up by length or relative shifting of the scanned rows in the LST raster.

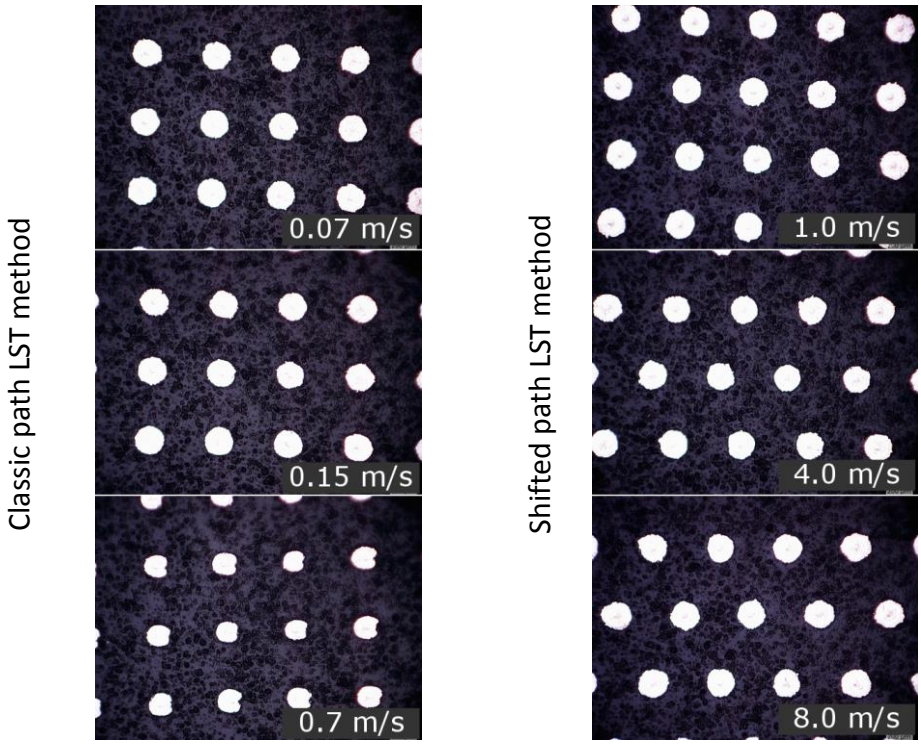

Fig. 5.2.2. Lateral LST with dimples formed by classic path filling (left column) and shifted path filling (right column).

The results define the maximal acceptable limits of the laser scanning speeds for the path filling with classic and shifted LST methods. The classic path filling LST method has achieved a precision limitation at $v_{sc} = 0.15$ m/s, while the shifted LST has satisfactory precision also at maximal scanning speed $v_{sc} = 8$ m/s. These two speeds were used in experiments with detection of heat accumulation for the corresponding classic and shifted LST methods.

Classic hatch LST and shifted burst LST methods

The precision of the next two methods, the classic hatch LST method and the shifted LST method in burst regime, were analyzed by the same logic. The results of the diameter deviation $\bar{\xi}$ measurements of the classic hatch method show higher precision than the classic path filling (Fig. 5.2.3). Similar to the classic path filling, the classic hatch method shows destabilization of the laser beam movement at higher speeds. The SD of the classic hatch method becomes bigger than 14% at higher speeds. The precision of the microobjects' circularity becomes unacceptable at speeds higher than $v_{sc} = 0.7$ m/s. The analysis of the microobjects' shapes has shown that the classic hatch LST method is not able to keep the correct position and length of the hatch segments inside of the dimples (Fig. 5.2.4, classic hatch LST, at the bottom).

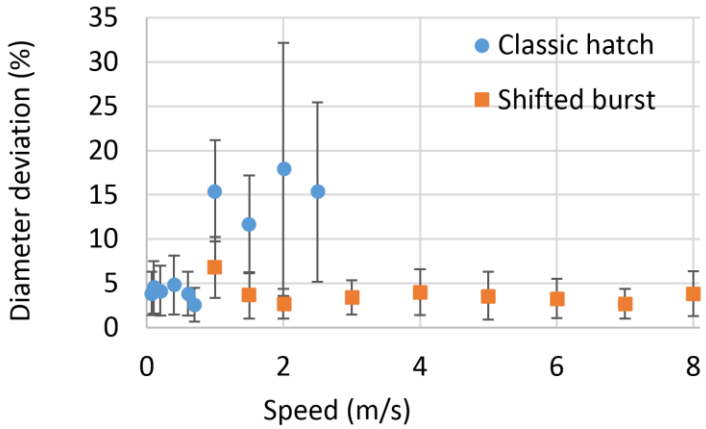

Fig. 5.2.3. Diameter deviation of the laser-textured dimples formed by the classic hatch (blue circles) and shifted LST in burst regime (orange circles) methods. The vertical bars show the SD of the corresponding LST methods.

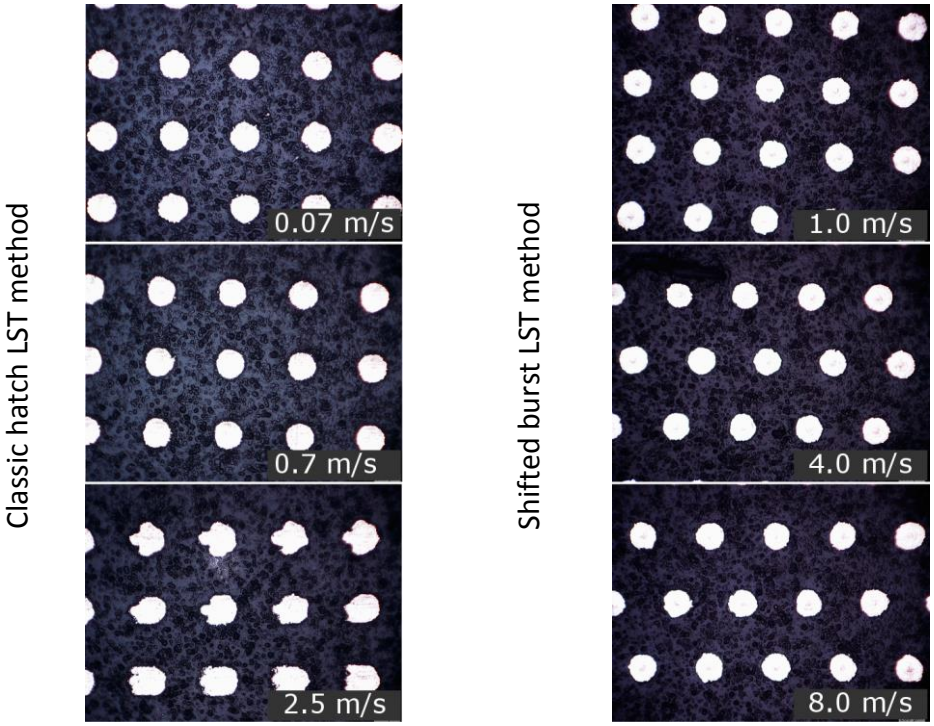

Fig. 5.2.4. Lateral LST with dimples formed by the classic hatch LST method (left column) and the shifted burst LST method (right column).

The shifted LST method in the burst regime (or shifted burst LST) has acceptable precision in almost the whole range of the tested speeds, including maximal speed 8 m/s, when the diameter deviation v_{sc} remains near the 5% limit. The laser beam movement remains stable because the SD value stays under 3.5% for the whole range of the speeds. Moreover, in the shifted burst method, the diameter deviation $\overline{\xi}$ decreases at higher speeds of the surface scanning. The low SD and smaller diameter deviation at higher speeds indicate

a positive influence of the mirrors' inertia with application of the shifted LST methods (Table 5.2). The difference in the diameter deviation of the shifted path LST and shifted burst LST methods can be explained by different trigger settings for both scanning methods.

Table 5.2. Influence of the mirrors' speed movement on LST stability in the application of the shifted LST methods.

Shifted path LST method			Shifted burst LST method		
Speed v_{sc} (m/s)	Diameter deviation $\overline{\xi}$ (µm)	SD s (%)	Speed v_{sc} (m/s)	Diameter deviation $\overline{\xi}$ (µm)	SD s (%)
0.4	3.53	2.42	1	6.81	3.46
0.8	3.97	2.28	1.5	3.66	2.62
1	2.81	1.66	2	2.70	1.69
2	4.30	2.40	3	3.40	1.95
3	4.24	2.18	4	3.98	2.59
4	4.98	2.89	5	3.60	2.70
5	4.25	2.47	6	3.30	2.21
6	3.94	2.37	7	2.68	1.67
7	2.99	2.21	8	3.82	2.52
8	4.42	2.62			

5.2.2. Precision in the depth profile of laser-textured micro-dimples

The next evaluation of the laser-processed surface geometry was the depth profile analysis of the laser-textured dimples. The results of the depth profile deviation for the different texturing methods are shown in Fig. 5.2.5. The results presented on the diagram were achieved at the highest acceptable scanning speed (speed limit of the LST methods). For all methods, the depth profile deviation ξ is lower or around 10%, so the precision of the shifted method in both variants is comparable or even better than that of classic methods, although done at a much higher scanning speed v_{sc}.

Typical examples of measured depth profiles and deviations Δ^P from the goal depth profile Δ_g^P are shown in Fig. 5.2.6. The most significant distortion of the depth profile was observed for the classic hatch-texturing method. The dimple bottom is not flat and is inclined by 1 ÷ 2 µm. The inclined bottom can be seen also in 3D profile views in the vertical direction of the profiles (Fig. 5.2.7). The difference in the profiles' forms can be explained by the effect of heat accumulation and incubation effects.

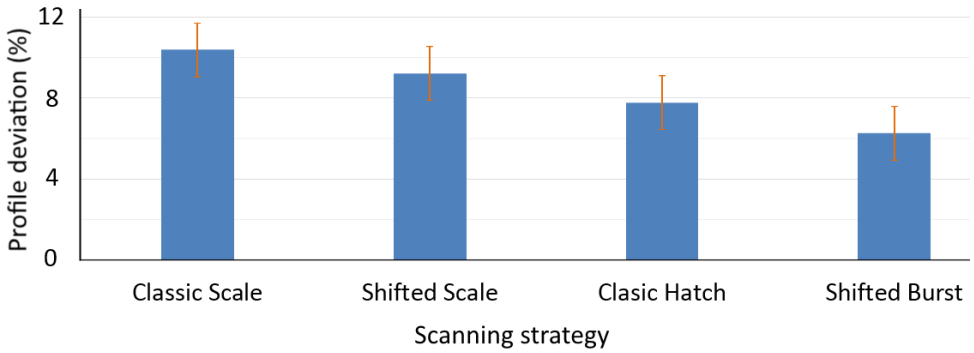

Fig. 5.2.5. The relative depth profile deviation for the different laser scanning strategies at their highest allowed scanning speeds.

The incubation effect means a decrease in the ablation threshold with the number of pulses reaching the same surface area. This can be explained by the change in the energy/optical penetration depth, reflectivity/absorptivity, roughness [19], accumulation of damage (defects) or surface chemistry [311]. If the ablation threshold is decreased, more energy goes into the material removal, when the same pulse energy is used. This means that the surface ablation process is different at the start point on a scanned segment and at the end of the scanned segment. As a result, the ablation depth is different at different places and the slope at the dimple bottom is formed with its deeper part at the end of the scanned segment. The laser ablation process with heat accumulation is faster and the depth of the dimple increases at the side with a higher starting temperature (end of hatch line or last line in the dimple). An interesting fact is that the depth change at the bottom is mainly in the laser beam scanning direction (ordinate on Fig. 5.2.7). This shows the important role of the inline heat accumulation on the incubation effects during laser scanning, while the effect from the previous lines is almost negligible.

On the other hand, when the time interval between neighboring laser pulses is optimally short, then better thermal conditions of the laser surface processing will be achieved. This can be seen in the burst regime with a flat output surface at the profile bottom (Fig. 5.2.7, shifted burst). In the classic methods, the thermo-chemical reactions, like surface oxidation, have more time to develop in the time period between laser pulses t_{lp}. The time interval between laser pulses t_{lp} remains short enough to sustain the higher residual temperature of the laser-scanned surface (Table 4.3). In the high-speed shifted path method, the situation is similar: the laser pulses are divided by long time intervals. But, in the shifted path method the laser pulses are divided by a thousand times longer period, more than ten milliseconds. The heat accumulation between laser pulses becomes negligibly small and the thermo-activated chemical processes cannot be sustained, unlike in the classic path method. This difference between path LST methods would explain the difference in the bottom structure of the micro-dimples obtained by these two strategies, even for the same laser spot distribution (Fig. 5.2.7, classic path and shifted path).

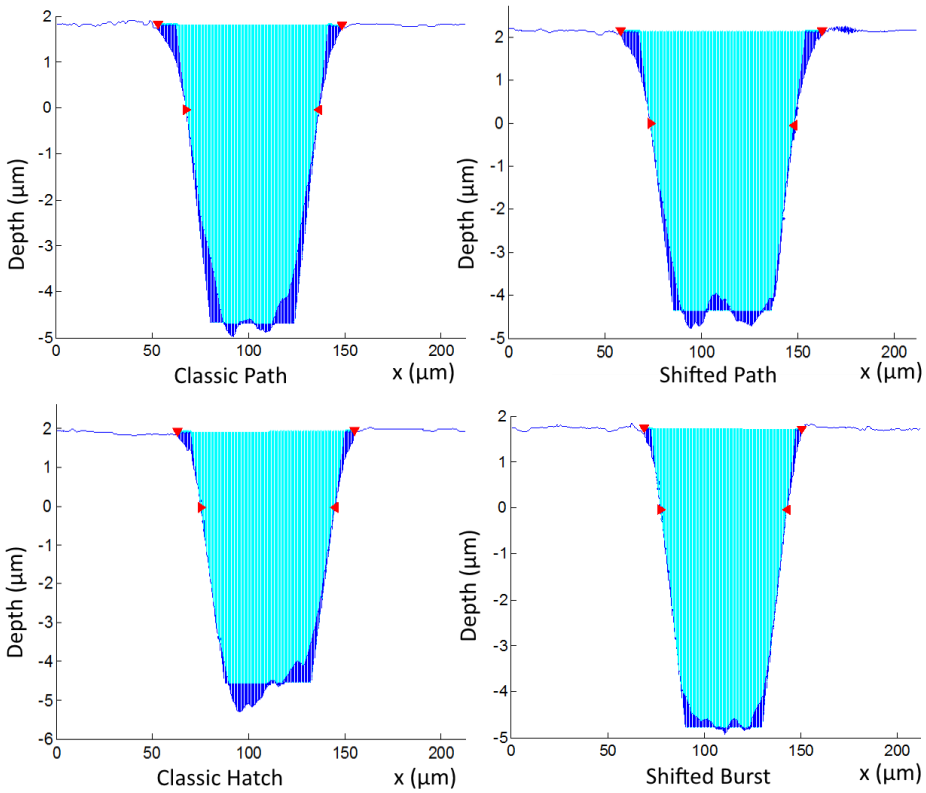

Fig. 5.2.6. Comparison of depth profiles of dimples produced by different laser texturing methods (scanning strategies) at their highest allowed scanning speeds. The dark blue areas present deviation Δ^P of the surface profile from the goal depth profile.

For the classic path method, the central part of the dimple is deeper (bottom is narrower, Fig. 5.2.6). This correlates with the highest temperature and higher incubation effects in the center, where most of the laser pulses occur in a short time. For the shifted burst method, the heat accumulation (or incubation) is forming at a different time scale (fast scanning and high repetition frequency) than for the classic hath method and probably takes place immediately after a few pulses and is stable during most of the line inside the dimple. The resulting dimple is well machined and so the heat accumulation temperature here is under the threshold critical temperature of material degradation of the material and the effect of heat accumulation and incubation is not negative.

The number of repetitions of the texturing process for complete depth was different for the different LST methods. It was defined after several tests in order to obtain the desired depth profile. For classic path it was 45 repetitions, for shifted path 60, for classic hatch 85 and for shifted burst 90 repetitions. The classic path method gives a narrower dimple at the bottom part (Figs. 5.2.6 and Fig. 5.2.7) and this is explained by the heap effects in the central part for the classic path method, which, on the other hand, means a higher ablation rate and correlates with the lower number of repetitions needed for obtaining the desired depth (45 scans in comparison with 60 scans for the shifted path method).

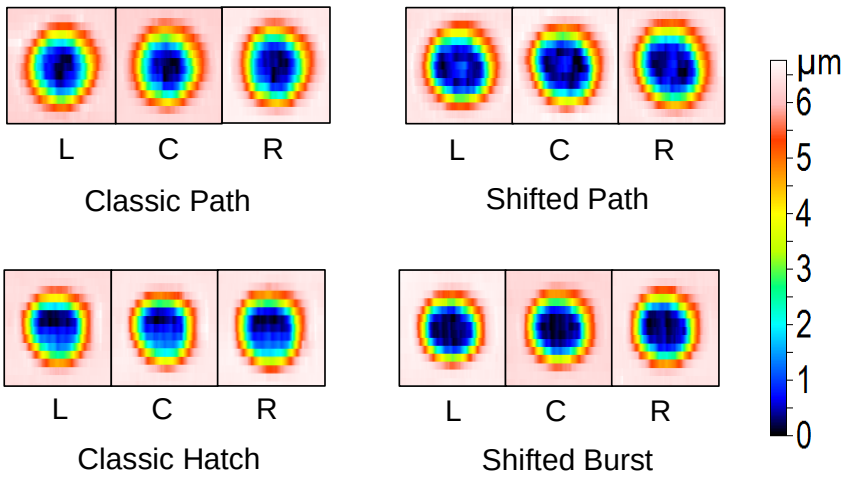

Fig. 5.2.7. Comparison of depth profiles of dimples produced by different LST methods (scanning strategies) at their highest allowed scanning speeds. Images are taken from three places in the 170 mm long textured area: L – left, C – center, R – right.

The profiles' variability detected for every LST method can be seen from the depth profiles measured from three different parts of the textured surface (Fig. 5.2.7): left, center and right. It can be seen that for each method the process is repeatable with only small changes. The variability in the profiles' imperfection depends on the applied LST scanning strategy. The statistical analysis of measured depth profiles is shown in Fig. 5.2.5 as error bars for different texturing methods. The smallest difference and thus the highest repeatability of depth profiles was found for the shifted burst method.

5.2.3. Processing rates of LST methods

Processing rate of the classic and shifted LST methods measured in the experiment

The results of the precision evaluation were used in the next series of experiments for defining the processing rate and detection of the heat accumulation in the lateral LST methods. Four scanning speed limits were observed, as was already stated in section 4.5.4. Since the scanning speed v_{sc} of the classic methods is more than ten times lower than that of the shifted methods, the processing rate v_{pr} has a similar difference. Table 5.3 presents the processing rates v_{pr} of the tested LST methods, which were measured in one layer surface scanning.

Table 5.3. Processing rates defined in one scanning layer with the different LST methods.

Method	Beam speed v_{sc} ($\overline{\xi}$< 5%)	Frequency f_{pulse} (kHz)	LST time for 10^4 objects	Processing rate v_{pr} (cm^2/min)
Classic path LST	0.15 m/s	21	47 sec	5.11
Shifted path LST	8 m/s	40	14 sec	17.14
Classic hatch LST	0.7 m/s	100	37 sec	6.49
Shifted burst LST	8 m/s	1143	1.5 sec	160.0

The shifted burst LST has a maximal processing rate of $v_{pr} =$ 160 cm^2/min and this is comparable with polygon scanner technology (see Appendix A). The processing rates of the lateral shifted LST methods is more than 24 times faster in comparison with classic LST methods. The advantage of the shifted LST is the laser pulse being delivered in an asynchronous way. The asynchronous character of the shifted LST eliminates the limiting connection between the laser generator and mirror movement. The processing rate benefits of the shifted LST methods for the depth texturing is discussed in the following comparison.

One scanning layer is able to remove a thin surface layer from the stainless steel samples and the depth of texturing will be 100 ÷ 200 nm only. The formation of a deeper surface texture profile, down to a 6.5 µm depth of the dimples, needs an application of 45 ÷ 90 scanning layers in dependence on the chosen LST method. In Fig. 5.2.8, the processing rates obtained from a smaller area (2 × 10 mm^2) are presented in comparison with a larger texturing area (2.4 × 170 mm^2). The time of the laser surface texturing is measured for complete dimple processing to the goal depth and for corresponding speed limitations of the LST methods. The highest processing rate was found for the shifted method in burst mode, $v_{pr} = 146\ \mathrm{mm}^2/\ \mathrm{min}$. The processing rate $v_{pr} = 12.6\ \mathrm{mm}^2/\mathrm{min}$ for the classic path LST method was found. The lowest processing rate was found for the classic hatch method, $v_{pr} = 3.4\ \mathrm{mm}^2/\mathrm{min}$. This is a huge difference – the shifted burst method is 43 times faster than the classic hatch and more than 11 times faster in comparison with the classic path LST method. The processing rate was also calculated from the software prediction of the elapsed time (Fig. 5.2.9).

The calculated time of the surface texturing is shorter than the experimental measurements. For example, the calculated processing rate for the classic hatch method is the more favorable $v_{pr} = 6.8\ \mathrm{mm}^2/\mathrm{min}$ in comparison with the experimental value $3.4\ \mathrm{mm}^2/\mathrm{min}$, but it is still the lowest speed in contrast to the other LST methods. The difference between the software prediction and the real measured production time highlights that the synchronization processes have slowed the texturing speed. For the shifted burst method, the predicted processing rate (177 mm^2/min) is also higher than the one obtained from the experiment. For the classic path and shifted path methods, the predicted and measured processing rate v_{pr} is in agreement. The improved laser systems and synchronization schemes can decrease the duty cycle, but it does not affect the principal limitations of the different LST methods.

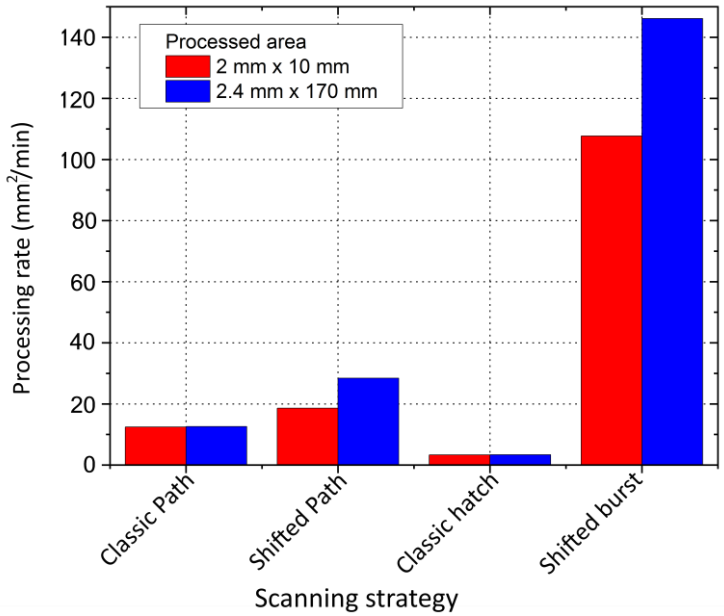

Fig. 5.2.8. Processing rates v_{pr} obtained for the different laser-texturing methods (scanning strategies) at their highest allowed scanning speeds and texture depth 6.5 µm. The data are based on measured processing time for two processed areas.

An explanation of the processing rates of the classic and shifted LST methods

A wider size of the processed area involves increasing the processing rate for both shifted methods. For the classic methods, there is almost no difference for the different size of the processed area. This result can be explained by the principal difference between these two strategies. For the classic path method, the explanation is clear: the texture is processed one object after the other (all circles in one dimple and then move to another dimple), so the full processing time of the whole textured area is roughly equal to the formation time of one object multiplied by the number of objects. A small decrease of the processing time of the classic methods can be achieved by correct setting of the laser scanning system used. In the classic methods, it is important to have fine-tuned the deflection mirrors' movement for the chosen scanning speed v_{sc} and minimal time delay for the laser synchronization with the scanner. For the shifted methods, the correct settings of the scanning system need to be tuned-up at the beginning of the scanning line only (one side of the processed area). Unlike this, for the classic hatch method synchronization will be done before each dimple in the LST array. This is the reason for the lowest processing rate v_{pr} for the classic hatch method independently of the scanned area size. This time dissipation at the beginning of each scanning path looks like the principal limitation for all classic methods with inertial scanning systems. This explanation is also supported by the trend of processing rate v_{pr} being in dependence on scanning speed v_{sc} (Fig. 5.2.9). The processing time has linear dependence on the scanning speed v_{sc} for the other three methods, but for the classic hatch method it has a certain limit and does not rise any more.

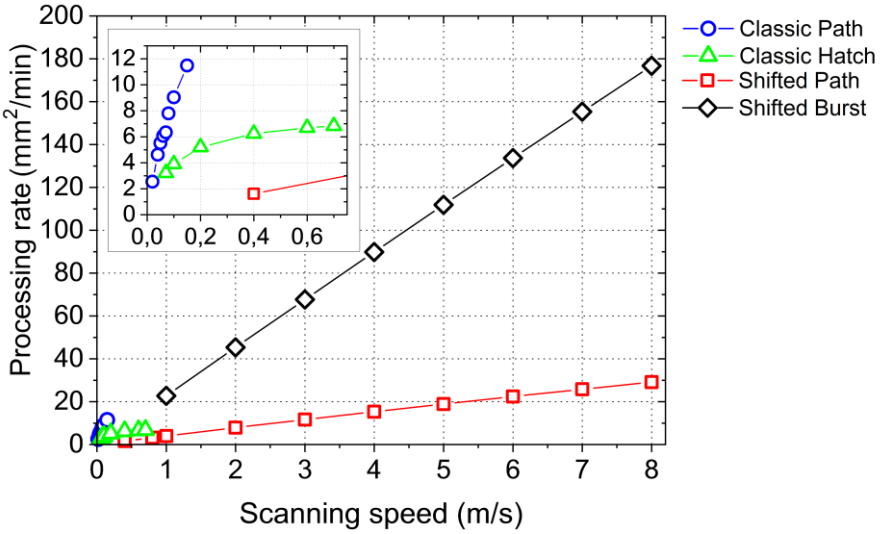

Fig. 5.2.9. Processing rate calculated for different laser scanning speeds and for different laser-texturing methods (scanning strategies). The data are based on processing time calculated by the scanning software for the processed area 2.4 x 170 mm^2.

The loss of time at the beginning of each line is also an explanation for the increase of the processing rate with the increase of the processing area length for the shifted method (in both variants). For the shifted path method, there are more scanning lines (one line – one pulse per object) in the process than for the shifted burst method (one line – burst of pulses per object), so the effect of area size becomes more important for the first method (52% in comparison to 36%). The dependence of the processing rate on area size for the shifted method can be a limiting factor for its application on small areas. Moreover, the shifted methods can be unusable for a small scanning area with a submillimeter perimeter.

Finally, the productivity of the scanning methods and their potential in the future were compared. The highest processing rate v_{pr} from the classic methods was experimentally observed for the classic path method (12.6 mm^2/min) and its increase is not permitted because it would result in a loss of precision. The only possible increase in this method would be by including hardware with a higher acceleration of the mirrors (e.g. electro-optical deflectors or acousto-optical deflectors [229]. The processing rate of the classic hatch method increases with the higher scanning speeds and accompanied by a loss of precision. Increase in this method would need an advance in synchronization (hardware and software) between the laser and the scanning head and elimination of the stopping of scanning between dimples. The presented shifted method solves/eliminates many of the mentioned problems (e.g. need of high acceleration, stopping between pulses). In comparison with the best result from the classic methods, the shifted path method has a 2.2 times higher processing rate, $v_{pr} = 28$ mm^2/min. The shifted burst strategy has a clear advantage in the processing rate value v_{pr}: more than 11.6 times higher than the best results of the classic LST.

The processing rates can be compared with the literature. Recently published results [237] using another promising method, DLIP, have shown a processing rate of 7 – 15 mm^2/min

for ferritic stainless steel and similar depth of texture (4 – 12 µm). The present here results of the processing rate are comparable or even higher better in the case of the shifted burst method.

From the software prediction, it can be seen that there is a linear dependence between processing rate v_{pr} and scanning speed v_{sc} for the shifted method, and the limitation related to scanning speed was not observed here. So if we assume continuation of the linear dependence and the use of a fast galvanometer scanning head with 50 m/s scanning speed (e.g. excelliSCAN), the processing rate v_{pr} would be 175 mm^2/min for the path variant and 912 mm^2/min for the burst variant. If we assume the use of a polygon scanning head with 1 km/s scanning speed and 71% time efficiency [312], the processing rate v_{pr} would be 2500 mm^2/min for the path variant and 12900 mm^2/min for the burst variant. The laser process would need a 5 MHz repetition frequency and 55 W average laser power in the path variant and a 143 MHz repetition frequency and 1570 W average laser power in the burst variant. Such a processing rate would be much closer to industrial applicability of laser surface texturing for functional applications and would enable the opening of new markets for this technology. Other improvements are possible using a combination of this method with other methods, like multibeam processing.

5.3. Thermo-physical processes in LST methods

5.3.1. Surface heat accumulation and plasma glow duration in micro-dimple LST

Heat accumulation in experiments with constant overlapping (with external trigger)

The results from precision and heat accumulation measurements in linear scanning were used IR radiation signal detection experiments on lateral LST with an array of microobjects. The applied LST methods of micro-dimple array formation have been described in section 4.3, and the corresponding speed limits were detected. In this section, the experimental results of LST with their maximal allowed speeds and constant overlapping are presented (triggered regime of laser pulse delivery, see Table 4.3).

The heat accumulation temperature IR radiation signal U_h has a tendency to increase with application of higher energy in the laser pulses (Fig. 5.3.1). The highest heat accumulation was detected in the classic hatch method. The heat accumulation value can be compared with energy delivered per scanned line unit, or simply line energy, which was applied for different LST methods [228]. The average power is reduced in the case of the laser pulse selection by the external trigger with the frequency $f_{trg} < f_{pulse}$ for keeping constant overlapping of 65% ($l_{trg} = r_d = const$). The line energy was maximal for the classic hatch LST method and it was equal to 14.3 J/m (Table 5.4). The real energy density can be higher due the mirrors' acceleration/deceleration on the edges of the laser beam path segments (see Figs. 4.3.1, *b* and 4.3.3, *a*).

The lowest heat accumulation temperature IR signal was detected at minimal pulse energy. For most of the LST methods the detected IR signal is low and it can be concluded that

the LST process falls in the non-overheated and low heat accumulation regime, when the IR signal is lower than 0.85 mV (compare with Table 5.1). The predicted heat accumulation temperature for the triggered surface processing was maximal for classic hatch LST and it was equal to 951 °C with 100 µJ. For the same pulse energy, the heat accumulation temperature 496 °C was predicted for the classic path method. The minimal predicted temperature was defined with the same energy in the laser pulse 100 µJ for the shifted burst method: 28 °C only. An interesting feature, is that the shifted path method has a slightly higher heat accumulation temperature of 55 °C, even with thousand times longest time period between laser pulses and energy 100 µJ (Table 4.3). For the lowest laser pulse energy 10 µJ, the heat accumulation temperature has an inverse character – it is maximal for the shifted burst regime and equal to 299 °C, whereas for the classic hatch LST, the predicted temperature is lower and equal 138 °C. This opposite character of the heat accumulation can be explained by the higher line energy and more than 10 times shorter pulse period for the shifted burst LST method. Such a prediction of the relative relation of the heat accumulation is in agreement with the experimentally detected residual IR signal U_h (see U_h value for 10 µJ and 100 µJ in Fig. 5.3.1).

Table 5.4. Line energy applied for the different LST methods with an external trigger.

Scanning strategy	Scanning speed v_{sc} (m/s)	Laser power P (W) at 10 µJ	Line energy Q_l at 10 µJ (J/m)	Laser power P (W) at 30 µJ	Line energy Q_l at 30 µJ (J/m)	Laser power P (W) at 100 µJ	Line energy Q_l at 100 µJ (J/m)
Classic path filling	0.15	0.21	1.4	0.63	4.2	2.1	14.0
Shifted path filling	8	0.4	0.1	1.2	0.2	4.0	0.5
Classic hatch	0.7	1	1.4	3	4.3	10	14.3
Shifted burst	8	10	1.5	13.6	1.7	13.8	1.7

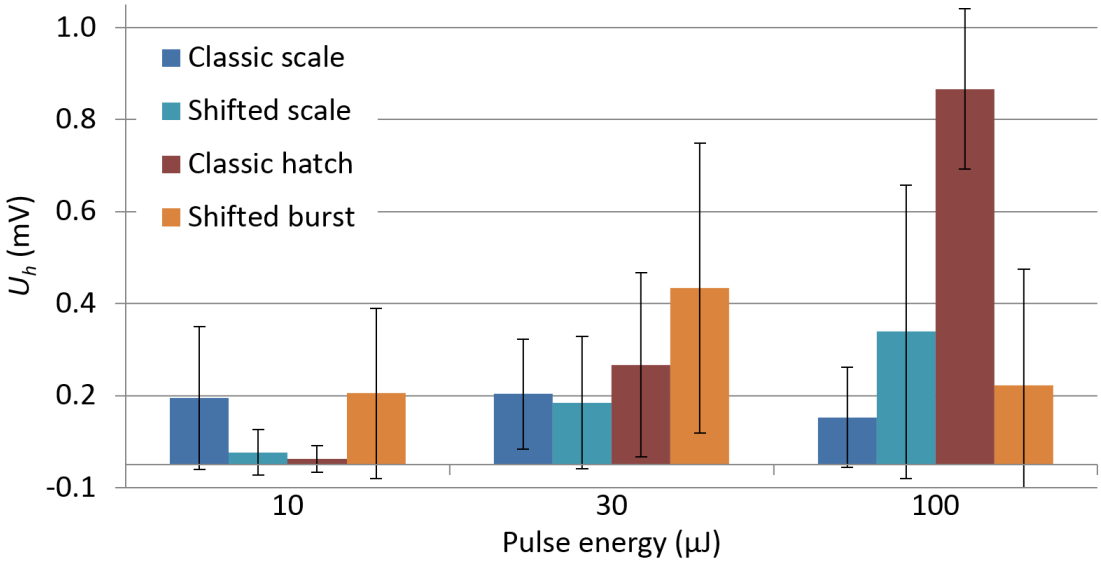

Fig. 5.3.1. The heat accumulation IR temperature signal detected on channel 1 from a stainless steel surface processed by different LST methods (triggered).

The measured peak thermal IR radiation signal U_{mb} achieves the maximal value in the classic path filling LST method with 100 μJ pulse energy (Fig. 5.3.2). A similar value of IR signal U_{mb} was detected with the classic hatch LST method with the same pulse energy. Both shifted methods have smaller or similar values of the maximal IR signal detected on channel 1. The detected maximal values are in agreement with results obtained in linear scanning experiments (compare with Fig. 5.1.2). The agreement of the detected maximal U_{mb} IR signal and low heat accumulation U_h value confirms that the LST methods have not reached the overheating regime.

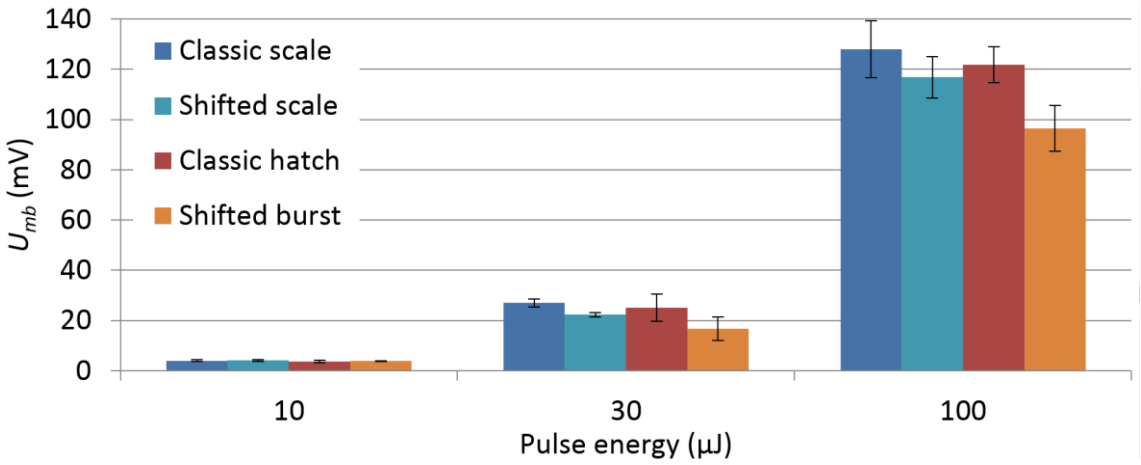

Fig. 5.3.2. The maximal IR temperature signals detected on channel 1 from a stainless steel surface processed by different LST methods (triggered).

Dependence of higher temperature NIR signals in applied LST methods (with external trigger)

The absence of long-term boiling or a liquid phase on the laser-scanned surfaces was confirmed by measurements of high temperature heat accumulation on channel 2 (Ch 2). The residual heat NIR signal had a small value comparable with the background noise level (Fig. 5.3.3). A similar result was obtained from the linear surface scanning (Fig. 5.1.3) and this means that the temperature between laser pulses is able to fall, under melting point, and every next laser pulse arrives on the solid material surface state.

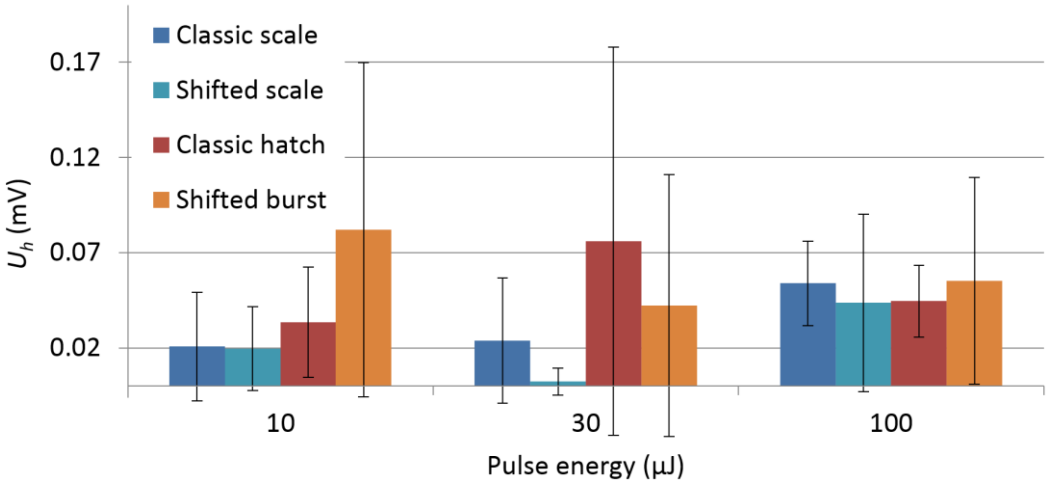

Fig. 5.3.3. The heat accumulation IR temperature signal detected on channel 2 from a stainless steel surface processed by different LST methods (triggered).

The maximal NIR temperature signals from channel 2 have shown that the surface temperature increase is similar for all the tested LST methods (Fig. 5.3.4). The resulting data are similar to the linear scanning experiments and this underlines the fact that there is no high temperature heat accumulation detected, even for localized beam movements in the classic path method.

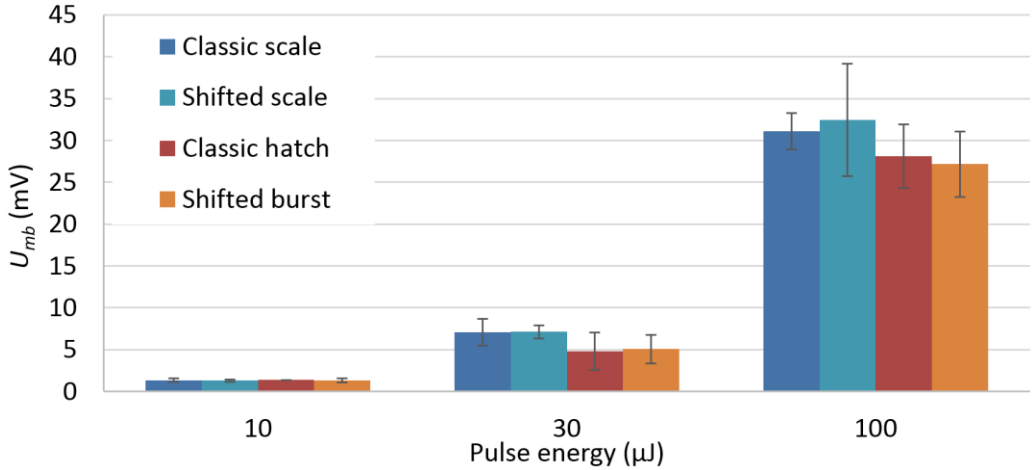

Fig. 5.3.4. The maximal IR temperature signals detected on channel 2 from a stainless steel surface processed by different LST methods (triggered).

Dependence of plasma glow duration for different LST methods (with external trigger)

The maximal plasma glow duration increases at the highest pulse energy for all tested LST methods (Fig. 5.3.5). This corresponds to the assumption of the dependence between plasma glow duration and the full energy of the ablation plume. Both classic methods have noteworthy higher values of the plasma glow duration at maximal laser pulse energy, but this difference is comparable to the SD level of the measurements. The maximal duration was not achieved in the case of the classic hatch LST method, where the detected heat accumulation signal U_h was maximal. This shows that heat accumulation is not the main factor which has an influence on the ablated plume full energy.

The LST with microobject formation has a shorter plasma glow duration in comparison with linear surface scanning measurements. This difference can be explained by the discrete character of surface scanning in the LST with microobjects. Instead of one overlapping distance along scanning direction r_d, the surface texturing with microobjects has an interline overlapping ΔH parameter additionally. Inside of the laser formed microobjects, the laser pulse interacts with the already affected surface from the neighboring line. The laser beam interaction with the partially scanned surface has other physical parameters of the ablation process, like the absorption coefficient or ablation threshold.

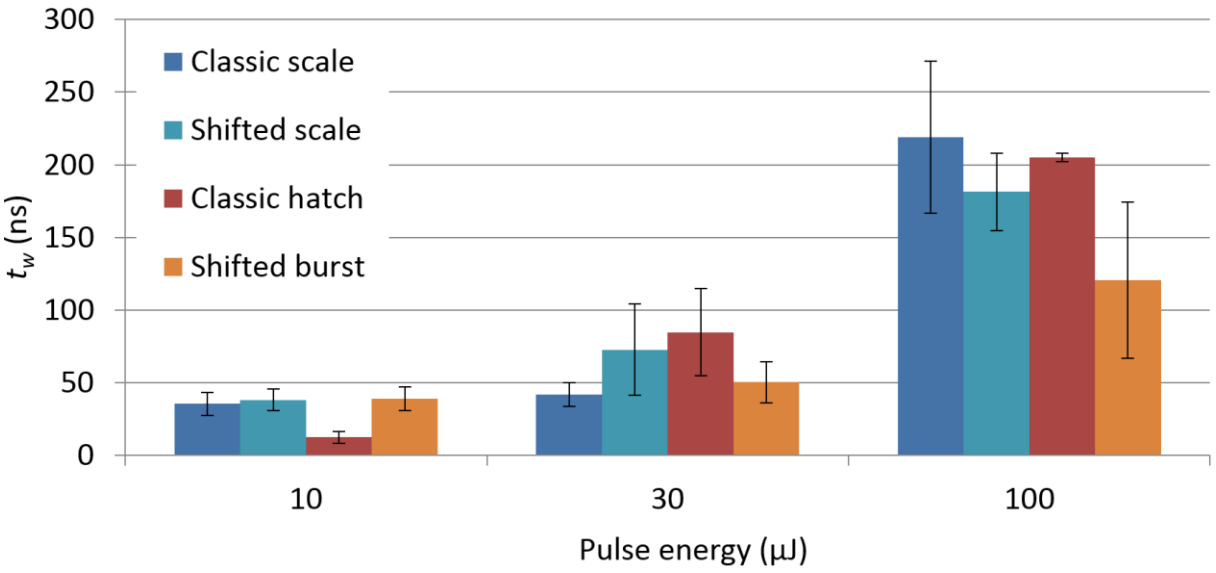

Fig. 5.3.5. The ablated plasma glow duration in dependence on the laser pulse energy in different LST methods (channel 3, triggered).

The application of an external trigger decreases the mean laser power. For example, in the application of the classic path filling method with 100 µJ, the laser pulse frequency will be 21 kHz with an external trigger and fixed spot distance 7 µm. The mean power of the laser in this case is equal 2.1 W only. In contrast, the application of the classic path filling without an external trigger has a frequency of laser pulses equal to 140 kHz and 13.8 W of laser pulses

(compare Table 4.3 with Table 4.4). Increasing the laser power should increase the heat accumulation in the textured surface. The next series of experiments were performed for detection of heat accumulation without an external trigger for the classic methods of surface processing.

Heat accumulation in experiments without constant overlapping (no external trigger in classic LST methods)

In the experiments without external trigger control, the heat accumulation IR radiation signal and plasma glow duration in the classic methods should be similar to those in linear scanning. The difference is only in the presence overlapping between scanning lines, in addition to inline laser spot overlapping. In both cases, the combination of the scanning speed > 0.07 m/s and laser pulse frequency was not enough to reach the overheated regime (see Table 5.1). A noticeable increase of the heat accumulation IR signal was detected for the classic path LST method with 10 μJ, in comparison with the triggering mode (Fig. 5.3.6, compare with Fig. 5.3.1). This can be explained by the nearly fifty times higher applied line energy of the classic path LST without a trigger, in comparison with triggered LST (Tables 5.4 and 5.5).

Table 5.5. Line energy applied for different LST methods without an external trigger.

Scanning strategy	Scanning speed v_{sc} (m/s)	Laser power P (W) at 10 μJ	Line energy Q_l (J/m) at 10 μJ	Laser power P (W) at 30 μJ	Line energy Q_l (J/m) at 30 μJ	Laser power P (W) at 100 μJ	Line energy Q_l (J/m) at 100 μJ
Classic path filling	0.15	10	66.7	13.6	90.7	13.8	92.0
Shifted path filling	8	0.4	0.1	1.2	0.2	4.0	0.5
Classic hatch	0.7	10	14.3	13.6	19.4	13.8	19.7
Shifted burst	8	10	1.3	13.6	1.7	13.8	1.7

The maximal heat accumulation temperature of LST was predicted for the classic path method: 1949 °C, with the laser pulse energy 30 µJ. For the laser pulse energy 100 µJ, the predicted heat accumulation temperature is equal to 1910 °C. The classic hatch method has the maximal predicted heat accumulation temperature of 1172 °C. This temperature is closer to the melting point in comparison to the triggered method with laser pulse energy 100 µJ. The unexpected lower value of the heat accumulation IR signal U_h can be explained by the change of surface emissivity inside the laser beam hatched dimples in comparison with the single-line scanning. Another possible reason for the residual heat signal decreasing can be explained by the shorter time between laser pulses. The shorter interval between laser pulses leads to an increase of the ablation cloud shielding effects, with lower laser pulse affection of the scanned surface. The highest heat accumulation IR radiation signal, $U_h = 0.57$ mV, was detected in the application of the classic path filling method, even when the other methods have the same power (Table 4.4). This fact underlines the greater influence of the line energy on the heat accumulation rather than the applied power of the laser source (Table 5.5).

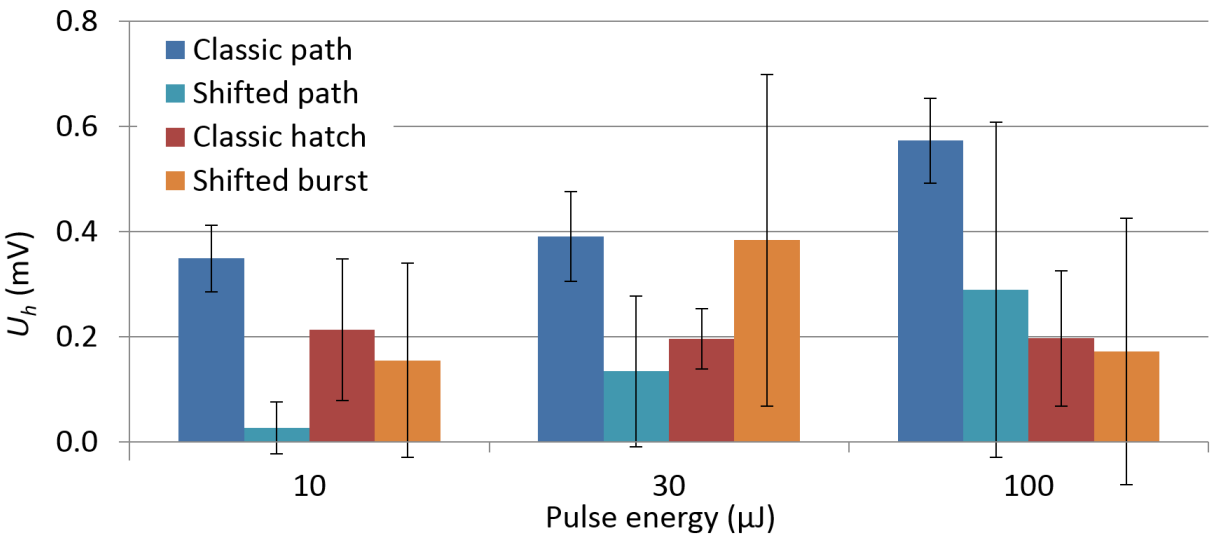

Fig. 5.3.6. The heat accumulation IR temperature signal detected on channel 1 from a stainless steel surface processed by different LST methods (without a trigger for the classic LST methods).

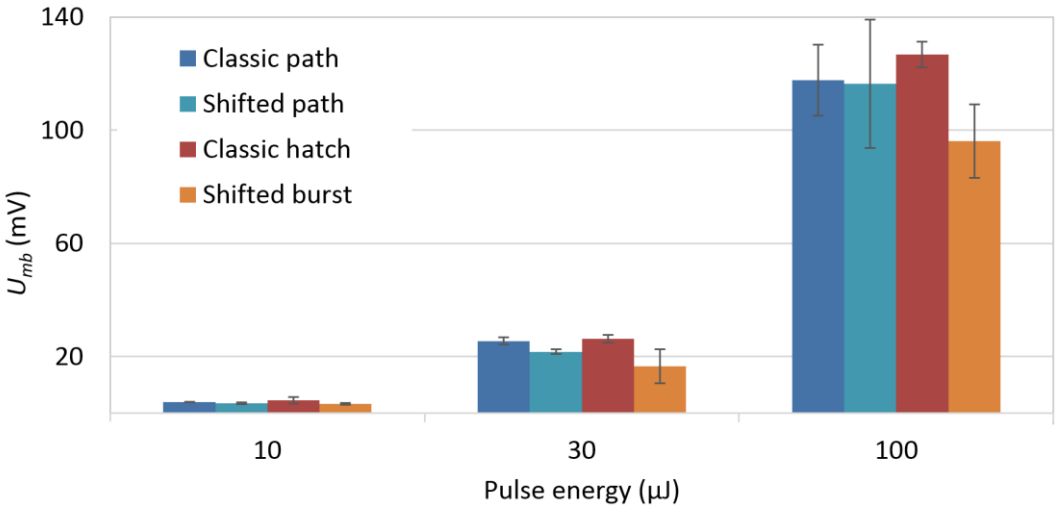

Fig. 5.3.7. The maximal IR temperature signal detected on channel 1 from a stainless steel surface processed by different LST methods (without a trigger for the classic LST methods).

The detection of the maximal heat peak signal on channel 1 shows that the achieved maximal temperature in the processed area has similar values for both classic and shifted LST methods (Fig. 5.3.7). The values of the detected signal $U_{mb} \leq 130$ mV corresponded to the IR radiation signal detected in the straight-line scanning experiments (see Fig. 5.1.2).

Dependence of high temperature NIR signals in applied LST methods (no external trigger in classic LST methods)

The NIR signal, which was detected on the second channel without triggering of the laser pulses, shows results similar to those of the triggered regime. There is no high-temperature heat accumulation and the value U_h did not increase above 0.1 mV (compare to Fig. 5.3.3). The same holds true for the maximal detected IR signal on the second channel U_{mb}. The maximal detected value U_{mb} did not exceed 40 mV (compare to Fig. 5.3.4).

Dependence of plasma glow duration for different LST methods (no external trigger in classic LST methods)

The ablated plasma glow signal falls in the same range of duration time as detected in the LST without triggering of the laser pulses (Fig. 5.3.8). For the lowest pulse energy 10 µJ, the plasma glow duration t_w becomes longer in comparison to the classic LST with an external trigger. At the middle pulse energy 30 µJ, the plasma glow duration becomes shorter for the classic path and longer for the classic hatch LST methods. At the maximal laser pulse energy 100 µJ, the value t_w becomes shorter for both classic LST methods without an external trigger. The difference in the plasma glow duration for these two regimes can be explained by the deviation in the measurements or by stronger shielding effects in multiline surface processing.

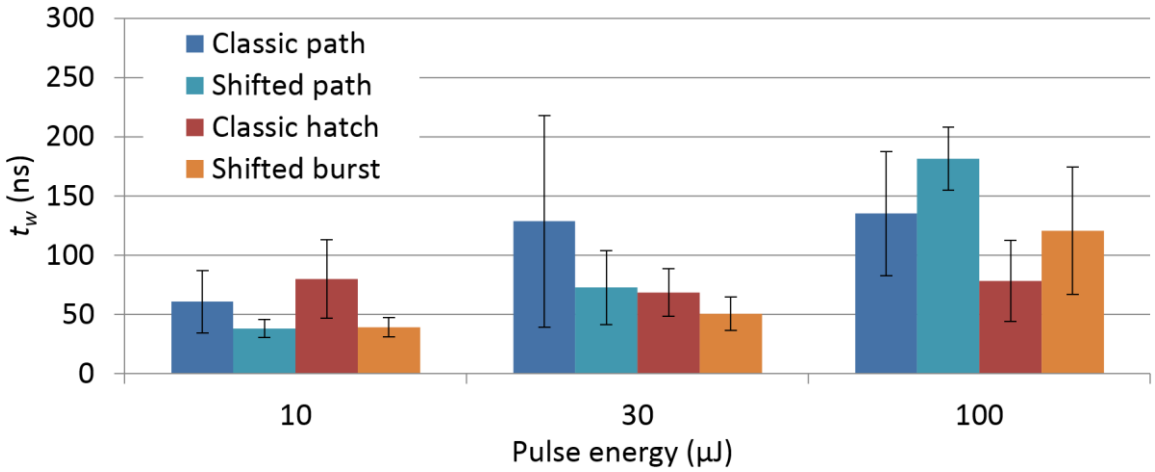

Fig. 5.3.8. The ablated plasma glow duration in dependence on laser pulse energy in the different LST methods (channel 3, without trigger for the classic LST methods).

As a summary of this section, the main results can be pointed out. The shifted and the classic LST methods achieved a similar maximal temperature in the surface processing with ultrashort laser pulses. For all the analyzed LST strategies, the heat accumulation signal has a similar value to the same energy of the laser pulses and the overheated regime was not achieved. However, two benefits from application of the shifted methods should be underlined here. The shifted LST methods have more than ten times higher scanning speed and, as a result, more than ten times higher processing rate. The heat accumulation in the shifted LST methods lies under the critical boundary 607 °C even when the laser pulse frequency has exceeded 1 MHz.

5.3.2. Subsurface temperature gradients in the LST methods

The intensity and efficiency of the laser material ablation depends on the state of the processed surface. For example, a surface with higher roughness has higher absorptivity. In a similar way, the ablation depth and material removal speed can be affected by the inherit temperature state of the laser-scanned surface. The laser material processing with ultrashort laser pulses initiates extreme high temperature gradients in subsurface layers. Application of the different scanning speeds and laser frequencies is able to noticeably change the heat accumulation distribution in the subsurface layers. The difference of the surface temperature state between laser pulses in a sequence affects the efficiency and quality of ultrashort laser surface processing [313]. After the laser surface ablation is finished, the upper surface layer of the material is in the preheated state with a higher temperature in comparison with deeper subsurface layers. The temperature gradient in the subsurface material layers, under the laser beam scanned surface, is able to express the difference in the ablation threshold for the upper and lower layers. The different thermo-physical states of the upper and lower layers affects the ablated depth and process quality of the output surface.

The model of heat accumulation under a scanning laser beam described in section 4.6.4 is able to predict the temperature distribution in the material subsurface layers.

Eq. 4.18 - 19 includes the depth parameter z and it gives the possibility to observe temperature changes in subsurface layers in the different time moments. In this work, the depth distribution of the temperature fields under the laser-scanning beam was evaluated for stainless steel for two LST methods. Heat accumulation was defined for the burst and classic sLST methods for several points fixed in equidistant subsurface layers down to 5 µm depth. Calculations were done for the speed of 0.7 m/s for the classic hatch method and 8 m/s for the shifted burst LST method. The inline spot distance 7 µm at this speed corresponds to 10 µs and a delay 0.85 µs between laser pulses for the classic hatch and shifted burst LST methods, respectively (see Table 4.3). The evolution of the temperature fields under these scanning regimes is presented in Fig. 5.3.9 (dashed straight line corresponds to maximal heat accumulation on the scanned surface, the full laser pulse energy $Q_p = 11$ µJ).

The values in the colors mean depths under the fixed surface point. Since the laser beam is scanned on the surface across this fixed point, the temperature increases at the start and then, after a direct hit, slowly decreases, longer than 150 µs for the classic hatch and 15 µs for the shifted burst LST methods. The maximal predicted heat accumulation surface temperature for the classic method is low, about 100 K only. The depth temperature gradient is not higher than 1 K/µm and the temperature is nearly the same for all subsurface layers to the 5 µm depth. The shifted burst LST method has the maximal heat accumulation value of $\Delta T_{Sum}(4.25\ \mu s, 0\ \mu m) \approx 350$ K on the top surface ($z = 0$ µm). Nearly the same value of heat accumulation is obtained for the next subsurface point ($z = 1$ µm) $\Delta T_{Sum}(4.27\ \mu s, 1\ \mu m) \approx 330$ K. The temperature gradient at the moment of achieving the maximal surface heat accumulation $t = 4.25$ µm is about 20 K/µm. At the same moment, the subsurface temperature for the deeper layers is noticeably lower, $\Delta T_{Sum}(4.25\ \mu s, z \geq 2\ \mu m) \leq 270$ K. This means that the temperature gradient between upper layers with depth $z \leq 1$ µm and deeper subsurface layers $z \geq 2$ µm is more than 60 K/µm.

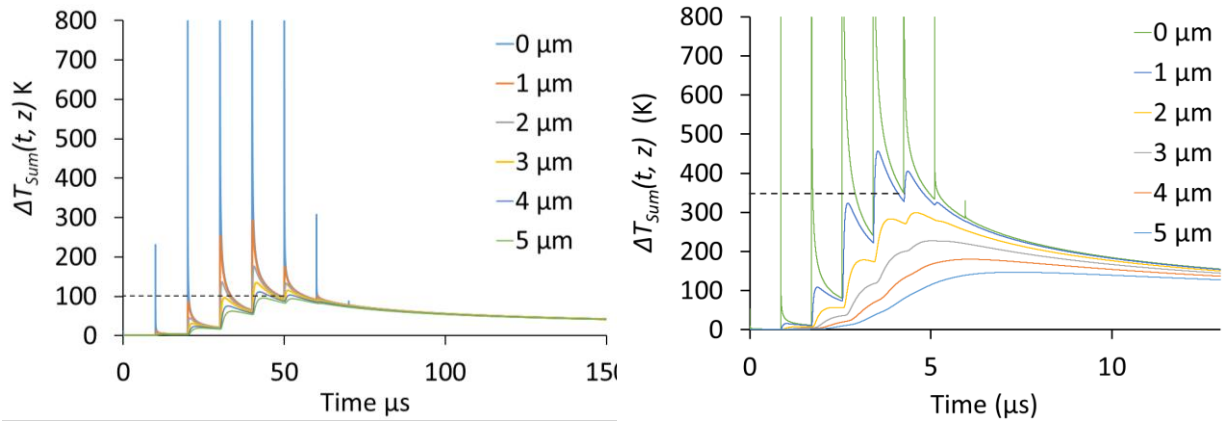

a *b*

Fig. 5.3.9. Temperature changes on the surface and in subsurface layers of stainless steel in the fixed point under the laser-scanning beam: *a*) classic method ($v_{sc} = 0.7$ m/s, $f_{pulse} = 100$ kHz); *b*) shifted burst sLST method ($v_{sc} = 8$ m/s, $f_{pulse} = 1143$ kHz) [314].

The difference in the temperature state of the thin surface layer and deeper subsurface layers under the scanning laser beam can be the reason for the lower roughness of the laser-processed surface with higher heat accumulation. The measured dimple bottom

roughness which was processed by the shifted burst LST method was $R_a = 0.03 \div 0.06$ µm. The same structure formed by the classic hatch LST method with lower heat accumulation has roughness $R_a = 0.134 \div 0.241$ µm. The lower roughness of the laser-processed surface with higher temperature on top and contrasting lower subsurface temperatures can be explained by the specific state of the scanned surface. Heat accumulation of $380 \div 360$ K in the upper layers corresponds to a temperature region where the tensile strength of AISI 304 becomes lower (Appendix B) [284]. This preheating regime of laser material processing leads to softening of the upper layer of the sample material. The ablation processes, like spallation and phase explosion, will be more preferred in these thin pre-heated surface layers and less preferred for the deeper and cooler layers with higher strength. The accentuated temperature gradient between upper and deeper surface layers leads to smoother laser material removal, and this can be described as soft exfoliation of the upper layers by laser ablation. This temperature field is achieved in the burst regime and is presented as an optimal condition with positive heat accumulation. The positive heat accumulation in these experiments has not led to the higher efficiency of ablation processes, but gives lower roughness of the output surface.

5.4. Application of the developed LST methods for preparation of functional surfaces

5.4.1. Formation of functional surfaces for real applications

In this section, several real applications of the shifted LST methods are presented. The first example of a shifted LST application is the laser formation of hydrophobic surfaces. The square columns on an aluminium alloy Al2017 substrate were created by a cross linear raster with 5 µm length of the shifting vectors. The cubic structure on the aluminium surface is able to increase the contact angle more than 130° and up to superhydrophobic angles $\theta_m > 150°$ [26] (Fig. 5.4.1). The hydrophobic LST surfaces were represented as a special pattern for molding forms. The main goal is to decrease the normal force in order to easily remove the molded object and at the same time increase the tangential forces to avoid self-debonding.

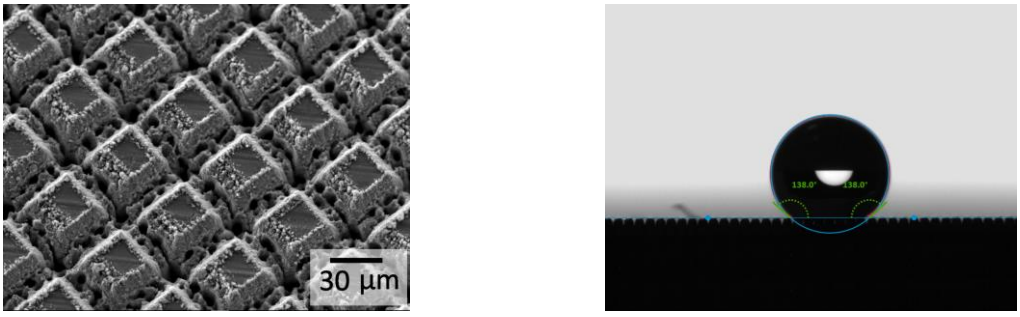

a *b*

Fig. 5.4.1. Formation of a hydrophobic structure on aluminium alloy: *a*) SEM image of a hydrophobic peak structure; *b*) optical image of wettability a test of the textured aluminium alloy surface [275]

Another example of shifted LST application is the formation of thermal spray substrates. The formation of the surface structures should increase the bonding forces

between the substrate and thermal-sprayed layer. Unlike with the traditional blast sanding, the LST method is able to create an optimal surface structure without cracks. Fig. 5.4.2 presents surfaces of tungsten and Al_2O_3 after application of the shifted LST method for the thermal spray coating. The wide spectrum of topography parameters can be easily improved to the desired structure by changing the laser-scanning parameters – periodicity, depth, inner structure of the bottom, concave or convex curvature.

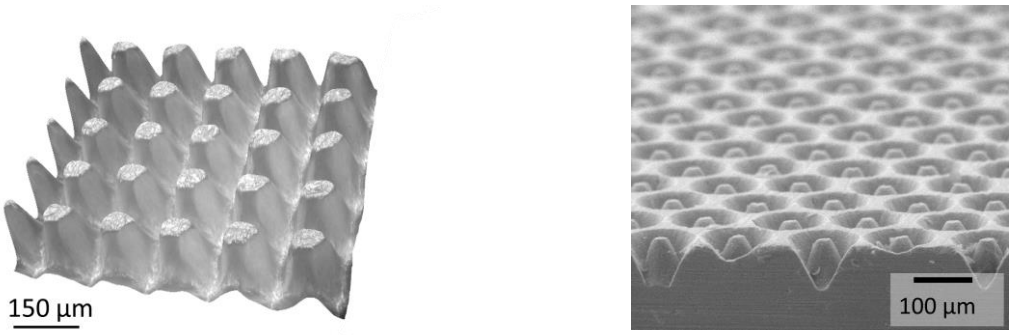

a *b*

Fig. 5.4.2. Functional surfaces formed by shifted LST for improving thermal-sprayed layer adhesion: *a*) 3D optical microscopy of the column structure on a tungsten surface formed by shifted LST in the burst regime (textured for *Institute of Plasma Physics, CAS, Prague*) [315]; *b*) SEM image of toroidal structures on Al_2O_3 formed by shifted path filling LST (textured for *LERMPS-UTBM*, *France*).

It should be underlined that formation of the convex structures is an untypical task for classic methods of LST. The formation of such structures in the literature are described as the application of laser beam interference and other optical effects in combination with self-organization of laser-ablated material [27], [242], [258], [316]–[318]. The geometry of the microobjects in such LST methods is limited by physical principles of the applied laser-processing technique. The shifted method of LST gives the possibility to control directly the geometry and distribution of the microobjects. The diameter, form and periodicity of the columns can be defined by shifted vectors, raster period, scanning speed and laser pulse frequency. The formation of convex microstructures, like a column array on the laser-textured surface, leads to increasing the contact area. For example, for a chemical application the laser-textured surface needed to have shallow depth structure of $10 \div 15$ μm for complete covering by a thin chemical coating. The period of the structure was set equal to 50 μm; the diameter of the textured microobjects was 30 μm. Such a structure was created by the shifted LST method and it has no gaps or holes in the crossing points of the rows (Fig. 5.4.3, *a*). The similar dimple and column structures were created for distancing the bottom surface from the upper contact surface of a tool. In this way, the wear resistance of the surface can be increased by application of LST on complex 3D technical tools (Fig. 5.4.3, *b*).

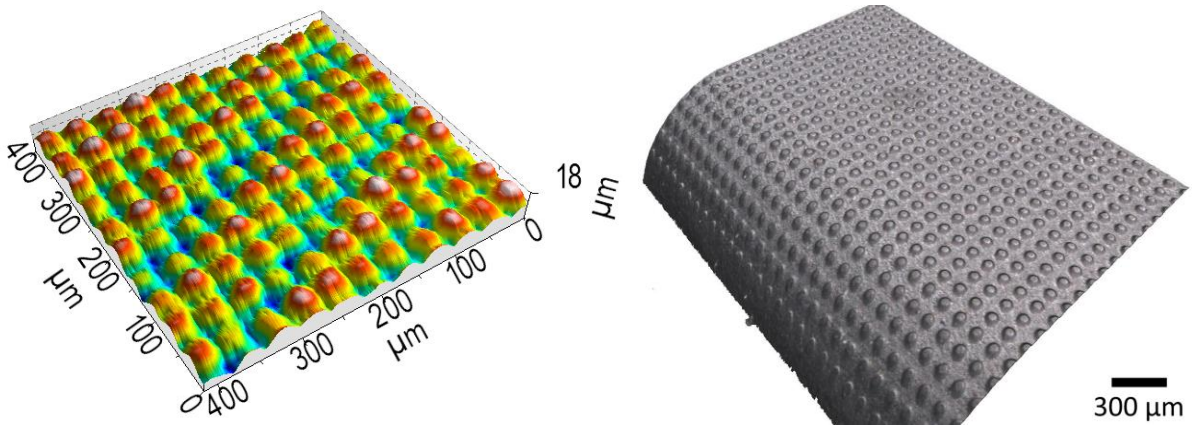

a *b*

Fig. 5.4.3. Formation of column structures for different applications: *a*) substrate for a chemical covering application; *b*) bonding structure for improving surface wear resistance.

Laser machining of sliding bearings is among the most cited applications of LST. The same application is used for the shifted path filling LST method on ring and half-bearing surfaces Fig 5.4.4. In one of our experiment, the surface relief was formed by raster scanning across the bearing sliding direction. The distance between the laser-textured micro-dimples was set at 78 µm, the depth varied between 6.5 ÷ 7 µm and the texture area density was 12%. The tribological experiments show that bearings with a laser-textured surface have smaller torque momentum. The lower measured torque in the initial stages of the star-stop test could be explained by faster oil film formation during rotation running [292].

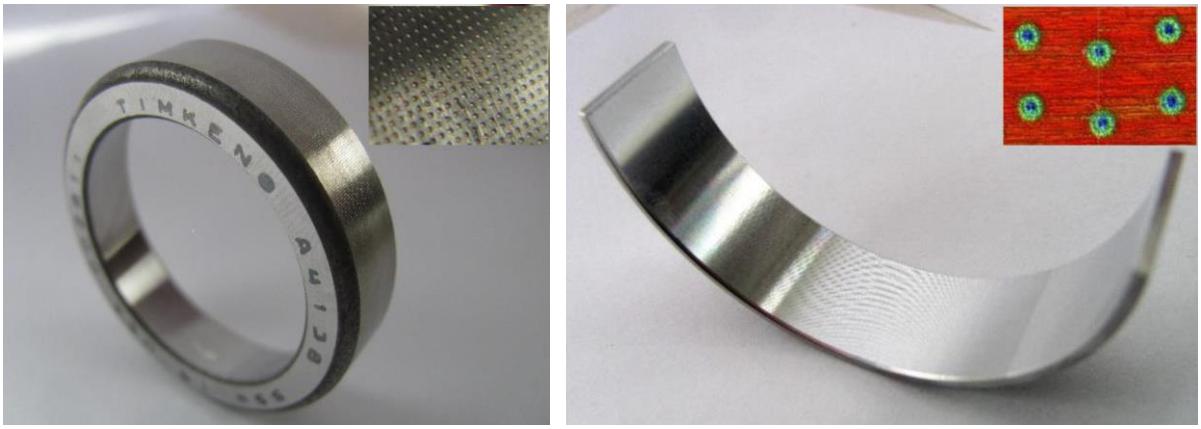

a *b*

Fig 5.4.4. Application of the shifted LST method for sliding bearings: *a*) laser-textured Timken A4138 bearing ring; *b*) bi-metal textured half bearing [292] (in the top-right corner is the zoomed texture).

There are several other functional surfaces which were textured by the shifted LST method in our laboratory. These functional surfaces were formed for biology, thermal and

semiconductor applications. At present, they are under testing for better understanding of the relief-sensitive physical processes which take place in the laser-formed surface layers.

5.4.2. Processing rate comparison of shifted and classic LST methods

An application of the shifted LST method was compared with surface texturing using the classic scanning method in an independent laboratory. The classic LST was provided on a commercial proposed five-axis computer numerical control (CNC) machine. For both LST methods, the parameters of the applied laser source and optical path system were the same. On stainless steel and tungsten surfaces, an array of micro-columns was formed on an area of 5 mm × 10 mm. In both cases, the column structure has a similar geometry (Fig. 5.4.5). The goal height of the micro-column structure was set at 80 µm, with the distance between micro-columns about 70 µm. The structure is formed by sequential ablation of material around the micro-column peaks.

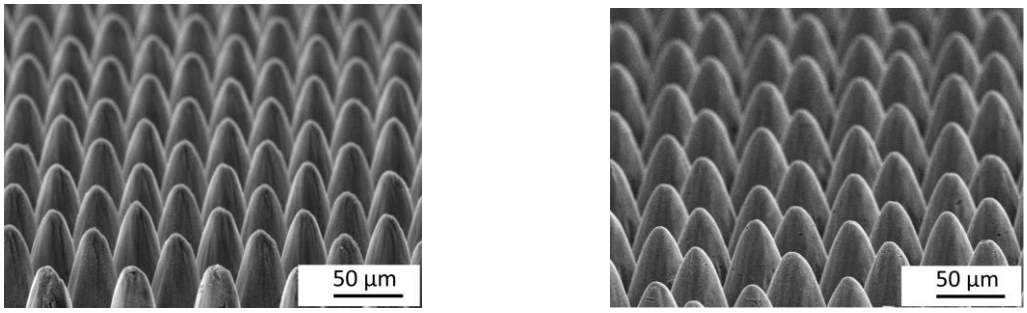

a *b*

Fig. 5.4.5. SEM images of the lateral array of micro-columns formed by different scanning methods *a*) classic LST method; *b*) shifted burst LST method.

The processing time which was achieved with the classic method is more than five times longer in comparison with the shifted method for creating the same texture. The explanation of such a difference in the processing time is not only in the physical principle of the laser pulse distribution, but in the noticeably higher number of synchronization cycles. Every next instruction in the command list for the galvanometer scanner slows the scanning speed and the average laser power becomes lower with the increase in the number of duty cycles.

A similar difference in the processing rates was detected in experiments with formation of a dimple array. The area of the dimple array was the same as for columns, but subsequent material ablation occurs inside of the dimples, leaving the material around the dimples. The distance between dimples was set at 250 µm and the depth of the dimples was around 80 µm. In Table 5.6, the processing rates achieved by the classic methods in the independent tests and shifted methods from our laboratory are presented. It is necessary to underline that the maximal technical scanning speed limit was the same 8 m/s for both sets of galvanometer scanner equipment.

Table 5.6. Processing rates achieved by the shifted method and the classic method of LST on a tungsten surface with structured area 5 mm × 10 mm.

Method	Texture type	Processing time	Data transport time	Data value	Processing rate v_{pr} (mm^2/min)
Shifted Burst	Columns	18.2 min	< 1 sec	4 kB	2.8
Shifted Burst	Dimples	17.5 min	< 1 sec	13.7 kB	2.9
Classic	Columns	105.0 min	< 1 min	15 MB	0.5
Classic	Dimples	70.1 min	1.2 min	46.7 MB	0.7

The processing rate value of shifted and classic methods decreased with the required depth of the structure, 80 µm, by multilayer scanning up to a thousand times. The multilayer manner of depth profiling for achieving the desired structure decreases the processing rate. Although the processing rate of the shifted burst LST method is more than five times higher than in the classic method, the achieved value of 2.8 mm^2/min can be improved. In the previous section, it was noted that there are several ways to increase the processing rate with application of the shifted LST methods. This can be achieved by higher scanning speeds – up to thousands of meters per second, higher pulse energy, ablation in the burst regime with GHz and THz frequency, the multi-beam technique of surface scanning or their combinations.

5.5. Summary of the main results

In this section, the experimental results of laser surface processing with ultrashort pulse laser scanning methods are discussed in comparison with analytical predictions. Three regimes of heat accumulation for laser surface processing were identified: overheating, critical heat accumulation and low heat accumulation. The analytical model predicted a temperature increase up to boiling point, and this regime was labeled as overheated laser surface processing. This overheated regime was detected as an extensive IR radiation signal increase in the scanning speed region of 0.007 ÷ 0.03 m/s. The scanning speed region from 0.03 m/s to 3 m/s is described as a critical heat accumulation regime, and it corresponds to the predicted residual surface temperature higher than 607 °C. The low heat accumulation regime was observed for speeds from 3 m/s to 8 m/s.

The plasma glow duration was analyzed in dependence on the laser surface scanning speed. An ablated plasma glow duration as long as ~ 200 ns was observed for the lowest scanning speeds, where the heat accumulation is maximal. At the higher scanning speeds, the plasma glow duration drops to ≤ 100 ns. Two possible mechanisms of this dependence were discussed. The first one is the higher energy of the laser-ablated plume from the preheated state of the processed metal surface. And the second one is the higher density of ablated products in the nearest to the previous laser spot area (particles, ions and vapors). It was mentioned that a deeper understanding of the physical reason for the longer plasma glow duration at lower speeds needs the application of faster radiation detectors in combination with spectral analysis.

The laser surface lateral texturing was analyzed in applications of the different LST methods. The maximal scanning speeds for acceptable precision of 5% in the formation of a circular dimple array were defined. The established speed limits are: 0.15 m/s for the classic path, 8 m/s for the shifted path, 0.7 m/s for the classic hatch and 8 m/s for the shifted burst methods. The precision of the dimple depth profiles of the laser formation was analyzed. The shifted burst LST method achieved maximal precision with the fastest processing rate. The maximal lateral processing rate was found in the shifted LST method: 160 cm^2/min for one scan layer and 146 mm^2/min for multilayer surface texturing with the depth of microobjects at 6.5 μm. For comparison, the maximal processing rate in the classic LST method was 6.49 cm^2/min for one scan layer and 12.6 mm^2/min for multilayer scanning to the depth of 6.5 μm.

The heat accumulation and ablation plasma glow duration were analyzed for the classic and shifted LST methods. For both types of laser surface scanning, it was shown that the overheated regime does not appear. For the shifted LST methods, the predicted heat accumulation temperature did not achieve the critical value of 607 °C and the measured IR residual heat signal was $U_h < 0.65\ \mathrm{mV}$. This result is in accordance with detection of surface heat regimes at different scanning speeds. The detection of the maximal residual IR radiation signal for classic methods was explained by the increased line energy in the scanning process with lower scanning speeds. For both the classic and shifted methods, the heat accumulation IR signal remains under $U_h < 0.9\ \mathrm{mV}$ and this shows that the overheated regime of laser surface processing was not achieved.

At the end, several applications of the developed shifted LST methods were presented. The processing rate of a practical application of the shifted LST method was also compared with the application of a classic LST method in an independent laboratory. The shifted LST method shows a five times faster processing rate for formation of a 50 mm^2 columns surface texture.

One of the special features of the shifted LST method with equidistant distribution of the laser pulses is the uncommonly long interval between laser pulses on a local position – it is about one thousand times longer than in other methods (see Table 4.3). Such a long interval between laser pulses does not slow down the scanning speed, but, on the contrary, the higher speed is desirable for stable beam movement and higher frequencies. The millisecond range of the laser pulse interval makes the shifted scanning strategy a promising method for applications where heat accumulation should be avoided: the processing of biomaterials, 3D printing, microelectronics, microscale thermography or laser NDT methods.

6. Conclusion

This dissertation is devoted to the characterization of thermo-physical processes in ultrashort pulse laser surface texturing (LST) and the development of laser scanning methods for high-speed processing with high precision and low heat accumulation. The different types of LST and their applications are reviewed in the first part of the dissertation. It was shown that the precision and effectivity of the scanning beam laser surface processing depend not only on parameters of the laser pulses, but also on the correct choice of the scanning speed and the strategy of the laser beam movement. The high-speed surface scanning leads to a decrease in precision, but low-speed scanning involves unusual heat accumulation in the laser processed material.

In this research, the heat accumulation and plasma glow duration from a laser-processed surface were measured with fast IR and NIR detectors. The main benefit of the IR radiation detection is that it is a highly sensitive and noncontact direct measurement of temperature changes. The thermo-physical processes of the laser surface scanning were evaluated in terms of the achieved level of the heat accumulation. The heat accumulation was detected as a residual IR radiation signal emitted from a laser-scanned surface between neighboring laser pulses. The influence of laser pulse energy on the heat accumulation was analyzed in a wide range of scanning speeds. The material temperature changes were predicted by a semi-planar model of laser surface scanning and then were compared with experimentally detected IR radiation signals. Three regimes of laser surface processing were defined: overheated laser surface processing with a quick increase in the residual temperature and predicted temperature exceeding the evaporation point; laser surface processing with critical heat accumulation ($T_s > T_{th}$); and the low heat accumulation regime ($T_s < T_{th}$).

Analysis of the plasma glow duration has shown that application of higher scanning speeds leads to a decrease in plasma glow duration. Two possible mechanisms of the plasma glow duration dependence on the laser surface scanning speed were discussed. One explanation is based on the additional energy of the plasma plume acquired from the heat accumulation in the laser-scanned surface layer at low speed. Another possible reason for the longer plasma plume glow duration is the presence of the inherited particles and partially ionized vapor after the previous laser pulse ablation. The interaction of the laser pulse with a surface covered by a vapor-particle layer can decrease the ablation threshold and then the ablated plasma glow contains a larger amount of energy. It was noted that a deeper investigation of the plasma plume evolution in conditions of laser multi-pulse surface scanning needs a combination of fast IR measurements with high-speed spectral analysis.

In this dissertation, a newly developed shifted LST method is described in detail. The shifted surface texturing is performed with sequential application of equidistant laser pulses in a linear raster. Sequential application of the linear rasters on the shifted positions along geometrical primitives (circles, triangles, squares, etc.) leads to forming an array of microobjects. The asynchronous manner of laser pulse delivery leads to achieving a high processing rate in the shifted LST methods at maximal possible scanning speed with the galvanometer scanner.

The precision, thermal regimes, speed limitations and processing rates of the shifted scanning methods were compared with two corresponding classic LST methods. The shifted methods show a higher processing rate in applications with a dimple array formation. The shifted LST method in burst regime has a processing rate more than 11 times faster in comparison with classic LST methods. The precision deviation of the shifted LST methods remains lower than 5% at the maximal hardware-limited scanning speed. The upper speed limitation of the classic methods is slower than one meter per second only.

The IR radiation measurements for all tested LST methods have shown that the heat accumulation does not reach the overheated regime of laser surface processing. In the shifted LST methods, the heat accumulation temperature is lower than the critical value in whole range of the tested energies of the laser pulse. For the classic methods, the maximal heat accumulation was detected for the classic path filing method in the triggered regime (controlled laser pulse overlapping). In the regime without application of the external trigger, the maximal heat accumulation was detected for the classic hatch filling. The detected heat accumulation corresponds to the maximal applied line energy on the scanned surface for these two regimes of laser pulse generation. The corresponding analytical calculations are in accordance with this result. The predicted temperatures of the heat accumulation in the classic LST methods exceeded the melting point and this corresponds to the overheated regime of material processing.

The analytical model was applied for a thermo-physical explanation of the difference in the output surface quality for the classic hatch and shifted burst LST methods. The stronger temperature gradients at higher scanning speeds were offered as an optimal regime with positive heat accumulation, when the output surface has lower roughness. This regime of high-speed surface processing was explained by laser-stimulated differentiation of thermo-physical properties between the upper and lower surface layers of laser-scanned material.

The developed shifted LST methods were applied for the surface functionalization of different types of materials. One application of the shifted LST method the formation of periodical structures on metallic and ceramic substrates for thermal spray coatings. Similar structures were created for improving the wear resistance of an industrial tool with a large working area. The array of micro-dimple structures was formed on the sliding surface of a bearing and the results of tribological tests were presented. It was found that the laser-textured bearing surface has decreased torque momentum.

The processing rate achieved in surface functionalization using the shifted LST method was compared with the application of a classic LST method in an independent laboratory. The application of the shifted LST method shows a more than five times higher processing rate for creating the same column structure.

The described method of IR radiation signal detection will be used for analysis of thermo-physical processes in applications with other types of lasers. In particular, measurements will be provided for microsecond, nanosecond and femtosecond laser pulses. Additional improvement of the heat accumulation detection and plasma glow analysis can be done with high-speed spectral recording of the IR radiation and the application of other types of

photodiodes. The analytical model can be extended by an integration algorithm of IR signal analysis from a larger area of the laser-processed surface. The next step in the evolution of this IR radiation signal analysis of the thermo-physical processes can be a combination of laser beam holographical modulation and high density spectrometry.

The developed shifted LST method can be used in other applications, where precision and higher scanning speed are principal factors of laser surface processing. Especially, the shifted LST can be useful in applications with equidistant laser pulse distribution in the possible low heat accumulation regime. For example, in biomedicine or selective laser melting technology. The shifted method can be useful for decreasing of lateral macroscale thermo-mechanical gradients and noticeably increasing the speed for the filling grades formation in 3D laser printing. Application of the shifted LST method with the high-speed IR detectors and spatial light modulation opens new perspectives for high-speed laser microscale thermography. Further combination of the shifted LST method with multi-beam surface scanning will be able to increase the processing rates up to ten times.

7. References

[1] K. Sugioka. *Progress in ultrafast laser processing and future prospects*, Nanophotonics, vol. 6, no. 2, pp. 393–413, Jan. 2017.

[2] P. Šugár, J. Šugárová, and M. Frnčík. *Laser surface texturing of tool steel: textured surfaces quality evaluation*, Open Eng., vol. 6, no. 1, pp. 90–97, May 2016.

[3] A. Žemaitis, M. Gaidys, M. Brikas, P. Gečys, G. Račiukaitis, and M. Gedvilas. *Advanced laser scanning for highly-efficient ablation and ultrafast surface structuring: experiment and model*, Sci. Rep., vol. 8, no. 1, p. 17376, Dec. 2018.

[4] M. Jiang, H. Y. Xiao, S. M. Peng, G. X. Yang, Z. J. Liu, and X. T. Zu. *A comparative study of low energy radiation response of AlAs, GaAs and GaAs/AlAs superlattice and the damage effects on their electronic structures*, Sci. Rep., vol. 8, no. 1, p. 2012, Dec. 2018.

[5] F. He, Y. Liao, J. Lin, J. Song, L. Qiao, Y. Cheng, and K. Sugioka. *Femtosecond Laser Fabrication of Monolithically Integrated Microfluidic Sensors in Glass*, pp. 19402–19440, 2014.

[6] T. Yang, H. Lin, and B. Jia. *Two-dimensional material functional devices enabled by direct laser fabrication*, Front. Optoelectron., vol. 11, no. 1, pp. 2–22, Mar. 2018.

[7] I. Etsion, G. Halperin, and E. Becker. *The effect of various surface treatments on piston pin scuffing resistance*, Wear, vol. 261, no. 7–8, pp. 785–791, Oct. 2006.

[8] J. Schille, U. Loeschner, R. Ebert, P. Scully, N. Goddard, and H. Exner. *Laser micro processing using a high repetition rate femto second laser*, in *International Congress on Applications of Lasers & Electro-Optics*, 2010, no. November 2014, pp. 1491–1499.

[9] A. Y. Vorobyev and C. Guo. *Direct femtosecond laser surface nano/microstructuring and its applications*, Laser Photonics Rev., vol. 7, no. 3, pp. 385–407, 2013.

[10] A. Y. Vorobyev and C. Guo. *Multifunctional surfaces produced by femtosecond laser pulses*, J. Appl. Phys., vol. 117, no. 3, 2015.

[11] E. Skoulas, A. Manousaki, C. Fotakis, and E. Stratakis. *Biomimetic surface structuring using cylindrical vector femtosecond laser beams*, Sci. Rep., vol. 7, no. November 2016, pp. 1–11, 2017.

[12] A. Lasagni, S. Alamri, A. Aguilar-Morales, F. Rößler, B. Voisiat, and T. Kunze. *Biomimetic Surface Structuring Using Laser Based Interferometric Methods*, Appl. Sci., vol. 8, no. 8, p. 1260, 2018.

[13] B. Bhushan and Y. C. Jung. *Natural and biomimetic artificial surfaces for superhydrophobicity, self-cleaning, low adhesion, and drag reduction*, Prog. Mater. Sci., vol. 56, no. 1, pp. 1–108, Jan. 2011.

[14] R. Weber, T. Graf, P. Berger, V. Onuseit, M. Wiedenmann, C. Freitag, and A. Feuer. *Heat accumulation during pulsed laser materials processing*, Opt. Express, vol. 22, no. 9, p. 11312, May 2014.

[15] D. J. Förster, S. Faas, S. Gröninger, F. Bauer, A. Michalowski, R. Weber, and T. Graf. *Shielding effects and re-deposition of material during processing of metals with bursts of ultra-short laser pulses*, Appl. Surf. Sci., vol. 440, pp. 926–931, 2018.

[16] B. Neuenschwander, B. Jaeggi, M. Zimmermann, and G. Hennig. *Influence of particle shielding and heat accumulation effects onto the removal rate for laser micromachining with ultra-short pulses at high repetition rates*, in *International Congress on Applications of Lasers & Electro-Optics*, 2014, pp. 218–226.

[17] F. Bauer, A. Michalowski, T. Kiedrowski, and S. Nolte. *Heat accumulation in ultra-short pulsed scanning laser ablation of metals*, Opt. Express, vol. 23, no. 2, p. 1035, 2015.

[18] C. A. Zuhlke, T. P. Anderson, and D. R. Alexander. *Formation of multiscale surface structures on nickel via above surface growth and below surface growth mechanisms using femtosecond laser pulses*, Opt. Express, vol. 21, no. 7, p. 8460, Apr. 2013.

[19] T. Häfner, J. Heberle, M. Dobler, and M. Schmidt. *Influences on incubation in ps laser micromachining of steel alloys*, J. Laser Appl., vol. 28, no. 2, p. 022605, May 2016.

[20] O. Armbruster, A. Naghilou, M. Kitzler, and W. Kautek. *Spot size and pulse number dependence of femtosecond laser ablation thresholds of silicon and stainless steel*, Appl. Surf. Sci., vol. 396, pp. 1736–1740, Feb. 2017.

[21] F. Fraggelakis, G. Mincuzzi, J. Lopez, I. Manek-Hönninger, and R. Kling. *Texturing metal surface with MHz ultra-short laser pulses*, Opt. Express, vol. 25, no. 15, p. 18131, 2017.

[22] A. H. Hamad. *Effects of Different Laser Pulse Regimes (Nanosecond, Picosecond and Femtosecond) on the Ablation of Materials for Production of Nanoparticles in Liquid Solution*, in *High Energy and Short Pulse Lasers*, vol. i, InTech, 2016, p. 13.

[23] J. Schille. *Investigation of micromachining using a high repetition rate femtosecond fibre laser*, 2013.

[24] V. D. Ta, A. Dunn, T. J. Wasley, J. Li, R. W. Kay, J. Stringer, P. J. Smith, E. Esenturk, C. Connaughton, and J. D. Shephard. *Laser textured superhydrophobic surfaces and their applications for homogeneous spot deposition*, Appl. Surf. Sci., vol. 365, pp. 153–159, Mar. 2016.

[25] N. J. Shirtcliffe, G. McHale, S. Atherton, and M. I. Newton. *An introduction to superhydrophobicity*, Adv. Colloid Interface Sci., vol. 161, no. 1–2, pp. 124–138, 2010.

[26] S. Wang and L. Jiang. *Definition of superhydrophobic states*, Adv. Mater., vol. 19, no. 21, pp. 3423–3424, 2007.

[27] M. Groenendijk. *Fabrication of Super Hydrophobic Surfaces by fs Laser Pulses*, Laser Tech. J., vol. 5, no. 3, pp. 44–47, 2008.

[28] A. B. D. Cassie and S. Baxter. *Wettability of porous surfaces*, Trans. Faraday Soc., vol. 40, no. 5, p. 546, 1944.

[29] T. Young. *III. An essay on the cohesion of fluids*, Philos. Trans. R. Soc. London, vol. 95, no. 0, pp. 65–87, Jan. 1805.

[30] E. Kostal, S. Stroj, S. Kasemann, V. Matylitsky, and M. Domke. *Fabrication of Biomimetic*

Fog-Collecting Superhydrophilic-Superhydrophobic Surface Micropatterns Using Femtosecond Lasers, Langmuir, vol. 34, no. 9, pp. 2933–2941, 2018.

[31] R. N. Wenzel. *Resistance of solid surfaces to wetting by water*, Ind. Eng. Chem., vol. 28, no. 8, pp. 988–994, 1936.

[32] L. Zhang, N. Zhao, and J. Xu. *Fabrication and application of superhydrophilic surfaces: A review*, J. Adhes. Sci. Technol., vol. 28, no. 8–9, pp. 769–790, 2014.

[33] F. H. Rajab, Z. Liu, and L. Li. *Production of stable superhydrophilic surfaces on 316L steel by simultaneous laser texturing and SiO2deposition*, Appl. Surf. Sci., vol. 427, pp. 1135–1145, 2018.

[34] M. Domke, G. Sonderegger, E. Kostal, V. Matylitsky, and S. Stroj. *Transparent laser-structured glasses with superhydrophilic properties for anti-fogging applications*, Appl. Phys. A Mater. Sci. Process., vol. 125, no. 10, pp. 1–10, 2019.

[35] W. Barthlott and C. Neinhuis. *Purity of the sacred lotus, or escape from contamination in biological surfaces*, Planta, vol. 202, no. 1, pp. 1–8, 1997.

[36] S. Subhash Latthe, A. Basavraj Gurav, C. Shridhar Maruti, and R. Shrikant Vhatkar. *Recent Progress in Preparation of Superhydrophobic Surfaces: A Review*, J. Surf. Eng. Mater. Adv. Technol., vol. 02, no. 02, pp. 76–94, 2012.

[37] L. Feng, S. Li, Y. Li, H. Li, L. Zhang, J. Zhai, Y. Song, B. Liu, L. Jiang, and D. Zhu. *Super-Hydrophobic Surfaces: From Natural to Artificial*, Adv. Mater., vol. 14, no. 24, pp. 1857–1860, Dec. 2002.

[38] D. V. Ta, A. Dunn, T. J. Wasley, R. W. Kay, J. Stringer, P. J. Smith, C. Connaughton, and J. D. Shephard. *Nanosecond laser textured superhydrophobic metallic surfaces and their chemical sensing applications*, Appl. Surf. Sci., vol. 357, pp. 248–254, Dec. 2015.

[39] A. M. Emelyanenko, A. G. Domantovsky, K. A. Emelyanenko, and L. B. Boinovich. *Synthesis of wear-resistant superhydrophobic coatings via laser micro- and nanotexturing*, Nanotechnologies Russ., vol. 10, no. 7–8, pp. 585–592, 2015.

[40] J. Yong, F. Chen, Q. Yang, and X. Hou. *Femtosecond laser controlled wettability of solid surfaces*, Soft Matter, vol. 11, no. 46, pp. 8897–8906, 2015.

[41] M. Martínez-Calderon, A. Rodríguez, A. Dias-Ponte, M. C. Morant-Miñana, M. Gómez-Aranzadi, and S. M. Olaizola. *Femtosecond laser fabrication of highly hydrophobic stainless steel surface with hierarchical structures fabricated by combining ordered microstructures and LIPSS*, Appl. Surf. Sci., vol. 374, pp. 81–89, Jun. 2016.

[42] P. Bizi-Bandoki, S. Benayoun, S. Valette, B. Beaugiraud, and E. Audouard. *Modifications of roughness and wettability properties of metals induced by femtosecond laser treatment*, Appl. Surf. Sci., vol. 257, no. 12, pp. 5213–5218, 2011.

[43] Y. Lin, J. Han, M. Cai, W. Liu, X. Luo, H. Zhang, and M. Zhong. *Durable and robust transparent superhydrophobic glass surfaces fabricated by a femtosecond laser with exceptional water repellency and thermostability*, J. Mater. Chem. A, vol. 6, no. 19, pp. 9049–9056, 2018.

[44] M. S. Ahsan, F. Dewanda, M. S. Lee, H. Sekita, and T. Sumiyoshi. *Formation of*

superhydrophobic soda-lime glass surface using femtosecond laser pulses, Appl. Surf. Sci., vol. 265, pp. 784–789, 2013.

[45] M. R. Cardoso, R. J. Martins, A. Dev, T. Voss, and C. R. Mendonca. *Highly hydrophobic hierarchical nanomicro roughness polymer surface created by stamping and laser micromachining*, J. Appl. Polym. Sci., vol. 132, no. 24, pp. 2–5, 2015.

[46] M. T. Khorasani, H. Mirzadeh, and Z. Kermani. *Wettability of porous polydimethylsiloxane surface: Morphology study*, Appl. Surf. Sci., vol. 242, no. 3–4, pp. 339–345, 2005.

[47] S. R. Paital and N. B. Dahotre. *Wettability and kinetics of hydroxyapatite precipitation on a laser-textured Ca-P bioceramic coating*, Acta Biomater., vol. 5, no. 7, pp. 2763–2772, 2009.

[48] D. Zhang, F. Chen, Q. Yang, J. Yong, H. Bian, Y. Ou, J. Si, X. Meng, and X. Hou. *A simple way to achieve pattern-dependent tunable adhesion in superhydrophobic surfaces by a femtosecond laser*, ACS Appl. Mater. Interfaces, vol. 4, no. 9, pp. 4905–4912, 2012.

[49] X. Shi, X. Li, L. Jiang, L. Qu, Y. Zhao, P. Ran, Q. Wang, Q. Cao, T. Ma, and Y. Lu. *Femtosecond laser rapid fabrication of large-area rose-like micropatterns on freestanding flexible graphene films*, Sci. Rep., vol. 5, no. 1, p. 17557, Dec. 2015.

[50] J. Lu, C. V. Ngo, S. C. Singh, J. Yang, W. Xin, Z. Yu, and C. Guo. *Bioinspired Hierarchical Surfaces Fabricated by Femtosecond Laser and Hydrothermal Method for Water Harvesting*, Langmuir, vol. 35, no. 9, pp. 3562–3567, 2019.

[51] Y. Cai, W. Chang, X. Luo, A. M. L. Sousa, K. H. A. Lau, and Y. Qin. *Superhydrophobic structures on 316L stainless steel surfaces machined by nanosecond pulsed laser*, Precis. Eng., vol. 52, no. January, pp. 266–275, 2018.

[52] M. Rafieazad, J. A. Jaffer, C. Cui, X. Duan, and A. Nasiri. *Nanosecond laser fabrication of hydrophobic stainless steel surfaces: The impact on microstructure and corrosion resistance*, Materials (Basel)., vol. 11, no. 9, 2018.

[53] D. M. Chun, C. V. Ngo, and K. M. Lee. *Fast fabrication of superhydrophobic metallic surface using nanosecond laser texturing and low-temperature annealing*, CIRP Ann. - Manuf. Technol., vol. 65, no. 1, pp. 519–522, 2016.

[54] B. Wu, M. Zhou, J. Li, X. Ye, G. Li, and L. Cai. *Superhydrophobic surfaces fabricated by microstructuring of stainless steel using a femtosecond laser*, Appl. Surf. Sci., vol. 256, no. 1, pp. 61–66, 2009.

[55] R. Jagdheesh, B. Pathiraj, E. Karatay, G. R. B. E. Römer, and A. J. Huis in‘t Veld. *Laser-Induced Nanoscale Superhydrophobic Structures on Metal Surfaces*, Langmuir, vol. 27, no. 13, pp. 8464–8469, Jul. 2011.

[56] P. Bizi-Bandoki, S. Valette, E. Audouard, and S. Benayoun. *Time dependency of the hydrophilicity and hydrophobicity of metallic alloys subjected to femtosecond laser irradiations*, Appl. Surf. Sci., vol. 273, pp. 399–407, 2013.

[57] A. Cunha, A. P. Serro, V. Oliveira, A. Almeida, R. Vilar, and M. C. Durrieu. *Wetting behaviour of femtosecond laser textured Ti-6Al-4V surfaces*, Appl. Surf. Sci., vol. 265,

pp. 688–696, 2013.

[58] M. V. Rukosuyev, J. Lee, S. J. Cho, G. Lim, and M. B. G. Jun. *One-step fabrication of superhydrophobic hierarchical structures by femtosecond laser ablation*, Appl. Surf. Sci., vol. 313, pp. 411–417, 2014.

[59] A. Y. Vorobyev and C. Guo. *Multifunctional surfaces produced by femtosecond laser pulses*, J. Appl. Phys., vol. 117, no. 3, p. 033103, Jan. 2015.

[60] M. Domke, E. Kostal, S. Kasemann, V. Matylitsky, and S. Stroj. *Fabrication of bionic surfaces with mixed superhydrophobic and superhydrophilic properties using fs-lasers*, 2017.

[61] S. C. Vlădescu, S. Medina, A. V. Olver, I. G. Pegg, and T. Reddyhoff. *The Transient Friction Response of a Laser-Textured, Reciprocating Contact to the Entrainment of Individual Pockets*, Tribol. Lett., vol. 62, no. 2, pp. 1–12, 2016.

[62] D. Gropper, L. Wang, and T. J. Harvey. *Hydrodynamic lubrication of textured surfaces: A review of modeling techniques and key findings*, Tribol. Int., vol. 94, pp. 509–529, 2016.

[63] M. H. Sulaiman, P. Christiansen, and N. Bay. *The Influence of tool texture on friction and lubrication in strip reduction*, Procedia Eng., vol. 207, pp. 2263–2268, 2017.

[64] M. Scaraggi, F. P. Mezzapesa, G. Carbone, A. Ancona, D. Sorgente, and P. M. Lugarà. *Minimize friction of lubricated laser-microtextured-surfaces by tuning microholes depth*, Tribol. Int., vol. 75, pp. 123–127, Jul. 2014.

[65] K. Li, Z. Yao, Y. Hu, and W. Gu. *Friction and wear performance of laser peen textured surface under starved lubrication*, Tribol. Int., vol. 77, pp. 97–105, Sep. 2014.

[66] W. Tang, Y. Zhou, H. Zhu, and H. Yang. *The effect of surface texturing on reducing the friction and wear of steel under lubricated sliding contact*, Appl. Surf. Sci., vol. 273, pp. 199–204, May 2013.

[67] M. L. Conditions. *Effect of Surface Texturing on Cast Iron Reciprocating against Steel under Cyclic Loading in Boundary and Mixed Lubrication Conditions*, Lubricants, vol. 6, no. 1, p. 2, Jan. 2018.

[68] D. Gropper, L. Wang, and T. J. Harvey. *Hydrodynamic lubrication of textured surfaces: A review of modeling techniques and key findings*, Tribol. Int., vol. 94, pp. 509–529, Feb. 2016.

[69] D. Braun, C. Greiner, J. Schneider, and P. Gumbsch. *Efficiency of laser surface texturing in the reduction of friction under mixed lubrication*, Tribol. Int., vol. 77, pp. 142–147, Sep. 2014.

[70] M. Scaraggi. *Partial surface texturing: A mechanism for local flow reconditioning in lubricated contacts*, Proc. Inst. Mech. Eng. Part J J. Eng. Tribol., vol. 229, no. 4, pp. 493–504, 2015.

[71] A. Ancona, G. Joshi, A. Volpe, M. Scaraggi, P. Lugarà, and G. Carbone. *Non-Uniform Laser Surface Texturing of an Un-Tapered Square Pad for Tribological Applications*, Lubricants, vol. 5, no. 4, p. 41, Oct. 2017.

[72] A. Ancona, G. S. Joshi, C. Gaudiuso, and C. Putignano. *Modifying steel surface tribology by ultrafast laser micro-texturing*, in *LPM2018*, 2018, pp. 1–5.

[73] D. Z. Segu, S. G. Choi, J. H. Choi, and S. S. Kim. *The effect of multi-scale laser textured surface on lubrication regime*, Appl. Surf. Sci., vol. 270, pp. 58–63, Apr. 2013.

[74] Y. Xing, J. Deng, Z. Wu, and F. Wu. *High friction and low wear properties of laser-textured ceramic surface under dry friction*, Opt. Laser Technol., vol. 93, pp. 24–32, 2017.

[75] F. Saeidi, M. Parlinska-Wojtan, P. Hoffmann, and K. Wasmer. *Effects of laser surface texturing on the wear and failure mechanism of grey cast iron reciprocating against steel under starved lubrication conditions*, Wear, vol. 386–387, no. May, pp. 29–38, 2017.

[76] D. Z. Segu, J.-H. Kim, S. G. Choi, Y.-S. Jung, and S.-S. Kim. *Application of Taguchi techniques to study friction and wear properties of MoS2 coatings deposited on laser textured surface*, Surf. Coatings Technol., vol. 232, pp. 504–514, Oct. 2013.

[77] A. F. Shamsul Baharin, M. J. Ghazali, and J. A Wahab. *Laser surface texturing and its contribution to friction and wear reduction: A brief review*, Ind. Lubr. Tribol., vol. 68, no. 1, pp. 57–66, 2016.

[78] A. I. Aguilar-Morales, S. Alamri, and A. F. Lasagni. *Micro-fabrication of high aspect ratio periodic structures on stainless steel by picosecond direct laser interference patterning*, J. Mater. Process. Technol., vol. 252, no. January 2018, pp. 313–321, 2018.

[79] S. Alamri, A. I. Aguilar-Morales, and A. F. Lasagni. *Controlling the wettability of polycarbonate substrates by producing hierarchical structures using Direct Laser Interference Patterning*, Eur. Polym. J., vol. 99, no. August 2017, pp. 27–37, Feb. 2018.

[80] J. T. Cardoso, A. I. Aguilar-Morales, S. Alamri, D. Huerta-Murillo, F. Cordovilla, A. F. Lasagni, and J. L. Ocaña. *Superhydrophobicity on hierarchical periodic surface structures fabricated via direct laser writing and direct laser interference patterning on an aluminium alloy*, Opt. Lasers Eng., vol. 111, no. July, pp. 193–200, 2018.

[81] U. Hermens, S. V. Kirner, C. Emonts, P. Comanns, E. Skoulas, A. Mimidis, H. Mescheder, K. Winands, J. Krüger, E. Stratakis, and J. Bonse. *Mimicking lizard-like surface structures upon ultrashort laser pulse irradiation of inorganic materials*, Appl. Surf. Sci., vol. 418, pp. 499–507, 2017.

[82] C. Kunz, F. Müller, and S. Gräf. *Multifunctional Hierarchical Surface Structures by Femtosecond Laser Processing*, Materials (Basel)., vol. 11, no. 5, p. 789, May 2018.

[83] F. Roessler and A. F. Lasagni. *Fabrication of hierarchical surface patterns using direct laser interference patterning as protection against mechanical damage*, in *LANE2018*, 2018.

[84] M. S. Brown and C. B. Arnold. *Fundamentals of Laser-Material Interaction and Application to Multiscale Surface Modification*, in *FLaser Precision Microfabrication*, Intergovernmental Panel on Climate Change, Ed. Cambridge: Cambridge University Press, 2010, pp. 91–120.

[85] A. Vinčiunas, S. Indrišiunas, B. Voisiat, G. Račiukaitis, I. Šimkiene, R. Suzanovičiene, A.

Reza, and R. Mažeikiene. *Effect of laser patterning on properties of crystalline Si photovoltaic cells and substrates*, J. Laser Micro Nanoeng., vol. 8, no. 3, pp. 244–252, 2013.

[86] B. Voisiat, S. Indrišiūnas, G. Račiukaitis, I. Šimkienė, A. Rėza, and R. Suzanovičienė. *Application of Laser Texturing in Silicon Solar Cell Technology*, Mater. Sci., vol. 20, no. 2, pp. 157–159, 2014.

[87] M. Abbott and J. Cotter. *Optical and electrical properties of laser texturing for high-efficiency solar cells*, J. Optoelectron. Adv. Mater., vol. 14, no. 3, pp. 225–235, 2006.

[88] B. Zheng, W. Wang, G. Jiang, and X. Mei. *Fabrication of broadband antireflective black metal surfaces with ultra-light-trapping structures by picosecond laser texturing and chemical fluorination*, Appl. Phys. B, vol. 122, no. 6, p. 180, Jun. 2016.

[89] C. Paper, B. Radfar, F. Es, H. Nasser, and A. Bek. *Effect of laser parameters and post-texturing treatments on the optical and electrical properties of laser textured c-Si wafers Effect of laser parameters and post-texturing treatments on the optical and electrical Behrad Radfar , Firat Es , Hisham Nasser*, no. August, 2018.

[90] B. K. Nayak and M. C. Gupta. *Self-organized micro/nano structures in metal surfaces by ultrafast laser irradiation*, Opt. Lasers Eng., vol. 48, no. 10, pp. 940–949, 2010.

[91] P. Vukusic, J. R. Sambles, C. R. Lawrence, and R. J. Wootton. *Quanti ® ed interference and diffraction in single Morpho butter ¯ y scales*, no. April, 1999.

[92] J. M. Guay, A. Calà Lesina, G. Côté, M. Charron, D. Poitras, L. Ramunno, P. Berini, and A. Weck. *Laser-induced plasmonic colours on metals*, Nat. Commun., vol. 8, no. May, 2017.

[93] M. Mikutis, T. Kudrius, G. Šlekys, D. Paipulas, and S. Juodkazis. *High 90% efficiency Bragg gratings formed in fused silica by femtosecond Gauss-Bessel laser beams*, Opt. Mater. Express, vol. 3, no. 11, p. 1862, 2013.

[94] D. Gailevičius, V. Purlys, M. Peckus, R. Gadonas, and K. Staliunas. *Spatial Filters on Demand Based on Aperiodic Photonic Crystals*, Ann. Phys., vol. 529, no. 8, pp. 1–4, 2017.

[95] S. Gloor, V. Romano, W. Lüthy, H. P. Weber, V. V. Kononenko, S. M. Pimenov, V. I. Konov, and A. V. Khomich. *Antireflection structures written by excimer laser on CVD diamond*, Appl. Phys. A Mater. Sci. Process., vol. 70, no. 5, pp. 547–550, 2000.

[96] S. K. Sundaram and E. Mazur. *Inducing and probing non-thermal transitions in semiconductors using femtosecond laser pulses*, Nat. Mater., vol. 1, no. 4, pp. 217–224, 2002.

[97] D. Trucchi, A. Bellucci, M. Girolami, M. Mastellone, and S. Orlando. *Surface Texturing of CVD Diamond Assisted by Ultrashort Laser Pulses*, Coatings, vol. 7, no. 11, p. 185, 2017.

[98] P. Calvani, A. Bellucci, M. Girolami, S. Orlando, V. Valentini, A. Lettino, and D. M. Trucchi. *Optical properties of femtosecond laser-treated diamond*, Appl. Phys. A Mater. Sci. Process., vol. 117, no. 1, pp. 25–29, 2014.

[99] D. S. Wang, S. Y. Chang, T. S. Chen, T. H. Chou, Y. C. Huang, J. B. Wu, M. S. Leu, and H. J. Lai. *Stress Writing Textured Graphite Conducting Wires/Patterns in Insulating Amorphous Carbon Matrix as Interconnects*, Sci. Rep., vol. 7, no. 1, pp. 1–10, 2017.

[100] P. Shukla, D. G. Waugh, J. Lawrence, and R. Vilar. *Laser surface structuring of ceramics, metals and polymers for biomedical applications*, in *Laser Surface Modification of Biomaterials*, no. December, Elsevier, 2016, pp. 281–299.

[101] R. Kumari, T. Scharnweber, W. Pfleging, H. Besser, and J. D. Majumdar. *Laser surface textured titanium alloy (Ti–6Al–4V) – Part II – Studies on bio-compatibility*, Appl. Surf. Sci., vol. 357, pp. 750–758, Dec. 2015.

[102] N. B. Dahotre, S. R. Paital, A. N. Samant, and C. Daniel. *Wetting behaviour of laser synthetic surface microtextures on Ti-6Al-4V for bioapplication*, Philos. Trans. R. Soc. A Math. Phys. Eng. Sci., vol. 368, no. 1917, pp. 1863–1889, 2010.

[103] S. R. Paital, N. Bunce, P. Nandwana, C. Honrao, S. Nag, W. He, R. Banerjee, and N. B. Dahotre. *Laser surface modification for synthesis of textured bioactive and biocompatible Ca-P coatings on Ti-6Al-4V*, J. Mater. Sci. Mater. Med., vol. 22, no. 6, pp. 1393–1406, 2011.

[104] B. Oktem, H. Kalaycioglu, M. Erdoğan, S. Yavaş, P. Mukhopadhyay, U. H. Tazebay, Y. Aykaç, K. Eken, and F. Ö. Ilday. *Surface texturing of dental implant surfaces with an ultrafast fiber laser*, Lasers Electro-Optics/Quantum Electron. Laser Sci. Conf. 2010 Laser Sci. to Photonic Appl. CLEO/QELS 2010, pp. 1–2, 2010.

[105] S. Çelen, C. Efeoğlu, and H. Özden. *Pulsed laser-induced micro-pits: As bone stabilizers*, Phys. Procedia, vol. 12, no. PART 2, pp. 245–251, 2011.

[106] C. Hallgren, H. Reimers, D. Chakarov, J. Gold, and A. Wennerberg. *An in vivo study of bone response to implants topographically modified by micromachining*, Biomaterials, vol. 24, no. 5, pp. 701–710, 2003.

[107] R. Brånemark, L. Emanuelsson, A. Palmquist, and P. Thomsen. *Bone response to laser-induced micro- and nano-size titanium surface features*, Nanomedicine Nanotechnology, Biol. Med., vol. 7, no. 2, pp. 220–227, 2011.

[108] N. Lin, D. Li, J. Zou, R. Xie, Z. Wang, and B. Tang. *Surface Texture-Based Surface Treatments on Ti6Al4V Titanium Alloys for Tribological and Biological Applications: A Mini Review*, Materials (Basel)., vol. 11, no. 4, p. 487, Mar. 2018.

[109] J. Chen, S. Mwenifumbo, C. Langhammer, J.-P. McGovern, M. Li, A. Beye, and W. O. Soboyejo. *Cell/surface interactions and adhesion on Ti-6Al-4V: Effects of surface texture*, J. Biomed. Mater. Res. Part B Appl. Biomater., vol. 82B, no. 2, pp. 360–373, Aug. 2007.

[110] A. Riveiro, A. L. B. Maçon, J. del Val, R. Comesaña, and J. Pou. *Laser Surface Texturing of Polymers for Biomedical Applications*, Front. Phys., vol. 6, no. February, Feb. 2018.

[111] J. P. Ulerich, L. C. Ionescu, J. Chen, W. O. Soboyejo, and C. B. Arnold. *Modifications of Ti-6Al-4V surfaces by direct-write laser machining of linear grooves*, vol. 6458, p. 645819, 2007.

[112] S. Mukherjee, S. Dhara, and P. Saha. *Enhancing the biocompatibility of Ti6Al4V implants by laser surface microtexturing: an in vitro study*, Int. J. Adv. Manuf. Technol., vol. 76, no. 1–4, pp. 5–15, Jan. 2015.

[113] K. van der Straeten, I. Burkhardt, A. Olowinsky, and A. Gillner. *Laser-induced Self-organizing Microstructures on Steel for Joining with Polymers*, Phys. Procedia, vol. 83, pp. 1137–1144, 2016.

[114] E. Rodríguez-Vidal, J. Lambarri, C. Soriano, C. Sanz, and G. Verhaeghe. *A combined experimental and numerical approach to the laser joining of hybrid polymer - Metal parts*, Phys. Procedia, vol. 56, no. C, pp. 835–844, 2014.

[115] P. Amend, T. Häfner, M. Gränitz, S. Roth, and M. Schmidt. *Effect of Ultrashort Pulse Laser Structuring of Stainless Steel on Laser-based Heat Conduction Joining of Polyamide Steel Hybrids*, Phys. Procedia, vol. 83, pp. 1130–1136, 2016.

[116] E. Rodríguez-vidal, C. Sanz, C. Soriano, J. Leunda, and G. Verhaeghe. *Journal of Materials Processing Technology Effect of metal micro-structuring on the mechanical behavior of polymer – metal laser T-joints*, J. Mater. Process. Tech., vol. 229, pp. 668–677, 2016.

[117] A. Lamraoui, S. Costil, C. Langlade, and C. Coddet. *Laser surface texturing (LST) treatment before thermal spraying: A new process to improve the substrate-coating adherence*, Surf. Coatings Technol., vol. 205, no. 2010, pp. S164–S167, Dec. 2010.

[118] R. Kromer, J. Cormier, S. Costil, D. Courapied, L. Berthe, and P. Peyre. *High temperature durability of a bond-coatless plasma-sprayed thermal barrier coating system with laser textured Ni-based single crystal substrate*, Surf. Coatings Technol., vol. 337, no. January, pp. 168–176, 2018.

[119] D. Garcia-Alonso, N. Serres, C. Demian, S. Costil, C. Langlade, and C. Coddet. *Pre-/During-/Post-Laser Processes to Enhance the Adhesion and Mechanical Properties of Thermal-Sprayed Coatings with a Reduced Environmental Impact*, J. Therm. Spray Technol., vol. 20, no. 4, pp. 719–735, Jun. 2011.

[120] J. Byskov-Nielsen and P. Balling. *Laser structuring of metal surfaces: Micro-mechanical interlocking*, Appl. Surf. Sci., vol. 255, no. 10, pp. 5591–5594, Mar. 2009.

[121] J. Byskov-Nielsen. *Short-pulse laser ablation of metals : Fundamentals and applications for micro-mechanical interlocking*, Appl. Phys., no. August, p. 96, 2010.

[122] R. Kromer, S. Costil, J. Cormier, L. Berthe, P. Peyre, and D. Courapied. *Laser Patterning Pretreatment before Thermal Spraying: A Technique to Adapt and Control the Surface Topography to Thermomechanical Loading and Materials*, J. Therm. Spray Technol., vol. 25, no. 3, pp. 401–410, 2016.

[123] R. Kromer, J. Cormier, and S. Costil. *Role of Powder Granulometry and Substrate Topography in Adhesion Strength of Thermal Spray Coatings*, J. Therm. Spray Technol., vol. 25, no. 5, pp. 933–945, Jun. 2016.

[124] R. Kromer, S. Costil, C. Verdy, S. Gojon, and H. Liao. *Laser surface texturing to enhance adhesion bond strength of spray coatings – Cold spraying, wire-arc spraying, and atmospheric plasma spraying*, Surf. Coatings Technol., vol. 352, pp. 642–653, Oct. 2018.

[125] B. Rethfeld, D. S. Ivanov, M. E. Garcia, and S. I. Anisimov. *Modelling ultrafast laser ablation*, J. Phys. D. Appl. Phys., vol. 50, no. 19, 2017.

[126] A. T. B.N. Chichkov, C. Momma, S. Nolte, F. von Alvensleben. *Femtosecond, picosecond*

and nanosecond laser ablation of solids, Appl. Phys. A, vol. 63, pp. 109–115, 1996.

[127] D. Bäuerle. *Laser Processing and Chemistry*. 2011.

[128] K. H. Leitz, B. Redlingshöer, Y. Reg, A. Otto, and M. Schmidt. *Metal ablation with short and ultrashort laser pulses*, Phys. Procedia, vol. 12, no. PART 2, pp. 230–238, 2011.

[129] L. L. Taylor, R. E. Scott, and J. Qiao. *Integrating two-temperature and classical heat accumulation models to predict femtosecond laser processing of silicon*, Opt. Mater. Express, vol. 8, no. 3, p. 648, 2018.

[130] M. V. Shugaev, I. Gnilitskyi, N. M. Bulgakova, and L. V. Zhigilei. *Mechanism of single-pulse ablative generation of laser-induced periodic surface structures*, Phys. Rev. B, vol. 96, no. 20, pp. 1–9, 2017.

[131] E. E. B. C. N.M. Bulgakova, R. Stoian, A. Rosenfeld, I.V. Hertel, W. Marine. *A general continuum approach to describe fast electronic transport in pulsed laser irradiated materials : The problem of Coulomb explosion*, Appl. Phys. A, vol. 81, no. 2, pp. 345–356, 2005.

[132] M. V. Shugaev, C. Wu, O. Armbruster, A. Naghilou, N. Brouwer, D. S. Ivanov, T. J. Y. Derrien, N. M. Bulgakova, W. Kautek, B. Rethfeld, and L. V. Zhigilei. *Fundamentals of ultrafast laser-material interaction*, MRS Bull., vol. 41, no. 12, pp. 960–968, 2016.

[133] S. I. Anisimov. *Electron emission from metal surfaces exposed to ultrashort laser pulses*, Sov. Phys.-JETP, vol. 39, pp. 375–377, 1975.

[134] Y. V. Afanasiev, B. N. Chichkov, N. N. Demchenko, V. A. Isakov, and I. N. Zavestovskaya. *Ablation of metals by ultrashort laser pulses: Theoretical modeling and computer simulations*, J. Russ. Laser Res., vol. 20, no. 2, pp. 89–115, Mar. 1999.

[135] E. G. Gamaly, A. V Rode, and B. Luther-davies. *Ablation of solids by femtosecond lasers : ablation mechanism and ablation thresholds for metals and dielectrics*, no. August 2013, 2001.

[136] C. Wu and L. V. Zhigilei. *Microscopic mechanisms of laser spallation and ablation of metal targets from large-scale molecular dynamics simulations*, Appl. Phys. A Mater. Sci. Process., vol. 114, no. 1, pp. 11–32, 2014.

[137] D. J. Förster, D. Anh, V. Onuseit, R. Weber, and T. Graf. *Lasers in Manufacturing Conference 2015 Energy transfer mechanisms during laser pulsed processing of metals*, 2015.

[138] L. I. M. and T. L. V Kaganov M I. *Relaxation between electrons and the crystalline lattice*, Sov. Phys.- JETP, vol. 4, pp. 173–178, 1957.

[139] T. Itina, M. Povarnitsyn, and K. Khishchenko. *Modeling Of Laser Ablation Induced By Nanosecond And Femtosecond Laser Pulses*, no. January 2016. 2011.

[140] M. Olbrich, E. Punzel, P. Lickschat, S. Weißmantel, and A. Horn. *Investigation on the ablation of thin metal films with femtosecond to picosecond-pulsed laser radiation*, Phys. Procedia, vol. 83, pp. 93–103, 2016.

[141] B. Rethfeld, K. Sokolowski-Tinten, D. Von Der Linde, and S. I. Anisimov. *Timescales in*

the response of materials to femtosecond laser excitation, Appl. Phys. A Mater. Sci. Process., vol. 79, no. 4–6, pp. 767–769, 2004.

[142] Honner. *Wave and parallel*. 1999.

[143] M. Honner. *Wave and parallel*. 2001.

[144] P. Balling. *Ultrashort-pulse laser excitation of materials*, no. July, 2014.

[145] J. M. Vadillo and J. J. Laserna. *Monitoring the dynamics of the surface deformation prior to the onset of plasma emission during femtosecond laser ablation of noble metals by time-resolved re fl ectivity microscopy*, Spectrochim. Acta Part B At. Spectrosc., vol. 131, pp. 1–7, 2017.

[146] E. G. Gamaly and A. V Rode. *Physics of ultra-short laser interaction with matter : From phonon excitation to ultimate transformations*, Prog. Quantum Electron., vol. 37, no. 5, pp. 215–323, 2013.

[147] J. Hohlfeld, J. G. Müller, S. S. Wellershoff, and E. Matthias. *Time-resolved thermoreflectivity of thin gold films and its dependence on film thickness*, Appl. Phys. B Lasers Opt., vol. 64, no. 3, pp. 387–390, 1997.

[148] R. Fang, A. Vorobyev, and C. Guo. *Direct visualization of the complete evolution of femtosecond laser-induced surface structural dynamics of metals*, Light Sci. Appl., vol. 6, no. 3, pp. e16256-7, 2017.

[149] B. Rethfeld, K. Sokolowski-Tinten, D. von der Linde, and S. I. Anisimov. *Ultrafast thermal melting of laser-excited solids by homogeneous nucleation*, Phys. Rev. B, vol. 65, no. 9, p. 092103, 2002.

[150] I. Carrasco-García, J. M. Vadillo, and J. Javier Laserna. *Visualization of surface transformations during laser ablation of solids by femtosecond pump–probe time-resolved microscopy*, Spectrochim. Acta Part B At. Spectrosc., vol. 113, pp. 30–36, Nov. 2015.

[151] E. L. Gurevich and S. V. Gurevich. *Laser Induced Periodic Surface Structures induced by surface plasmons coupled via roughness*, Appl. Surf. Sci., vol. 302, pp. 118–123, 2014.

[152] T. T. D. Huynh, M. Vayer, A. Sauldubois, A. Petit, and N. Semmar. *Evidence of liquid phase during laser-induced periodic surface structures formation induced by accumulative ultraviolet picosecond laser beam*, Appl. Phys. Lett., vol. 107, no. 19, 2015.

[153] L. V Zhigilei, Z. Lin, D. S. Ivanov, and V. Charlottes. *Atomistic Modeling of Short Pulse Laser Ablation of Metals : Connections between Melting , Spallation , and Phase Explosion †*, pp. 11892–11906, 2009.

[154] B. Emile, B. Emile, J. Colombier, B. Dutta, R. Stoian, and A. Ini-. *Ab Initio Nonequilibrium Thermodynamic and Transport Properties of Ultrafast Laser Irradiated 316L Stainless Steel To cite this version :*, J. Phys. Chem. C, vol. 119, no. 21, pp. 11438–11446, 2015.

[155] M. S. Brown and C. B. Arnold. *Laser Precision Microfabrication*, Springer Ser. Mater. Sci., vol. 135, no. 0933–033X, pp. 91–120, 2010.

[156] A. Physics. *Photomechanical spallation of molecular and metal targets : molecular*

dynamics study, vol. 1655, pp. 1643–1655, 2004.

[157] J. König. *Plasma evolution during metal ablation with ultrashort laser pulses*, vol. 13, no. 26, pp. 186–196, 2005.

[158] J. Mildner, C. Sarpe, N. Götte, M. Wollenhaupt, and T. Baumert. *Applied Surface Science Emission signal enhancement of laser ablation of metals (aluminum and titanium) by time delayed femtosecond double pulses from femtoseconds to nanoseconds*, Appl. Surf. Sci., vol. 302, pp. 291–298, 2014.

[159] I. Carrasco-García, J. M. Vadillo, J. Javier Laserna, and J. J. Laserna. *Monitoring the dynamics of the surface deformation prior to the onset of plasma emission during femtosecond laser ablation of noble metals by time-resolved reflectivity microscopy*, Spectrochim. Acta - Part B At. Spectrosc., vol. 131, pp. 1–7, 2017.

[160] V. V Temnov, S. Kudryashov, and A. Cavalleri. *Ablation dynamics of solids heated by femtosecond laser pulses*, no. June, 2001.

[161] S. Amoruso, R. Bruzzese, C. Pagano, and X. Wang. *Features of plasma plume evolution and material removal efficiency during femtosecond laser ablation of nickel in high vacuum*, Appl. Phys. A Mater. Sci. Process., vol. 89, no. 4, pp. 1017–1024, 2007.

[162] P. Lorazo, L. J. Lewis, and M. Meunier. *Thermodynamic pathways to melting , ablation , and solidification in absorbing solids under pulsed laser irradiation*, pp. 1–22, 2006.

[163] P. Sankar, H. D. Shashikala, and R. Philip. *Effect of laser beam size on the dynamics of ultrashort laser-produced aluminum plasma in vacuum*, Phys. Plasmas, vol. 26, no. 1, 2019.

[164] T. Y. Choi and C. P. Grigoropoulos. *Plasma and ablation dynamics in ultrafast laser processing of crystalline silicon Plasma and ablation dynamics in ultrafast laser processing of crystalline silicon*, no. November, 2002.

[165] C. Wu, M. S. Christensen, J. M. Savolainen, P. Balling, and L. V. Zhigilei. *Generation of subsurface voids and a nanocrystalline surface layer in femtosecond laser irradiation of a single-crystal Ag target*, Phys. Rev. B - Condens. Matter Mater. Phys., vol. 91, no. 3, pp. 1–14, 2015.

[166] I. Carrasco-García, J. M. Vadillo, and J. Javier Laserna. *Monitoring the dynamics of the surface deformation prior to the onset of plasma emission during femtosecond laser ablation of noble metals by time-resolved reflectivity microscopy*, Spectrochim. Acta Part B At. Spectrosc., vol. 131, pp. 1–7, May 2017.

[167] E. G. Gamaly, A. V Rode, V. T. Tikhonchuk, and B. Luther-davies. *Electrostatic mechanism of ablation by femtosecond lasers*, vol. 198, pp. 699–704, 2002.

[168] A. . Fallis. *Laser Precision Microfabrication*, vol. 53, no. 9. 2013.

[169] S. Niehoff and F. Vollertsen. *Laser induced shock waves in deformation processing*, Metalurgija, vol. 11, no. 3, pp. 183–194, 2005.

[170] L. Zhang, J. Z. Lu, Y. K. Zhang, H. Le Ma, K. Y. Luo, and F. Z. Dai. *Effects of laser shock processing on morphologies and mechanical properties of ANSI 304 stainless steelweldments subjected to cavitation erosion*, Materials (Basel)., vol. 10, no. 3, 2017.

[171] N. Singh, K. Ahuja, T. singh, and S. Singh. *A Review: Effect of Laser Peening Treatment on Properties And Life Cycle of Different Materials*, IOSR J. Mech. Civ. Eng., vol. 14, no. 01, pp. 83–94, 2017.

[172] G. Tani, L. Orazi, A. Fortunato, A. Ascari, and G. Campana. *Warm Laser Shock Peening: New developments and process optimization*, CIRP Ann., vol. 60, no. 1, pp. 219–222, 2011.

[173] Y. Shadangi, K. Chattopadhyay, S. B. Rai, and V. Singh. *Effect of LASER shock peening on microstructure, mechanical properties and corrosion behavior of interstitial free steel*, Surf. Coatings Technol., vol. 280, pp. 216–224, 2015.

[174] B. Wu, S. Tao, and S. Lei. *Numerical modeling of laser shock peening with femtosecond laser pulses and comparisons to experiments*, Appl. Surf. Sci., vol. 256, no. 13, pp. 4376–4382, Apr. 2010.

[175] S. Petronic, A. Milosavljevic, D. Milovanovic, M. Momcilovic, and Z. Radovanovic. *Influence of picosecond laser pulses on the microstructure of austenitic materials*, J. Russ. Laser Res., vol. 32, no. 6, pp. 564–571, 2011.

[176] N. Bulgakova, A. Panchenko, V. Zhukov, S. Kudryashov, A. Pereira, W. Marine, T. Mocek, and A. Bulgakov. *Impacts of Ambient and Ablation Plasmas on Short- and Ultrashort-Pulse Laser Processing of Surfaces*, Micromachines, vol. 5, no. 4, pp. 1344–1372, Dec. 2014.

[177] J. M. Lee and K. G. Watkins. *In-process monitoring techniques for laser cleaning*, Opt. Lasers Eng., vol. 34, no. 4–6, pp. 429–442, 2000.

[178] M. Verdier, S. Costil, C. Coddet, R. Oltra, and O. Perret. *On the topographic and energetic surface modi ® cations induced by laser treatment of metallic substrates before plasma spraying*, vol. 205, 2003.

[179] F. Dausinger, H. Hugel, and V. I. Konov. *Micromachining with ultrashort laser pulses: from basic understanding to technical applications*, in *SPIE proc.*, 2003, vol. 5147, pp. 106–115.

[180] G. Račiukaitis, M. Brikas, P. Gečys, B. Voisiat, and M. Gedvilas. *Use of high repetition rate and high power lasers in microfabrication: How to keep the efficiency high?*, J. Laser Micro Nanoeng., vol. 4, no. 3, pp. 186–191, 2009.

[181] B. Neuenschwander, B. Jaeggi, M. Schmid, and G. Hennig. *Surface structuring with ultra-short laser pulses: Basics, limitations and needs for high throughput*, Phys. Procedia, vol. 56, no. C, pp. 1047–1058, 2014.

[182] J. Byskov-Nielsen, J. M. Savolainen, M. S. Christensen, and P. Balling. *Ultra-short pulse laser ablation of copper, silver and tungsten: Experimental data and two-temperature model simulations*, Appl. Phys. A Mater. Sci. Process., vol. 103, no. 2, pp. 447–453, 2011.

[183] B. Jaeggi, B. Neuenschwander, M. Schmid, M. Muralt, J. Zuercher, and U. Hunziker. *Influence of the pulse duration in the ps-regime on the ablation efficiency of metals*, Phys. Procedia, vol. 12, no. PART 2, pp. 164–171, 2011.

[184] C. S. R. Nathala, A. Ajami, W. Husinsky, B. Farooq, S. I. Kudryashov, A. Daskalova, I.

Bliznakova, and A. Assion. *Ultrashort laser pulse ablation of copper, silicon and gelatin: effect of the pulse duration on the ablation thresholds and the incubation coefficients*, Appl. Phys. A Mater. Sci. Process., vol. 122, no. 2, pp. 1–8, 2016.

[185] C. Y. Chien and M. C. Gupta. *Pulse width effect in ultrafast laser processing of materials*, Appl. Phys. A, vol. 81, no. 6, pp. 1257–1263, Nov. 2005.

[186] G. Raciukaitis, M. Brikas, P. Gecys, and M. Gedvilas. *Accumulation effects in laser ablation of metals with high-repetition-rate lasers*, in *Proc. SPIE, 7005*, 2008, no. MAY, p. 70052L.

[187] V. I. Emel and D. V Babak. *Defect capture under rapid solidification of the melt induced by the action of femtosecond laser pulses and formation of periodic surface structures on a semiconductor surface*, vol. 805, pp. 797–805, 2002.

[188] D. Lee. *Feasibility study on laser microwelding and laser shock peening using femtosecond laser pulses*, 2008.

[189] C. A. Zuhlke, T. P. Anderson, and D. R. Alexander. *Formation of multiscale surface structures on nickel via above surface growth and below surface growth mechanisms using femtosecond laser pulses*, Opt. Express, vol. 21, no. 7, pp. 8460–8473, 2013.

[190] J. S. Hoppius, L. M. Kukreja, M. Knyazeva, F. Pöhl, F. Walther, A. Ostendorf, and E. L. Gurevich. *On femtosecond laser shock peening of stainless steel AISI 316*, Appl. Surf. Sci., vol. 435, pp. 1120–1124, 2018.

[191] E. V Golosov, T. N. Vershinina, M. V Zhidkov, A. A. Ionin, S. I. Kudryashov, S. V Makarov, L. V Seleznev, D. V Sinitsyn, and A. E. Ligachev. *Structural transformation and residual stresses in surface layers of a + b titanium alloys nanotextured by femtosecond laser pulses*, pp. 241–247, 2015.

[192] F. Di Niso, C. Gaudiuso, T. Sibillano, F. P. Mezzapesa, A. Ancona, and P. M. Lugarà. *Influence of the repetition rate and pulse duration on the incubation effect in multiple-shots ultrafast laser ablation of steel*, Phys. Procedia, vol. 41, pp. 698–707, 2013.

[193] L. M. Machado, R. E. Samad, A. Z. Freitas, N. D. Vieira, and W. De Rossi. *Microchannels direct machining using the femtosecond smooth ablation method*, Phys. Procedia, vol. 12, no. PART 2, pp. 67–75, 2011.

[194] F. Di Niso, C. Gaudiuso, T. Sibillano, F. Paolo, A. Ancona, and P. M. Lugarà. *Role of heat accumulation on the incubation effect in multi-shot laser ablation of stainless steel at high repetition rates*, vol. 22, no. 10, pp. 2230–2236, 2014.

[195] A. Naghilou, O. Armbruster, and W. Kautek. *Femto- and nanosecond pulse laser ablation dependence on irradiation area: The role of defects in metals and semiconductors*, Appl. Surf. Sci., vol. 418, pp. 487–490, 2017.

[196] J. Finger and M. Reininghaus. *Effect of pulse to pulse interactions on ultra-short pulse laser drilling of steel with repetition rates up to 10 MHz*, Opt. Express, vol. 22, no. 15, p. 18790, 2014.

[197] R. Weber, T. Graf, C. Freitag, A. Feuer, T. Kononenko, and V. I. Konov. *Processing constraints resulting from heat accumulation during pulsed and repetitive laser*

materials processing, Opt. Express, vol. 25, no. 4, p. 3966, 2017.

[198] F. Bauer, A. Michalowski, T. Kiedrowski, and S. Nolte. *Heat accumulation in ultra-short pulsed scanning laser ablation of metals*, Opt. Express, vol. 23, no. 2, p. 1035, Jan. 2015.

[199] B. Neuenschwander, B. Jaeggi, M. Zimmermannn, V. Markovic, B. Resan, K. Weingarten, R. de Loor, and L. Penning. *Laser surface structuring with 100 W of average power and sub-ps pulses*, J. Laser Appl., vol. 28, no. 2, p. 022506, May 2016.

[200] X. C. Wang, H. Y. Zheng, P. L. Chu, J. L. Tan, K. M. Teh, T. Liu, B. C. Y. Ang, and G. H. Tay. *Femtosecond laser drilling of alumina ceramic substrates*, Appl. Phys. A, vol. 101, pp. 271–278, 2010.

[201] A. Ancona, F. Röser, K. Rademaker, J. Limpert, S. Nolte, and A. Tünnermann. *High speed laser drilling of metals using a high repetition rate, high average power ultrafast fiber CPA system*, Opt. Express, vol. 16, no. 12, p. 8958, Jun. 2008.

[202] A. Tuennermann, S. Nolte, and J. Limpert. *Femtosecond vs. Picosecond Laser Material Processing*, Laser Tech. J., vol. 7, no. 1, pp. 34–38, 2010.

[203] L. M. Cabalín, A. González, V. Lazic, and J. Laserna. *Deep Ablation and Depth Profiling by Laser-Induced Breakdown Spectroscopy (LIBS) Employing Multi-Pulse Laser Excitation: Application to Galvanized Steel*, Appl. Spectrosc., vol. 65, no. 7, pp. 797–805, Jul. 2011.

[204] J. Lopez, G. Mincuzzi, R. Devillard, Y. Zaouter, C. Hönninger, E. Mottay, and R. Kling. *Ablation efficiency of high average power ultrafast laser*, J. Laser Appl., vol. 27, no. S2, p. S28008, 2015.

[205] J. Thorstensen and S. Erik Foss. *Temperature dependent ablation threshold in silicon using ultrashort laser pulses*, J. Appl. Phys., vol. 112, no. 10, p. 103514, Nov. 2012.

[206] S. Bruening, G. Hennig, S. Eifel, and A. Gillner. *Ultrafast Scan Techniques for 3D-µm Structuring of Metal Surfaces with high repetitive ps-laser pulses*, Phys. Procedia, vol. 12, no. PART 2, pp. 105–115, 2011.

[207] T. Kramer. *Increasing the Specific Removal Rate for Ultra Short Pulsed Laser-Micromachining by Using Pulse Bursts*, J. Laser Micro/Nanoengineering, vol. 12, no. 2, pp. 107–114, Sep. 2017.

[208] J. Schille, L. Schneider, L. Hartwig, U. Loeschner, and L. H. Mittweida. *High-rate laser processing of metals using high-average power ultrashort pulse lasers*, no. November, pp. 88–95, 2015.

[209] B. Jaeggi, S. Remund, R. Streubel, and B. Goekce. *Laser Micromachining of Metals with Ultra-Short Pulses : Factors Limiting the Laser Micromachining of Metals with Ultra-Short Pulses : Factors Limiting the Scale-Up Process*, no. December, 2017.

[210] J. Schille, L. Schneider, A. Streek, S. Kloetzer, and U. Loeschner. *High-throughput machining using high average power ultrashort pulse lasers and ultrafast polygon scanner*, in *Proc. SPIE, 9736*, 2016, p. 97360R.

[211] J. Lopez, K. Mishchik, G. Mincuzzi, E. Audouard, and E. Mottay. *Efficient Metal Processing Using High Average Power Ultrafast Laser*, J. Laser Micro/Nanoengineering,

vol. 12, no. 3, pp. 1–8, Dec. 2017.

[212] J. Schille, L. Schneider, and U. Loeschner. *Process optimization in high-average-power ultrashort pulse laser microfabrication: how laser process parameters influence efficiency, throughput and quality*, Appl. Phys. A Mater. Sci. Process., vol. 120, no. 3, pp. 847–855, Sep. 2015.

[213] N. Rykalin. *Rascety teplovych processov pri svarke*. Moscow: MASGIZ, 1951.

[214] H. S. Carslaw and J. Jaeger. *Conduction of heat in solids*, 2nd ed. Oxford at the Clarendon Press, 1959.

[215] F. Bauer, A. Michalowski, T. Kiedrowski, and S. Nolte. *Heat accumulation in ultra-short pulsed scanning laser ablation of metals*, Opt. Express, vol. 23, no. 2, pp. 1035–1043, 2015.

[216] J. Schille. *Highspeed Laser Micro Processing using Ultrashort Laser Pulses*, J. Laser Micro/Nanoengineering, vol. 9, no. 2, pp. 161–168, Jun. 2014.

[217] E. Mottay, M. Delaigue, B. Schöps, G. Dalla-Barba, E. Audouard, C. Hönninger, O. Bernard, and K. Mishchik. *Efficient micro processing with high power femtosecond lasers by beam engineering and modelling*, Procedia CIRP, vol. 74, pp. 310–314, 2018.

[218] C. He, C. Hartmann, C. Fornaroli, F. Zibner, and A. Gillner. *Temporal evolution of hole geometry and influences of energy deposition in ultra-short pulse helical drilling*, Lasers Manuf. Conf. 2015, pp. 1–8, 2015.

[219] B. Jaeggi, B. Neuenschwander, U. Hunziker, J. Zuercher, T. Meier, M. Zimmermann, K. H. Selbmann, and G. Hennig. *Ultra high precision surface structuring by synchronizing a galvo scanner with an ultra short pulsed laser system in MOPA arrangement*, Proc. SPIE, no. 0, pp. 8243–20, 2012.

[220] B. Jaeggi, B. Neuenschwander, T. Meier, M. Zimmermann, and G. Hennig. *High precision surface structuring with ultra-short laser pulses and synchronized mechanical axes*, Phys. Procedia, vol. 41, pp. 319–326, 2013.

[221] M. Zimmermann, B. Jaeggi, and B. Neuenschwander. *Improvements in ultra-high precision surface structuring using synchronized galvo or polygon scanner with a laser system in MOPA arrangement*, in *Laser Applications in Microelectronic and Optoelectronic Manufacturing (Lamom) XX, San Francisco*, 2015, vol. 9350, p. 935016.

[222] A. Dunn, J. V. Carstensen, K. L. Wlodarczyk, E. B. Hansen, J. Gabzdyl, P. M. Harrison, J. D. Shephard, and D. P. Hand. *Nanosecond laser texturing for high friction applications*, Opt. Lasers Eng., vol. 62, pp. 9–16, 2014.

[223] X. Xu, C. P. Grigoropoulos, and R. E. Russo. *Measurement of solid-liquid interface temperature during pulsed excimer laser melting of polycrystalline silicon films*, Appl. Phys. Lett., vol. 65, no. 14, pp. 1745–1747, 1994.

[224] X. Xu and C. P. Grigoropoulos. *Nanosecond-time-resolution thermal emission measurement during pulsed excimer-laser interaction with materials ~ e KrF excimerJaser Beam meter Oscilloscope*, October, vol. 59, pp. 51–59, 1996.

[225] D. Demange, P. Beauchêne, M. Bejet, and R. Casulleras. *Mesure simultanée de la*

diffusivité thermique selon les deux directions principales d'un matériau, Rev. Générale Therm., vol. 36, no. 10, pp. 755–770, Nov. 1997.

[226] J. Martan, O. Cibulka, and N. Semmar. *Nanosecond pulse laser melting investigation by IR radiometry and reflection-based methods*, Appl. Surf. Sci., vol. 253, no. 3, pp. 1170–1177, 2006.

[227] J. Martan, N. Semmar, and C. Boulmer-Leborgne. *IR radiometry optical system view factor and its application to emissivity investigations of solid and liquid phases*, Int. J. Thermophys., vol. 28, no. 4, pp. 1342–1352, 2007.

[228] M. Kučera, J. Martan, and A. Franc. *Time-resolved temperature measurement during laser marking of stainless steel*, Int. J. Heat Mass Transf., vol. 125, pp. 1061–1068, Oct. 2018.

[229] G. R. B. E. Römer and P. Bechtold. *Electro-optic and Acousto-optic Laser Beam Scanners*, Phys. Procedia, vol. 56, no. C, pp. 29–39, 2014.

[230] L. Li, W. Guo, Z. B. Wang, Z. Liu, D. Whitehead, and B. Luk'yanchuk. *Large-area laser nano-texturing with user-defined patterns*, J. Micromechanics Microengineering, vol. 19, no. 5, p. 054002, May 2009.

[231] R. De Loor, L. Penning, and R. Slagle. *A need for speed in laser processing and micromachining*, Laser Tech. J., vol. 3, pp. 32–34, 2014.

[232] A. Žemaitis, M. Gaidys, P. Gečys, G. Račiukaitis, and M. Gedvilas. *Rapid high-quality 3D micro-machining by optimised efficient ultrashort laser ablation*, Opt. Lasers Eng., vol. 114, no. November 2018, pp. 83–89, 2019.

[233] R. De Loor. *Polygon Scanner System for Ultra Short Pulsed Laser Micro-Machining Applications*, Phys. Procedia, vol. 41, pp. 544–551, 2013.

[234] R. De Loor, L. Penning, and R. Slagle. *A need for speed in laser processing and micromachining*, Laser Tech. J., vol. 3, pp. 32–34, 2014.

[235] A. Streek and M. Lee. *Ultrafast Material Processing with High-Brightness Fiber Lasers*, Laser Tech. J., vol. 14, no. 4, pp. 22–25, Sep. 2017.

[236] A. Lasagni, D. Benke, T. Kunze, M. Bieda, S. Eckhardt, T. Roch, D. Langheinrich, and J. Berger. *Bringing the direct laser interference patterning method to industry: A one tool-complete solution for surface functionalization*, J. Laser Micro Nanoeng., vol. 10, no. 3, pp. 340–344, 2015.

[237] A. I. Aguilar-Morales, S. Alamri, and A. F. Lasagni. *Micro-fabrication of high aspect ratio periodic structures on stainless steel by picosecond direct laser interference patterning*, J. Mater. Process. Technol., vol. 252, no. January 2018, pp. 313–321, Feb. 2018.

[238] V. Lang, T. Roch, and A. F. Lasagni. *High-Speed Surface Structuring of Polycarbonate Using Direct Laser Interference Patterning: Toward 1 m2 min−1 Fabrication Speed Barrier*, Adv. Eng. Mater., vol. 18, no. 8, pp. 1342–1348, 2016.

[239] V. Lang, A. Rank, and A. F. Lasagni. *Large Area One-Step Fabrication of Three-Level Multiple-Scaled Micro and Nanostructured Nickel Sleeves for Roll-to-Roll Hot Embossing*, Adv. Eng. Mater., vol. 19, no. 8, p. 1700126, Aug. 2017.

[240] G. M. Burrowg and T. K. Gaylord. *Multi-beam interference advances and applications: Nano-electronics, photonic crystals, metamaterials, subwavelength structures, optical trapping, and biomedical structures*, Micromachines, vol. 2, no. 2, pp. 221–257, 2011.

[241] V. Furlan, A. G. Demir, G. Pariani, A. Bianco, and B. Previtali. *eu spen ' s 18 th International Conference & A new approach to Direct Laser Interference Patterning with scanner optics for high productivity*, no. June, 2018.

[242] A. I. Aguilar-Morales, S. Alamri, and A. F. Lasagni. *Micro-fabrication of high aspect ratio periodic structures on stainless steel by picosecond direct laser interference patterning*, J. Mater. Process. Technol., vol. 252, no. September 2017, pp. 313–321, Feb. 2018.

[243] H. Sandra, S. V Kirner, and A. Rosenfeld. *Laser-Induced Periodic Surface Structures — A Scientific Evergreen*, IEEE J. Sel. Top. Quantum Electron., vol. 23, no. 3, 2017.

[244] I. Gnilitskyi, T. J. Derrien, Y. Levy, N. M. Bulgakova, and L. Orazi. *High-speed manufacturing of highly regular femtosecond laser- induced periodic surface structures : physical origin of regularity*, no. January, pp. 1–11, 2017.

[245] U. Loeschner, J. Schille, A. Streek, T. Knebel, L. Hartwig, R. Hillmann, and C. Endisch. *High-rate laser microprocessing using a polygon scanner system*, vol. 29303, no. February, 2015.

[246] D. T. E. Myles, M. Ziyenge, J. D. Shephard, and D. C. Milne. *Scanned mask imaging solid state laser tool for cost effective flip chip - chip scale package manufacture*, J. Laser Micro Nanoeng., vol. 10, no. 1, pp. 106–109, 2015.

[247] Y. H. Chang, Y. C. Lin, Y. S. Liu, and C. Y. Liu. *Light-extraction enhancement by cavity array-textured n-polar GaN surfaces ablated using a KrF laser*, IEEE Photonics Technol. Lett., vol. 24, no. 22, pp. 2013–2015, 2012.

[248] A. Horn, C. C. Kalmbach, J. G. Moreno, V. Schütz, U. Stute, and L. Overmeyer. *Laser-Surface-Treatment for Photovoltaic Applications*, Phys. Procedia, vol. 39, pp. 709–716, 2012.

[249] G. Zhu, D. Whitehead, W. Perrie, O. J. Allegre, V. Olle, Q. Li, Y. Tang, K. Dawson, Y. Jin, S. P. Edwardson, L. Li, and G. Dearden. *Thermal and optical performance characteristics of a spatial light modulator with high average power picosecond laser exposure applied to materials processing applications*, Procedia CIRP, vol. 74, pp. 594–597, 2018.

[250] C. Abbott, R. M. Allott, B. Bann, K. L. Boehlen, M. C. Gower, P. T. Rumsby, I. Stassen Boehlen, and N. Sykes. *New techniques for laser micromachining MEMS devices*, 2002, p. 281.

[251] U. Loeschner, J. Schille, A. Streek, T. Knebel, L. Hartwig, R. Hillmann, and C. Endisch. *High-rate laser microprocessing using a polygon scanner system*, J. Laser Appl., vol. 27, no. S2, p. S29303, Feb. 2015.

[252] G. F. Marshall. *Handbook of Optical and Laser Scanning*. CRC Press, 2016.

[253] B. Jaeggi, B. Neuenschwander, M. Zimmermann, R. De Loor, and L. Penning. *High throughput ps-laser micro machining with a synchronized polygon line scanner*, in *8th International Conference on Photonic Technologies LANE 2014*, 2014, pp. 1–8.

[254] A. Dunn, K. L. Wlodarczyk, J. V. Carstensen, E. B. Hansen, J. Gabzdyl, P. M. Harrison, J. D. Shephard, and D. P. Hand. *Laser surface texturing for high friction contacts*, Appl. Surf. Sci., vol. 357, pp. 2313–2319, Dec. 2015.

[255] J. Schille. *Highspeed Laser Micro Processing using Ultrashort Laser Pulses*, J. Laser Micro/Nanoengineering, vol. 9, no. 2, pp. 161–168, Jun. 2014.

[256] M. A. O. Delgado and A. F. Lasagni. *Minimizing stitching errors for large area laser surface processing*, J. Laser Micro Nanoeng., vol. 11, no. 2, pp. 185–191, 2016.

[257] G. Mincuzzi, L. Gemini, M. Faucon, and R. Kling. *Extending ultra-short pulse laser texturing over large area*, Appl. Surf. Sci., vol. 386, pp. 65–71, Nov. 2016.

[258] A. I. Aguilar-Morales, S. Alamri, T. Kunze, and A. F. Lasagni. *Influence of processing parameters on surface texture homogeneity using Direct Laser Interference Patterning*, Opt. Laser Technol., vol. (accepted), pp. 216–227, 2018.

[259] B. Neuenschwander, B. Jaeggi, M. Zimmermann, V. Markovic, B. Resan, K. Weingarten, R. de Loor, and L. Penning. *Laser Surface Structuring with 100W of Average Power and Sub-ps Pulses*, in *International Congress on Applications of Lasers & Electro-Optics (ICALEO), Atlanta*, 2015, no. 1, pp. 14–22.

[260] K. L. Wlodarczyk, A. A. Lopes, P. Blair, M. M. Maroto-Valer, D. P. Hand, K. L. Wlodarczyk, A. A. Lopes, P. Blair, M. M. Maroto-Valer, and D. P. Hand. *Interlaced Laser Beam Scanning: A Method Enabling an Increase in the Throughput of Ultrafast Laser Machining of Borosilicate Glass*, J. Manuf. Mater. Process. 2019, Vol. 3, Page 14, vol. 3, no. 1, p. 14, 2019.

[261] L. A. Dobrzański, A. Drygała, K. Gołombek, P. Panek, E. Bielańska, and P. Zieba. *Laser surface treatment of multicrystalline silicon for enhancing optical properties*, J. Mater. Process. Technol., vol. 201, no. 1–3, pp. 291–296, 2008.

[262] C. E. Christian Daniel, Jannik Manderla, Sina Hallmann. *Influence of an Angular Hatching Exposure Strategy on the Surface Roughness During Picosecond Laser Ablation of Hard Materials*, vol. 83, pp. 135–146, 2016.

[263] C. A. Dold. *Picosecond laser processing of diamond cutting edges*, PhD thesis, no. 21598, p. 144, 2013.

[264] L. Ma and H. Bin. *Temperature and stress analysis and simulation in fractal scanning-based laser sintering*, Int. J. Adv. Manuf. Technol., vol. 34, no. 9–10, pp. 898–903, 2007.

[265] J. Kruth, M. Badrossamay, E. Yasa, J. Deckers, L. Thijs, and J. Van Humbeeck. *Part and material properties in selective laser melting of metals*, 16th Int. Symp. Electromachining, pp. 1–12, 2010.

[266] A. Salama, Y. Yan, L. Li, P. Mativenga, D. Whitehead, and A. Sabli. *Understanding the self-limiting effect in picosecond laser single and multiple parallel pass drilling/machining of CFRP composite and mild steel*, Mater. Des., vol. 107, pp. 461–469, Oct. 2016.

[267] N. Kumar, S. Prakash, and S. Kumar. *Studies of laser textured Ti-6Al-4V wettability for implants*, IOP Conf. Ser. Mater. Sci. Eng., vol. 149, no. 1, 2016.

[268] T. Schonlau, R. Hebel, S. Pause, and G. Mayer. *Machining strategies for versatile ultra-short pulse laser applications*, no. 2013, 2014.

[269] S. Faas, U. Bielke, R. Weber, and T. Graf. *Prediction of the surface structures resulting from heat accumulation during processing with picosecond laser pulses at the average power of 420 W*, Appl. Phys. A Mater. Sci. Process., vol. 124, no. 9, p. 0, 2018.

[270] S. Faas, U. Bielke, R. Weber, and T. Graf. *Scaling the productivity of laser structuring processes using picosecond laser pulses at average powers of up to 420 W to produce superhydrophobic surfaces on stainless steel AISI 316L*, Sci. Rep., vol. 9, no. 1, p. 1933, 2019.

[271] S. Mohanty and J. Hattel. *Cellular scanning strategy for selective laser melting: Capturing thermal trends with a low-fidelity, pseudo-analytical model*, Math. Probl. Eng., vol. 2014, 2014.

[272] EdgeWave GmbH. *PX-seria Datasheet*, *Datasheet*. [Online]. Available: https://www.edge-wave.de/web/wp-content/uploads/2018/03/PXweb2018.pdf. [Accessed: 21-Jun-2018].

[273] SCANLAB. *intelliSCAN III 14*, *Datasheet*. [Online]. Available: http://www.scanlab.de/sites/default/files/PDF-Dateien/Data-Sheets/Scan-Systems/intelliSCAN-EN.pdf. [Accessed: 21-Jun-2018].

[274] D. Moskal, M. Kučera, E. Smazalová, S. Houdková, and R. Kromer. *Application of shifted laser surface texturing*, in *METAL 2015 - 24th International Conference on Metallurgy and Materials, Brno*, 2015, pp. 4103–1–6.

[275] J. Martan, D. Moskal, and M. Kučera. *Laser surface texturing with shifted method—Functional surfaces at high speed*, J. Laser Appl., vol. 31, no. 2, p. 022507, May 2019.

[276] Q. B. Du Keming, Li Daijung. *Master-Oszillator-Leistungsverstärker*, DE Patent 102014017568 B4, 2016.

[277] M. KUČERA, D. MOSKAL, and J. MARTAN. *Method of laser beam writing with shifted laser surface texturing*, US 10,160,229 B2, 2018.

[278] Š. Houdková, P. Šperka, M. Repka, J. Martan, and D. Moskal. *Shifted laser surface texturing for bearings applications*, J. Phys. Conf. Ser., vol. 843, no. 1, p. 012076, May 2017.

[279] R. Kromer, S. Costil, J. Cormier, D. Courapied, L. Berthe, P. Peyre, and M. Boustie. *Laser surface patterning to enhance adhesion of plasma sprayed coatings*, Surf. Coatings Technol., vol. 278, no. 2015, pp. 171–182, Sep. 2015.

[280] I. M. Kučera. *ZNAČENÍ A VLIV NA KOROZNÍ ODOLNOST KOROZIVZDORNÝCH OCELÍ MARKING AND THE EFFECT ON THE CORROSION RESISTANCE OF THE STAINLESS*, 2016.

[281] D. Bergström, J. Powell, and A. F. H. Kaplan. *The absorptance of steels to Nd:YLF and Nd:YAG laser light at room temperature*, Appl. Surf. Sci., vol. 253, no. 11, pp. 5017–5028, 2007.

[282] R. S. Graves, T. G. Kollie, D. L. McElroy, and K. E. Gilchrist. *The thermal conductivity of AISI 304L stainless steel*, Int. J. Thermophys., vol. 12, no. 2, pp. 409–415, Mar. 1991.

[283] Deutsche Edelstahlwerke GmbH. *Data sheet X5CrNi18-10*, 2015. [Online]. Available: https://www.dew-stahl.com/fileadmin/files/dew-stahl.com/documents/Publikationen/Werkstoffdatenblaetter/RSH/1.4301_de.pdf. [Accessed: 30-May-2019].

[284] ATI. *304™ Austenitic Stainless Steel*, *Datasheet*, 2018. [Online]. Available: https://www.atimetals.com/Products/ati-304.

[285] I. JAHM Software. *MPDB Software*. [Online]. Available: https://www.jahm.com. [Accessed: 22-Oct-2018].

[286] W. M. Steen and J. Mazumder. *Laser Material Processing*. London: Springer London, 2010.

[287] West Bohemia University in Plzen. *LabIR*, *Thermographic paint for standard applications*, 2018. [Online]. Available: http://paints.labir.eu/documents/LabIR Paint HERP-LT-en-product leafleft-web.pdf. [Accessed: 21-Jun-2018].

[288] P. Soille. *Morphological Image Analysis*, Second Edi. Berlin, Heidelberg: Springer Berlin Heidelberg, 2004.

[289] M. Ghoreishi, D. K. . Low, and L. Li. *Comparative statistical analysis of hole taper and circularity in laser percussion drilling*, Int. J. Mach. Tools Manuf., vol. 42, no. 9, pp. 985–995, Jul. 2002.

[290] Matlab. *bwconncomp*, *Documentation*. [Online]. Available: https://www.mathworks.com/help/images/ref/bwconncomp.html#bu2xdbl-6. [Accessed: 22-Mar-2019].

[291] A. SEMEROK, B. SALLÉ, J.-F. WAGNER, and G. PETITE. *Femtosecond, picosecond, and nanosecond laser microablation: Laser plasma and crater investigation*, Laser Part. Beams, vol. 20, no. 1, pp. 67–72, Jan. 2002.

[292] Houdková, P. Šperka, M. Repka, J. Martan, D. Moskal, Š. Houdková, P. Šperka, M. Repka, J. Martan, and D. Moskal. *Shifted laser surface texturing for bearings applications*, J. Phys. Conf. Ser., vol. 843, no. 1, 2017.

[293] A. Kovalchenko, O. Ajayi, A. Erdemir, G. Fenske, and I. Etsion. *The effect of laser surface texturing on transitions in lubrication regimes during unidirectional sliding contact*, Tribol. Int., vol. 38, no. 3, pp. 219–225, Mar. 2005.

[294] N. G. Semaltianos, W. Perrie, P. French, M. Sharp, G. Dearden, and K. G. Watkins. *Femtosecond laser surface texturing of a nickel-based superalloy*, Appl. Surf. Sci., vol. 255, no. 5, pp. 2796–2802, Dec. 2008.

[295] J. Martan, D. Moskal, L. Prokešová, and M. Honner. *Detection of heat accumulation in laser surface texturing by fast infrared detectors*, in *The Laser in Manufacturing (LiM2019)*, 2019, pp. 1–7.

[296] I. M. Kučera. *PHYSICAL PROCESSES DURING THE LASER MARKING AND THE EFFECT ON THE CORROSION RESISTANCE OF THE STAINLESS STEEL*, 2016.

[297] D. Moskal, J. Martan, V. Lang, and M. Švantner. *The Stamp method for processing of high noise data from infrared sensor in harsh environment*, Sensors Actuators A Phys.,

vol. 263, pp. 480–487, Aug. 2017.

[298] D. Moskal, J. Martan, and M. Kučera. *Shifted Laser Surface Texturing (sLST) in Burst Regime*, J. Laser Micro/Nanoengineering, vol. 14, no. 2, pp. 1–6, Sep. 2019.

[299] T. Kramer, S. Remund, M. Gafner, D. Zwygart, B. Neuenschwander, R. Holtz, R. Witte, and N. Dury. *Novel strategy for ultrafast pulsed laser micromachining of rotational symmetric metallic parts*, Procedia CIRP, vol. 74, pp. 611–617, 2018.

[300] Z. M. Schlüter H., Jaeggi B., Neuenschwander B. *Applications : Galvo scanners reach megahertz- scale range repetition rates for laser micromachining Maximizing ablation*, Laser Focus World, vol. 12, no. 16, pp. 1–9, 2016.

[301] E. Hecht and M. Griot. *Optics*, 4th ed., no. 1. San Francisco: Addison-Wesley, 2002.

[302] D. Moskal, J. Martan, M. Kučera, Š. Houdková, and R. Kromer. *Picosecond Laser Surface Cleaning of AM1 Superalloy*, Phys. Procedia, vol. 83, pp. 249–257, 2016.

[303] D. Moskal, J. Martan, V. Lang, M. Švantner, J. Skála, and J. Tesař. *Theory and verification of a method for parameter-free laser-flash diffusivity measurement of a single-side object*, Int. J. Heat Mass Transf., vol. 102, pp. 574–584, 2016.

[304] D. Moskal, J. Martan, V. Lang, M. Švantner, J. Skála, and J. Tesař. *Theory and verification of a method for parameter-free laser-flash diffusivity measurement of a single-side object*, Int. J. Heat Mass Transf., vol. 102, 2016.

[305] R. Weber, T. Graf, P. Berger, V. Onuseit, M. Wiedenmann, C. Freitag, and A. Feuer. *Heat accumulation during pulsed laser materials processing*, Opt. Express, vol. 22, no. 9, p. 11312, 2014.

[306] M. Planck, M., Masius. *The Theory of Heat Radiation*. Philadelphia: The Maple Press – York PA (P. Blakiston's Son & Co.), 1914.

[307] Q. Wang, L. Jiang, J. Sun, C. Pan, W. Han, G. Wang, H. Zhang, C. P. Grigoropoulos, and Y. Lu. *Enhancing the expansion of a plasma shockwave by crater-induced laser refocusing in femtosecond laser ablation of fused silica*, Photonics Res., vol. 5, no. 5, p. 488, Oct. 2017.

[308] B. Luther-Davies. *Picosecond high-repetition-rate pulsed laser ablation of dielectrics: the effect of energy accumulation between pulses*, Opt. Eng., vol. 44, no. 5, p. 051102, 2005.

[309] D. M. Goebel and I. Katz. *Fundamentals of Electric Propulsion: Ion and Hall Thrusters*, Fundam. Electr. Propuls. Ion Hall Thrusters, pp. 1–507, 2008.

[310] L. Nagli, M. Gaft, I. Gornushkin, and R. Glaus. *Stimulated emission and lasing in laser-induced plasma plume Stimulated emission and lasing in laser-induced plasma plume*, Opt. Commun., vol. 378, no. November, pp. 41–48, 2016.

[311] C. Gaudiuso, G. Giannuzzi, A. Volpe, P. M. Lugarà, I. Choquet, and A. Ancona. *Incubation during laser ablation with bursts of femtosecond pulses with picosecond delays*, Opt. Express, vol. 26, no. 4, pp. 8958–8968, 2018.

[312] *Polygon Scanner Systems*, *Datasheet*. [Online]. Available:

https://nextscantechnology.com/wp-content/uploads/2018/12/NST_PolygonScannerSystems_2018.pdf. [Accessed: 03-Sep-2019].

[313] A. Letan, E. Audouard, K. Mishchik, C. Hönninger, and E. Mottay. *Use of bursts for femtosecond ablation efficiency increase*, pp. 1–6, 2019.

[314] M. K. Denys Moskal, Jiri Martan. *Shifted laser surface texturing (sLST) in burst regime*, J. Laser Micro/Nanoengineering, Jan. 2019.

[315] J. Matějíček, M. Vilémová, D. Moskal, R. Mušálek, J. Krofta, M. Janata, Z. Kutílek, J. Klečka, S. Heuer, J. Martan, E. Nardozza, Š. Houdková, and D. Dorow-Gerspach. *The Role of Laser Texturing in Improving the Adhesion of Plasma Sprayed Tungsten Coatings*, J. Therm. Spray Technol., vol. 28, Oct. 2019.

[316] D. Dufft, A. Rosenfeld, S. K. Das, R. Grunwald, and J. Bonse. *Femtosecond laser-induced periodic surface structures revisited: A comparative study on ZnO*, J. Appl. Phys., vol. 105, no. 3, 2009.

[317] Q.-Z. Zhao, S. Malzer, and L.-J. Wang. *Self-organized tungsten nanospikes grown on subwavelength ripples induced by femtosecond laser pulses.*, Opt. Express, vol. 15, no. 24, pp. 15741–6, 2007.

[318] J. Romano, A. Garcia-giron, P. Penchev, and S. Dimov. *Applied Surface Science Triangular laser-induced submicron textures for functionalising stainless steel surfaces Ultra short pulsed ShuΣer laser source Quarter Waveplate 100mm F-ϑ lens Scanning Δz*, Appl. Surf. Sci., vol. 440, pp. 162–169, 2018.

[319] P. A. Dmitriev, S. V. Makarov, V. A. Milichko, I. S. Mukhin, A. K. Samusev, A. E. Krasnok, and P. A. Belov. *Direct Femtosecond Laser Writing of Optical Nanoresonators*, J. Phys. Conf. Ser., vol. 690, no. 1, p. 012021, Feb. 2016.

[320] J. Sampedro, R. Ferre, E. Fernández, I. Pérez, B. Cárcel, T. Molina, and J. A. Ramos. *Surface Functionalization of AISI 316 Steel by Laser Texturing of Shaped Microcavities with Picosecond Pulses*, Phys. Procedia, vol. 39, pp. 636–641, 2012.

[321] Z. Liu, W. Xu, Z. Hou, and Z. Wu. *A Rapid Prototyping Technique for Microfluidics with High Robustness and Flexibility*, Micromachines, vol. 7, no. 11, p. 201, Nov. 2016.

[322] J. Schille, L. Schneider, F. Ullmann, S. Mauersberger, and U. Löschner. *Bio-inspirierte Funktionalisierung von technischen Oberflächen durch Hochrate-Lasermikrostrukturierung*, in *ThGOT Thementage Grenz- und Oberflächentechnik und 5. Kolloquium Dünne Schichten in der Optik*, 2017, no. 12.

8. List of publications

Articles in impact journals

I. J. Matějíček, M. Vilémová, D. Moskal, R. Mušálek, J. Krofta, M. Janata, Z. Kutílek, J. Klečka, S. Heuer, J. Martan, E. Nardozza, Š. Houdková, and D. Dorow-Gerspach. *The Role of Laser Texturing in Improving the Adhesion of Plasma Sprayed Tungsten Coatings*, J. Therm. Spray Technol., vol. 28, Oct. 2019.

II. D. Moskal, J. Martan, M. Kučera. *Shifted laser surface texturing (sLST) in burst regime.* J. Laser Micro/Nanoengineering, vol. 14, no. 2, pp. 1–6, Sep. 2019.

III. D. Moskal, J. Martan, M. Kučera. *Laser surface texturing with shifted method—Functional surfaces at high speed.* Journal of Laser Applications 31(2):022507-1. doi: 10.2351/1.5096082, 2019

IV. D. Moskal, J. Martan, V. Lang, M. Švantner. *The Stamp method for processing of high noise data from infrared sensor in harsh environment*. Sensors and Actuators A: Physical, Volume 263, 2017, Pages 480-487, ISSN 0924-4247

V. D. Moskal, Jiří Martan, Vladislav Lang, Michal Švantner, Jiří Skála, Jiří Tesař. *Theory and verification of a method for parameter-free laser-flash diffusivity measurement of a single-side object*. In International Journal of Heat and Mass Transfer, Volume 102, 2016, Pages 574-584, ISSN 0017-9310

Conference papers

VI. J. Martan, D. Moskal, L. Prokešová, and M. Honner. *Detection of heat accumulation in laser surface texturing by fast infrared detectors*, in The Laser in Manufacturing (LiM2019), 2019, pp. 1–7.

VII. D. Moskal, J. Martan, M. Kučera. *Scanning strategy of high speed shifted laser surface texturing*. The Laser in Manufacturing (LiM), Munich, Germany from June 26 to June 29 2017.

VIII. D. Moskal, J. Martan, M. Kučera, Š. Houdková, R. Kromer. *Picosecond Laser Surface Cleaning of AM1 Superalloy*, In Physics Procedia, Volume 83, 2016, Pages 249-257, ISSN 1875-3892

IX. D. Moskal, J Martan, E. Smazlova, Š. Houdkova. *Influence of initial surface state on laser surface texturing result.* Conference: METAL 2016, BRNO

X. D. Moskal, M. Kucera, E. Smazlova, Š. Houdkova, R. Kromer. *APPLICATION OF SHIFTED LASER SURFACE TEXTURING*. Conference: METAL 2015, Brno

XI. Š Houdková, P Šperka, M Repka, J Martan and D Moskal. *Shifted laser surface texturing for bearings applications*. IOP Conf. Series: Journal of Physics: Conf. Series 843 (2017) 012076 doi :10.1088/1742-6596/843/1/012076.

Patents

XII. M. Kučera, D. Moskal, J. Martan. *Method of laser beam writing with shifted laser surface texturing*. International Application No.: CT/IB2015/000807. International Filing Date: 28.05.2015

XIII. M. Kučera, D. Moskal, J. Martan. *Method of laser beam writing with shifted laser surface texturing*. United States Patent and Trademark Office. US 10,160,229 B2. 2018.

9. Appendices

9.1. APPENDIX A. Surface processing rate of different scanning strategies

	Scanning strategy	Scanning technique	Interval	Processing rate (cm^2/min)	Scanning speed	Reference
1	DLIP-head, interference pattering	Sample movement	$\sim \lambda/2$ (343÷1064 nm)	100 ÷ 9000	1 m/s	[236]–[239]
2	DLIP-head, dynamic interference pattering	Galvanometer scanner	$\sim \lambda/2$ (532÷1064 nm)	0.7 ÷ 10	0.16÷6.8 cm/s	[241], [242]
3	LIPSS	Galvanometer scanner	0.9 µm	6.3	3 m/s	[244]
4	Array of square microobjects with inner nano-structure (200 nm) – multishot per object	Sample movement	0.8 µm	0.01	300 mm/s	[319]
5	Array of complex microobjects on cylinder – multishot per object	Sample rotation and acousto-optic beam deflection	250 um	~ 46.8	1.5 m/s (rotation) 40 m/s (AOD scanning)	[206]
6	Array of circle microobjects – one shot per object	Galvanometer scanner	12.5÷200 µm	1.8 ÷ 428	25÷400 cm/s	[254]
7	Array of circle microobjects with inner micro/nano-structure – multishot per object	Galvanometer scanner	30 ÷40 µm	0.4 ÷ 0.75	~ 5÷20 cm/s	[43], [87]
8	Array of square microobjects with inner micro-structure – multishot per object	Galvanometer scanner	2 mm	0.15 ÷ 0.20	0.5 m/s	[320]

9	Complex irregular microstructure	Galvanometer scanner	50 µm	1.2	400÷2000 mm/s	[321]
10	Straight hatch lines	Galvanometer scanner	4 µm	8 ÷ 25	4.5÷17.1 m/s	[216]
11	Straight interlaced lines	Galvanometer scanner	1.2÷6 µm	0.017 ÷ 2	24÷600 mm/s	[260]
12	Straight hatch lines	Multibeam galvanometer scanner	0.5 mm	5400	20 m/s	[249]
13	Straight hatch lines	Polygonscanner	14.5÷40 µm	148 ÷ 7680	60÷800 m/s	[233], [234], [251]
14	Complex regular structure	Polygonscanner	10 µm	840	10÷200 m/s	[210]
15	Spike formation	Polygonscanner	1÷12 µm	0.03, approx. 60	25 m/s	[257]
16	Ripple structures	Polygonscanner	40 µm	43	15 m/s	[322]
17	One pulse per array of microobjects	Sample movement with mask	20 µm	1800	–	[110], [250]

9.2. APPENDIX B. Thermo-physical properties AISI 304

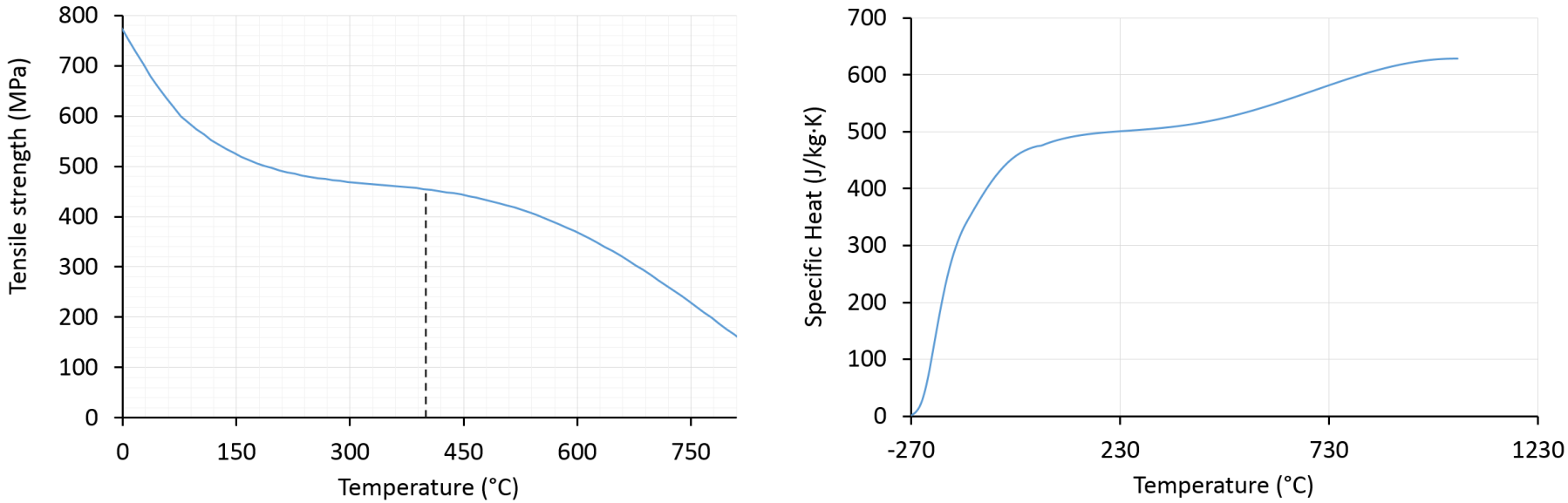

Fig. B1. Temperature dependency of physical properties AISI 304: *a*) tensile strength [284]; *b*) specific heat [285].

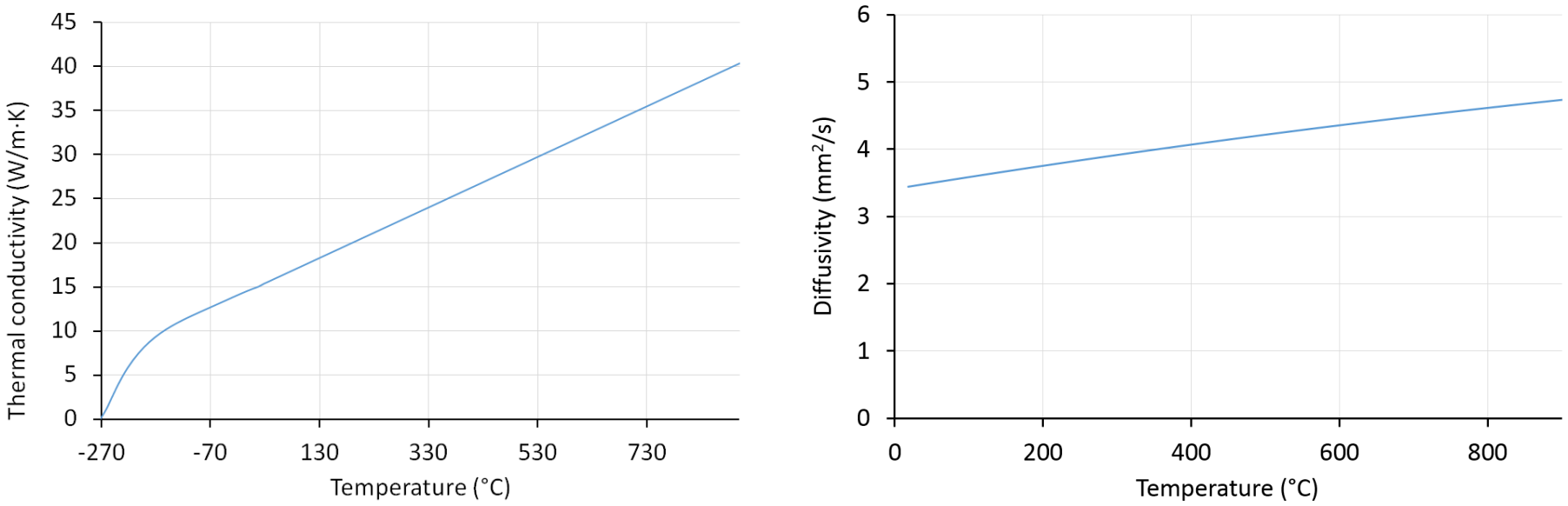

Fig. B2. Temperature dependency of physical properties AISI 304: a) heat capacity [285]; b) heat diffusivity [285]

Errata for Ph.D. Dissertation

Denys Moskal

This document lists errors found in the printed version of Ph.D. dissertation "Thermo-physical processes and ultrashort pulse laser scanning methods in surface texturing", together with corrections where applicable. Only errors that matter from a mathematical view point are listed.

Location	Original text	Correction
Page 63, eq. (4.16)	$F = F_0 \cdot e^{-2r/w_0}$	$F = F_0 \cdot e^{-2r^2/w_0^2}$
Page 64, eq. (4.18)	$\Delta T(t,z) = \dfrac{\eta \cdot F \cdot e^{-\frac{2r}{w_0}-\frac{z^2}{4\cdot\alpha\cdot t}}}{\rho \cdot c \cdot \sqrt{\pi \cdot \alpha \cdot t}}$	$\Delta T(t,z) = \dfrac{\eta \cdot F_0 \cdot e^{-\frac{2r^2}{w_0^2}-\frac{z^2}{4\cdot\alpha_{th}\cdot t}}}{\rho \cdot c \cdot \sqrt{4 \cdot \pi \cdot \alpha_{th} \cdot t}}$
Page 64, eq. (4.19)	$\Delta T_{Sum}(t,z) = \left(\eta \cdot F/\rho \cdot c \cdot \sqrt{\pi \cdot \alpha}\right) \cdot \sum_{n=1}^{N} e^{-\frac{2r_n}{w_0}-\frac{z^2}{4\cdot\alpha\cdot t}} \Big/ \sqrt{t-t_n}$	$\Delta T_{Sum}(t,z) = = \left(\eta \cdot F_0/\left(\rho \cdot c \cdot \sqrt{4 \cdot \pi \cdot \alpha_{th}}\right)\right) \cdot \sum_{n=1}^{N} e^{-\frac{2r_n^2}{w_0^2}-\frac{z^2}{4\cdot\alpha_{th}\cdot(t-t_n)}} \Big/ \sqrt{t-t_n}$